UNIVERSITAT POLITÈCNICA DE VALÈNCIA

Instituto de Tecnología Química

Metal Nanoparticles Wrapped on Defective Nitrogen-Doped Graphitic Carbons as Highly Selective Catalysts for CO_2 Hydrogenation

Doctoral Thesis

Presented by:

Lu Peng

Supervised by:

Prof. Hermenegildo García Gómez

S.T. & Dr. Ana Primo Arnau

Valencia, July, 2021

Table of Contents

List of abbreviations in the present PhD thesis

Fischer-Tropsch synthesis (FTS)

Reverse water-gas shift (RWGS)

Clusters (CLs)

Nanoparticles (NPs)

N-doped graphene [(N) G]

Metal nanoparticles (MNPs)

N-doped graphitic carbon [(N)C]

Co-Fe alloy NPs wrapped on N-doped graphitic carbons [Co-Fe@(N)C]

X-ray diffraction (XRD)

Inductively coupled plasma-optical emission spectrometry (ICP-OES)

Field emission scanning electron microscopy (FESEM)

Transmission electron microscopy (TEM)

High-resolution transmission electron microscopy (HRTEM)

Dark-field (DF)

Energy dispersive spectrometry (EDS)

Gas chromatography (GC)

Turnover frequency (TOF)

Acknowledgments

Time is fleeting. At this moment, as the PhD thesis is about to be completed, I would like to express my sincere gratitude to my supervisors, Prof. Hermenegildo Garcia, S.T. Ana Primo, and my colleagues in ITQ. Without their kind help, I would not be able to complete the works presented in this thesis.

Set the time back to three and half years ago, when I knew that my PhD application failed. Everything was so bad and desperate. However, there is an old saying in China that to bottom out, which means that when everything can't get worse, a turning point is coming. What a coincidence. After heard that there are available global-oriented positions in the group of Prof. Hermenegildo, I sent an e-mail including my resume and transcripts with nervousness and expectation. It turned out I was so lucky. With tremendous support from Herme and Ana, my application for the doctoral candidate got approved. Even if the time has passed for so long, I can clearly remember that when I received Herme's mail, congratulations, Lu. In the next three months, I passed the IELTS and completed the application for the visa with help from Inma and Ana. Finally, at the end of November, I came to Spain and started my PhD career. The day of November 27, 2017, is a memorable day in my life. On this day, I left my motherland to pursue my ideals with great expectations for the future.

When I first arrived at ITQ, Herme gave me several projects mainly about the preparation of three-dimensional graphene based on the use of polysaccharides as the precursor *via* a soft-template method, of which my research work for PhD was carried out. With the exhaustive guidance and extended help of Herme and Ana, everything went well. During the constant PhD study with Herme, his enthusiasm for scientific research and dedication has always encouraged me to explore and move forward. On the road of scientific research, there would always be bumps. Whenever it happens, Herme and Ana have always patiently guided me to overcome difficulties. In my impression, Herme is erudite, knowledgeable, and hard-working. His rigorous inspiration for scientific research has always motivated me to make progress. Not only that, his positive attitude towards everything also deeply inspired me that work and life should be kept in a good balance, which will continue to influence me in the future. Compared to the supervisor, S.T. Ana is more like my friend. Whenever I encounter troubles no matter in work or life, she has always helped me to exclude the difficulty and anxiety. We could share scientific achievements and unforgettable experiences but also complain about occasional dissatisfaction and misfortune in life. Being a member of Herme's group is a great fortune for me and knowing Herme and Ana is the precious treasure in my life.

In ITQ, everyone has their own work but within a framework of collaboration. We are like a big family. Thanks to the excellent researchers and technicians around me. Without their endless help, I would not complete my work. The technician team in ITQ (Estefania, Mª Isabel, Maria Adelina, Rosa, Miguel, Mariam, Javie...) and the microscope service of UPV (Manuel, Alicia, Mercha, Ximo, Jose Luis) have always given me the firmest support which helps me focus on scientific research without worrying about the characterization issue. Thanks for the tremendous support from my colleagues in ITQ (Abde, Josep, Amparo, Yong, Pedro, Ester, Maria, Alberto, Ruben, Jiajun, Xiangze, Andres, Horatiu, Ana, Rocio, Alejandra, Manolo, Tugca, Aicha, Nisrine, Yue, Paula...) and in chemistry department (Mercedes, Sergio, Belen, Herme J, Murthy, Cristina, Arianna, Juan, Eva...). Their humor and dedication make our group full of joy and love. In addition, I felt I was so lucky to make friends in ITQ (Anna, Rosella, Jose, Alice, Bea, Judit, Jenny, Eva, Zaher, Jodi, Camilo, Hans, Marcos, Maria, Fernando, Elena...). They made my daily life colorful and full of joy. Thanks for my dearest friends, Anna and Rosella, without their endless love and company, I could not survive on the way to being a PhD. Their warm encouragement always keeps me moving forward. Because of them, I could know what means, regret we didn't meet each other sooner. I will never forget the time that we were together and the wonderful memories they brought. Thought that we would be separated for a very long time in the future, I couldn't help crying. (T-T) They may be afar, but we will never be apart. Besides, I would also feel gratitude to my friends in Valencia (Lichen, Jinling, Chuanzhi, Qintong, Yimeng, Chengeng, Zhuohua, Lixin, Jinan, Xuehua, Zi, Tiemin...). They helped me to adapt to life abroad quickly and brought me a lot of joy. Due to their company and support, I could feel the warmth of family even abroad. I really appropriate the endless support from Lichen and Jinling who have set excellent examples to me on both working on science and living a balanced life. Thanks for enlightening and encouraging me when I am lost and down. Thanks for being my friends and being around. Wish we all a bright future, in various ways.

Besides, I would also show my sincerest appreciation to BASF SE for financial support as well as the supervision and guidance of Prof. Vasile I. Parvulescu at the University of Bucharest and Dr. Alvaro Gordillo of BASF during the last two years.

Almost all chapters in the PhD thesis are based on the research project of BASF. Thanks BASF and Prof. Herme for giving me such a rare opportunity to participate in this project. Meanwhile, thanks Prof. Vasile and Prof. Bogdan Jurca for all their contributions in this cooperation. In the past one and a half years, the progress check meetings have been held every two weeks to discuss experimental results, solutions to problems, and next work arrangements, showing me amazing state-of-art technologies to study nanomaterials and catalysis on the nanometer regime. Their awesome execution and professionalism made me admire and the valuable experience of working with them has greatly broadened my horizon and prompted me a lot.

In addition, I would like to say thank you to my family. Thanks for their education and cultivation, meticulous care and patience, endless tolerance and support for every decision I have made, and always being my solid backup and haven. Thanks my love, Junda. Thanks for your endless love and being with me. I will love you forever and ever. I love sea, love flowers, love sunrise and sunset, no more than I love you. Hope we will never be absent in the years to come.

In the end, thanks for the world, time, the people I have met, all the happy and sad, lucky and unfortunate, lighthearted and tough experiences, all these shaped together who I am today. Thanks myself for being exploring forward at a loss, and persisting till the end. Thanks healthcare workers and scientists worldwide for all their great efforts to overcome the covid-19 and save Earth.

CHAPTER 1

Introduction

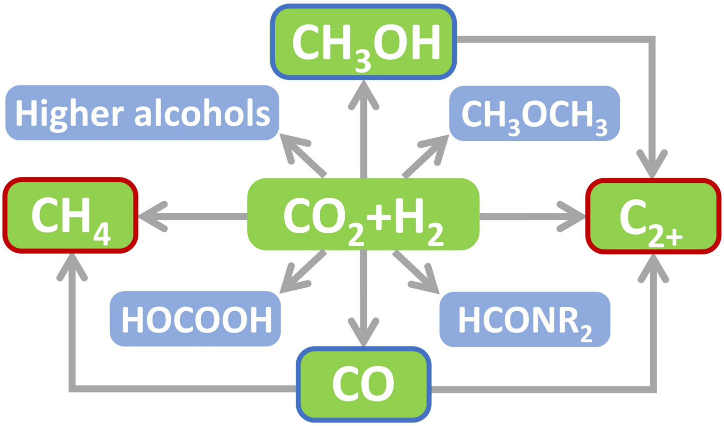

CHAPTER 1

CHAPTER 1

1.1 Climate Change and Global Warming

1.1.1 Climate change

On multi million-year time scales, Earth's climate has alternated between cold ice ages and ice-free greenhouse periods.[1] Currently, Earth is in the Quaternary glaciation, known as the Ice Age.[2] An interval of time under cold climate within an ice age is termed as glaciation, alternatively glacial. On the other hand, interglacials are periods of warmer climate between glacials, referring relatively higher global temperature.[3] These climate changes had natural origins related to variations in solar output, changes in Earth's orbit around the sun and the atmospheric composition, such as the concentrations of carbon dioxide and methane , as shown in **Figure 1.1**.[4] It is noted that these natural climate changes have significantly influenced on the life on the planet, favoring the growth of large vegetation, while causing the extinction of reptiles such as dinosaurs and even mammal animals like mammoths, saber-toothed tigers and others.

With the emergence of the Industrial Revolution and for the purpose of good manufacturing, humankind has made increasing use of energy initially based on the coal and wood until the First World War. In this period, between the First and Second World War, there was a huge shift from coal to liquid gasoline and fossil fuels. The fossil resources have become the primary energy resource for development of society and the consumption of fossil resources has steadily grown over the years and reached some peaks related to the economic periods of expansion or recession. The use of fossil fuels is mainly based on the thermal energy released during the combustion of hydrocarbons with the formation of carbon dioxide and water.

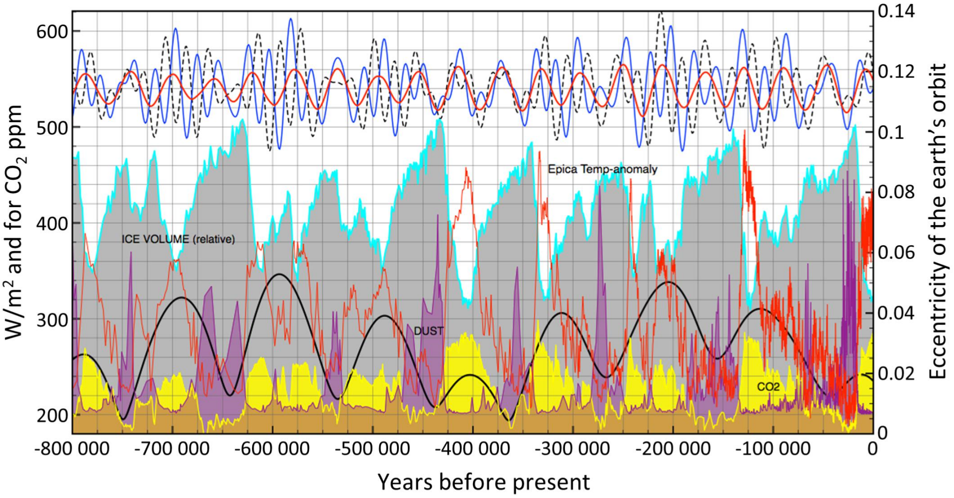

Figure 1.1. Comparison of the relationship between the ice volume, CO_2 concentration and Earth's orbit during the last 800,000 years. Ice volume (grey); epica T-anom (red); CO_2 levels (yellow); epica dust (purple); eccentricity (black); total insolation at either pole (red); maximum summer insolation at north pole (blue) and south pole (dashed).[5]

Current data from the U.S. Department of Energy indicate that the daily global demand for fuel is over sixty million barrels crude oil and similar vast scale of natural gas. One crude oil barrel is 42 gallons and about 160 liters which can generate 660 m^3 CO_2. Therefore, numerous amount of CO_2 are released to the atmosphere every day. The CO_2 concentration in the atmosphere is not toxic, however, the massive burning of fossil fuels has steadily increased atmospheric CO_2 concentration from the value about 150 ppm in the early 20th Century to the current 420 ppm that has been measured recently by the National Oceanic and Atmospheric Administration Earth System Research Laboratory.[6] The recent change is amazing and unprecedented. The increase in CO_2 has never exceeded 30 ppm in last one thousand years, however, CO_2 concentration has increased by 30 ppm in the past 17 years. **Figure 1.2** shows the data from the national atmosphere of ocean laboratory, exhibiting the continuing increase in CO_2 concentration in the atmosphere.[7] Worth noting in **Figure 1.2** are the seasonal changes of CO_2 concentration between summer and winter that are due to the photosynthesis activity in the North Hemisphere and reveals the small influence of natural photosynthesis to control the CO_2 concentration at the levels currently produced.

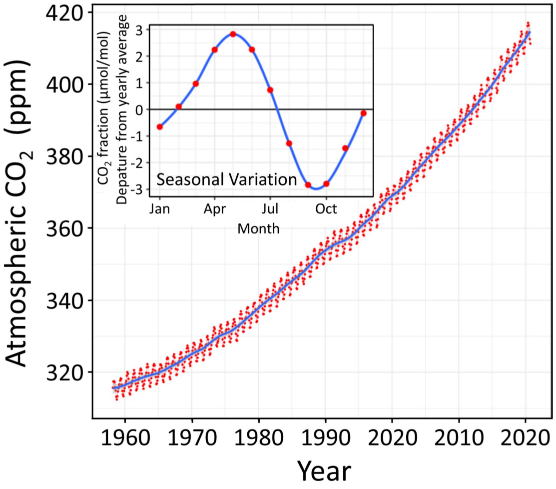

Figure 1.2. The Keeling Curve of monthly atmospheric CO_2 concentrations measured from 1958 to 2020 at Mauna Loa Observatory, Hawaii.[7]

1.1.2 Evidence of greenhouse effect

Evidence of greenhouse effect can be obtained from the permanent ice exploration in the Antarctica. The permanent ice containing the data of the atmosphere over millions of years has correlated CO_2 concentration and Earth's climate by drilling and analyzing hundreds of meters depth of the ice core. Interglacial periods are related with thin layers of ice, while glacial periods corresponding to much thicker ice. And each ice contains entrapped bubbles of air in which the concentration of CO_2 can be analyzed and determined. The CO_2 concentration correlates strongly with the temperature of the glacial and interglacial periods. The ice core record indicates CO_2 mole fractions stayed within a range of 180 ppm to 270 ppm throughout the last 800,000 years until Industrial Revolution.[8] Measurements from Antarctic ice cores also show that before industrial emissions started, atmospheric CO_2 mole fractions were about 280 ppm,[9] and stayed between 260 and 280 ppm during the preceding ten thousand years.[10] However, since the beginning of the Industrial Revolution, the atmospheric concentration of carbon dioxide have gone up by approximately 45 %, rising from 280 ppm in 1750 to 418 ppm in 2021.[7]

In addition, studies on Earth's climate have also shown that there are certain molecules in Earth's atmosphere that can absorb and emit radiation in the infrared wavelength range, causing an effect that has been denoted as greenhouse effect, shown in **Scheme 1.1**.[11] As a consequence, the radiatively active gases, also known as greenhouse gases, radiate energy in all directions in Earth's atmosphere and part of this radiation can be redirected towards Earth's surface, thus increasing the temperature of the biosphere. The primary atmospheric greenhouse gases are water vapor , carbon dioxide, methane, nitrogen oxides (NO_x), and ozone (O_3).[12] The most abundant greenhouse gas, accounting for about two-thirds of greenhouse gases, carbon dioxide, is largely the product of burning fossil fuels.[10] In addition, the direct radiative effect of a mass of methane is about 84 times stronger than that of carbon dioxide itself over a 20-year time frame[13] and the presence of methane in the atmosphere also related to the massive use of fossil fuels as the primary energy source.

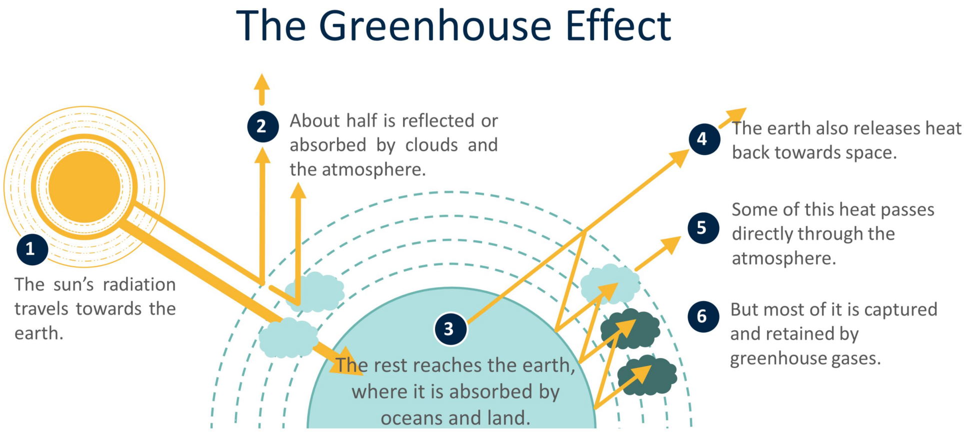

Scheme 1.1. Illustration of the greenhouse effect.

1.1.3 International agreements

Starting from the Sustainable Development Goals (SDGs) in 2015 designed to be a "*blueprint to achieve a better and more sustainable future for all*", United Nations (UN) has always been concerning about the sustainability and preservation of eco-systems and natural forests of the planet.[14] The Intergovernmental Panel on Climate Change (IPCC) was set up by the UN Environment Commission to provide objective and scientific evidences on climate changes. In 2013, the IPCC presented its conclusions on the role of human activities in climate change and concluded categorically that climate change is real and human activities are the main cause. The predicted consequence of this change on humankind and life on the planet are dramatic, recommending actions to mitigate this change. Subsequently, in 2015, a landmark agreement was reached to mitigate climate change and to accelerate and intensify the actions and investments needed for a sustainable low carbon future.[15] The Paris Agreement, after Kyoto Protocol, for the first time, brought all nations into a common cause to undertake ambitious efforts against climate change and adapt to its effects. The central aim of Paris Agreement is to strengthen the global response of all nations to the threat of climate change by keeping the global temperature increase in this century, well below 2 °C above the pre-industrial level and to pursue efforts to limit global warming to 1.5 °C by the end of the century.[16] There are now about 200 countries corresponding to 90% human population that have ratified the Paris Agreement. With global emissions reaching record levels and showing no sign of peaking, in September 2019, UN called on to a reduction of greenhouse gas emissions by 45 % over the next decade by 2020, and to net zero emissions by 2050.[17]

The European Union (EU) was the key in favor of the change in the energy sector and to abandon fossil fuels as the main energy source. EU has considered the change as an opportunity and over 1.5 billion Euros of public funding was used to promote this low-carbon transition with clear milestones to raise the 2030 greenhouse gas emission reduction target, including less emissions and source removals, to at least 55% compared to 1990.[18] In addition, EU aims to be climate-neutral by 2050, an economy with net-zero greenhouse gas emissions.[17] This objective is at the heart of the European Green Deal and in line with the EU's commitment to global climate action under the Paris Agreement.[16] In this transitional period until the lined objective is reached, while controlling carbon dioxide emissions, the capture and utilization of carbon dioxide are also important for coping with global warming. For this reason, an active scientific research fields has focused on different ways to capture CO_2 as well as the chemical use of CO_2 as feedstock to produce fuels and offer value-added carbon-containing chemicals.

1.2 CO_2 as the Inert Molecule

As a nontoxic, abundant and renewable carbon source, the chemical utilization of CO_2 into value-added products is very attractive since it will contribute to diminish atmospheric CO_2 emissions and the replacement of dwindling fossil fuels.[19] However, carbon dioxide is a well-known highly stable molecule ($\Delta_f G_{298K}$ = -396 kJ·mol^{-1}) and most of the reactions involving CO_2 are thermodynamically uphill, meaning that these reactions require entropy to occur.[20] In other words, the activation and subsequent conversion of carbon dioxide are energy-demanding processes. Therefore, in the context of CO_2 capture and utilization, the number of spontaneous reactions that can be performed by using CO_2 as starting material is very few. **Scheme 1.2** illustrates some of the reactions that have been considered for CO_2 utilization, including urea formation,[21] diethyl carbonate production[21] and ethanol from CO_2.[22] Other reactions, such as the formation of methanol[23] and other higher alcohols,[24] are reversible and the equilibrium are largely shifted towards CO_2 into organic compounds. A large energy input is required to transform CO_2. Thus, the addition of another substance with relatively higher Gibbs energy will make the CO_2 conversion more favorable thermodynamically. As an easily available and high-energy material, hydrogen can be used as the reagent for CO_2 transformation. Therefore, CO_2 hydrogenation, using H_2 obtained from renewable energy,[25] could be a promising research direction. Electrochemical H_2 production can serve to deal with the intermittence of renewable electricity and produce chemicals and fuels. In this way, not only CO_2 emissions will be diminished but also the whole strategy will cover the shortage of fossil fuels.

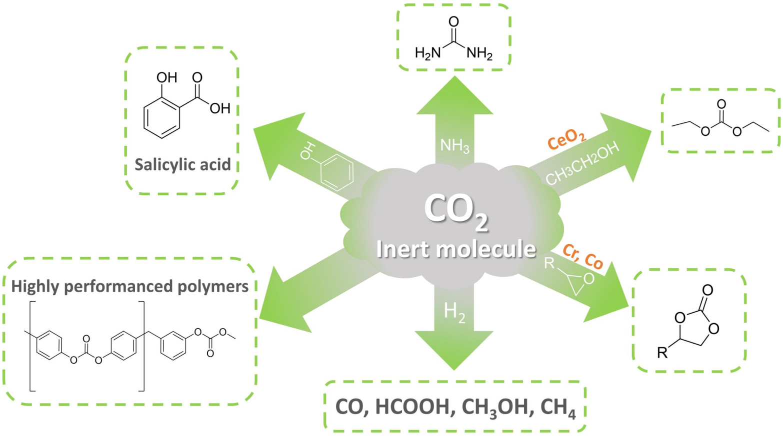

Scheme 1.2. Illustration of different reactions that can be used for CO_2 utilization.

1.3 CO_2 Hydrogenation

Catalytic CO_2 hydrogenation is considered as a potential path forward sustainable production in a large variety of compounds, such as methane, higher hydrocarbons, formic acid, methanol and higher alcohols.[26] As it can be seen in **Scheme 1.3**, products of CO_2 hydrogenation can be liquid, but most frequently they are gases. Considering the depletion of fossil fuels, CO_2 hydrogenation to hydrocarbons is a promising way to covert CO_2 into fuels, among other CO_2 hydrogenation products.

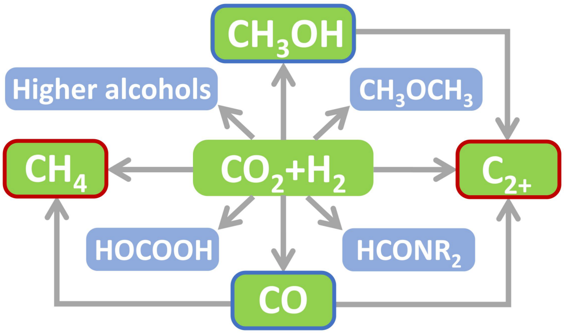

Scheme 1.3. Catalytic CO_2 hydrogenation to chemicals and fuels.

There are different possible pathways to produce C_{2+} hydrocarbons from CO_2 hydrogenation (**Scheme 1.4**). Two typical parallel reactions to obtain from CO_2 hydrogenations are reverse water-gas shift (**Eq. 1.1**, RWGS)[27, 28] and methanol formation (**Eq. 1.2**).[29, 30] The value-added C_{2+} products could be directly obtained through Fischer-Tropsch synthesis[31] from syngas (a mixture of carbon monoxide and hydrogen) or the methanol-to-hydrocarbon (MTH) process.[32] MTH was first discovered in 1976 and can transfer methanol into a series of compounds, including methanol-to-olefin (MTO)[33] and methanol-to-gasoline (MTG)[34] and methanol-to-aromatics (MTA) reactions.[35] In addition, the indirect methanol-mediated route can also be used to obtain carbon-containing chemicals and fuels, in which methanol is produced by CO_2 hydrogenation and then the obtained methanol is dehydrated or coupled over zeolites or alumina.[36] Evidently, it is possible to develop bifunctional or hybrid catalysts used for both methanol synthesis and dehydration/coupling,[37] in a way that CO_2 can be directly converted into high-value C_{2+} products. Recently, the direct pathway of CO_2 modified Fischer-Tropsch synthesis (CO_2-FTS) has been developed. In this process, CO_2 is converted to CO *via* the RWGS reaction that is coupled with CO conversion to hydrocarbons *via* FTS.[38]

$$CO_2 + H_2 \rightleftharpoons CO + H_2O \quad \Delta_rH_{298K} = 41.2\ \text{kJ·mol}^{-1} \qquad \textbf{(Eq. 1.1)}$$

$$CO_2 + 3H_2 \rightleftharpoons CH_3OH + H_2O \quad \Delta_rH_{298K} = -49.5\ \text{kJ· mol}^{-1} \qquad \textbf{(Eq. 1.2)}$$

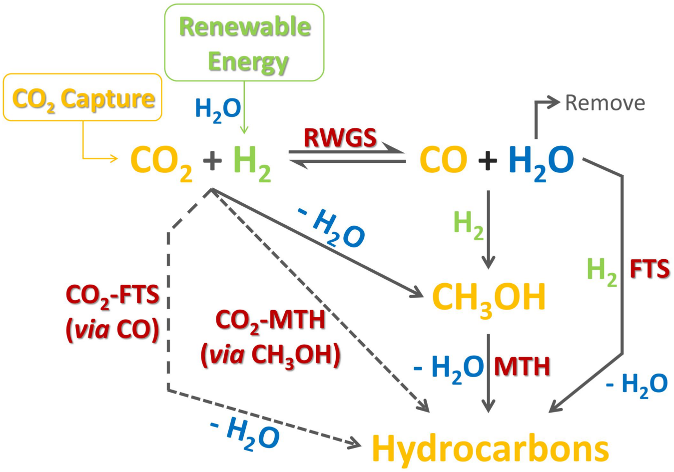

Scheme 1.4. Different pathways to produce long-chain hydrocarbons from CO_2 hydrogenation.

1.3.1 CO_2 hydrogenation to methane

In contract to typical reactions for CO_2 utilization, CO_2 hydrogenation to methane can be performed easily at atmospheric pressure and high gas hourly space velocity (GHSV) at the CO_2 conversion and selectivity values close to theoretical equilibrium values.[39] The process of converting CO_2 into CH_4 is named as the Sabatier reaction, because it was first reported by French chemists Paul Sabatier and Jean-Baptiste Senderens in 1897.[40] One of the main important feature of the methanation is that the reaction is highly exothermic and accompanied by a decrease in volume. Thus, the high pressure and the low temperature are favorable conditions. Typically, methanation can be carried out at a temperature range of 250 to 350 °C and under 25 bar pressure *via* Sabatier reaction (**Eq. 1.3**)[41] or Fischer-Tropsch process (**Eq. 1.4**). In terms of industrial production, the infrastructure for the synthesis, storage, transport, and utilization of methane is fairly well-established.

$$CO_2 + 4H_2 \rightleftharpoons CH_4 + 2H_2O \quad \Delta_r H_{298K} = -165.0\ kJ\cdot mol^{-1} \qquad (\textbf{Eq. 1.3})$$

$$CO + 3H_2 \rightleftharpoons CH_4 + H_2O \quad \Delta_r H_{298K} = -206.1\ kJ\cdot mol^{-1} \qquad (\textbf{Eq. 1.4})$$

1.3.2 CO_2 hydrogenation to methanol

Other typical C_1 products obtained through CO_2 hydrogenation are methanol and formic acid. Although the consumption of CH_4 as a primary constituent of natural gas has increased greatly, the price of methane is quite low compared with the price of methanol about 340 euros per ton.[42] Despite the fact that methanol is currently produced in a large multi-ton scale, about 148 million metric tons in 2019, there is still possible to increase considerably methanol consumption, particularly if the application of methanol as a fuel is implemented. In any case, forecasts of the market indicate that methanol production will at least double by 2030 due to new processes driving from methanol, particularly its use as direct-methanol fuel cells (DMFC).[43, 44] Formic acid has been considered for chemical storage of H_2,[45] although it has low hydrogen storage capacity, only 4.4 wt.% gravimetrically and 53 $kg \cdot m^{-3}$ volumetrically, compared to other alternative among the chemicals However, the significant benefit of formic acid over methanol or ammonia is that the dehydrogenation of formic acid can be realized at very mild conditions, in some cases even at room temperature.[46]

Methanol has a considerable advantage over other possible liquid C_1 products derived from CO_2 at mild temperatures. Compared with formic acid, methanol has the advantage of having a much higher energy density, according to its combustion enthalpy of 22 700 $kJ \cdot kg^{-1}$ about three times higher than that of formic acid.[47] Not only that, as a transportation fuel, methanol could be used in combustion engines reaching high engine power with minor modifications, compared with the current gasoline motors.[48] Methanol can even be used as a liquid fuel to generate electricity in proton exchange membrane fuel cells (PEMFC) having a similar configuration as those powered with hydrogen.[49] In addition, the DMFC make it possible to generate electricity directly from methanol which could be applied in the field of transportation and distributed energy generation.[44] Thus, the use of methanol as fuel could become a smooth transition between the current massive use of fossil fuels to the future hydrogen technology. In fact, methanol is considered as a liquid organic hydrogen carrier (LOHC), since methanol reforming can deliver up to three hydrogen molecules per methanol molecule.[44, 50] Then, the H_2 storage capacity of methanol is about 19 % that is among the highest percentage for LOHCs. Although the process will emit unwanted CO_2, the cycle could have a zero-CO_2 footprint if methanol is formed in turn from CO_2.[50] Therefore, regarding CO_2 utilization, the consumption of methanol has a considerable potential to grow and therefore can contribute to achieving a massive decrease in atmospheric CO_2 emissions. **Scheme 1.5** illustrates some possible uses of methanol as an alternative fuel to natural gas and crude oil.

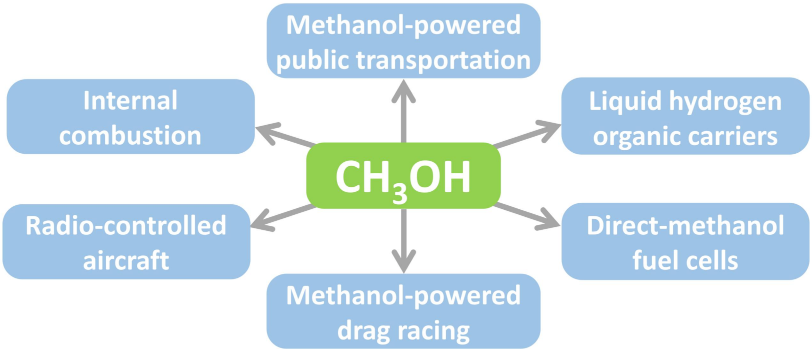

Scheme 1.5. Different uses of methanol as an alternative fuel.

Earlier research, especially from Klier,[51] suggests that carbon monoxide is the major feedstock for methanol synthesis. Currently, CO_2 hydrogenation to methanol is a well-established process (**Eq. 1.2**) While it incorporates the generation of water, CO could be obtained from CO_2 *via* RWGS by consumption of water. (**Eq. 1.1**) Thus, the CO conversion to methanol can be expressed as **Eq. 1.5**.

$$CO + 2H_2 \rightleftharpoons CH_3OH \quad \Delta_rH_{298K} = -\,90.7\ kJ\ mol^{-1} \qquad (\textbf{Eq. 1.5})$$

Both methanol formation reactions (**Eq.s 1.2** and **1.5**) are exothermal and involve a decrease of volume. Therefore, from the thermodynamic point of view, the equilibrium of methanol formation is more favorable at low temperatures and high pressures. However, due to the stability of CO_2, the slow kinetics determines that measurable reaction rates require high temperatures and the use of suitable catalysts to form methanol. Under these conditions, CO_2 conversion can be limited by the equilibrium composition. Generally, under the conditions of methanol formation, CO formation (**Eq. 1.1**)[27] is the only competing reaction and, therefore, typical reaction mixtures are composed by methanol and CO in various proportions. **Figure 1.3** shows the equilibrium composition for CO_2 hydrogenation to methanol and CO as a function of the temperature.[52]

The above consideration explains why CO_2 hydrogenation to methanol is carried out at temperatures below 300 °C, typically in the range from 250 to 300 °C, and high pressures, generally above 30 bar, being common pressures close to 100 bar. Under these conditions, every path of CO_2 is expected a few conversion percent and methanol selectivity is the key parameter. In this context, shown in **Figure 1.3**, a target in the area would be to diminish the reaction temperature to near 200 °C that at the stoichiometric H_2/CO_2 of 3 would allow CO_2 conversions close to 20 % without compromising methanol selectivity. Accordingly, in the reported formation of methanol from CO_2 hydrogenation at temperature between 200 to 300 °C, CO is frequently the main by-product. Thus, the introduction of transition metal oxides in catalysts used for CO_2 hydrogenation to methanol can promote more efficiently the activation of H_2 and decrease the reaction temperature.

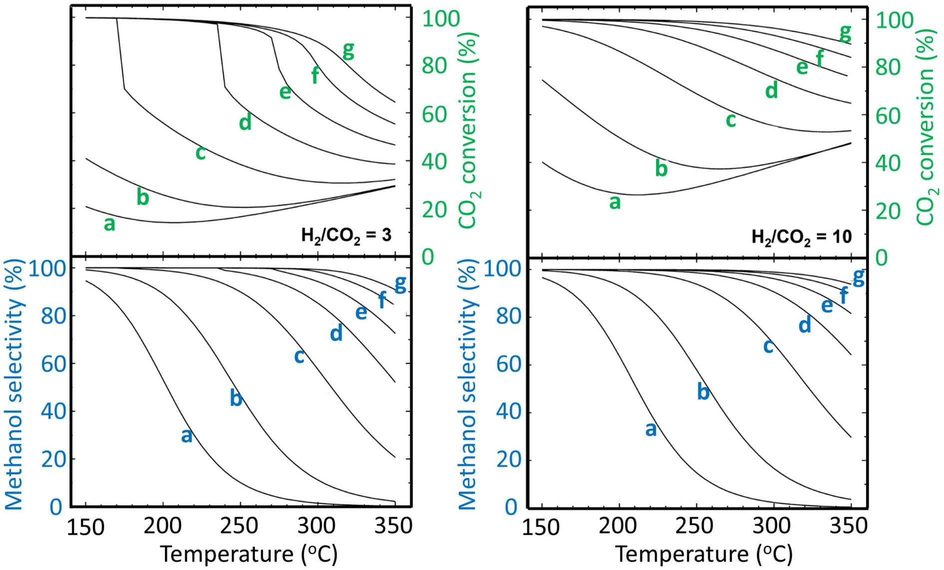

Figure 1.3. Equilibrium of CO_2 conversion and methanol selectivity as a function of temperatures and H_2/CO_2 stoichiometric ratio at pressures of **a**: 10 bar; **b**: 30 bar; **c**: 100 bar; **d**: 200 bar; **e**: 300 bar; **f**: 400 bar and **g**: 500 bar.[52]

1.3.3 CO_2 hydrogenation to C_{2+} hydrocarbons

Compared with the generation of C_1 products, the conversion of CO_2 to C_{2+} product is more challenging due to the high C-C coupling barrier and the competition with CO_2 methanation.[53] However, considering the relative price in the market and the energy density of C_{2+} hydrocarbons respect to methane, it is clear that a selective CO_2 conversion into C_{2+} hydrocarbons would be extremely more attractive. Recently, considerable progress has been made in the catalytic hydrogenation of CO_2 to various value-added C_{2+} products, including olefins, liquid fuels, and higher alcohols.[54]

As previously mentioned, C_{2+} hydrocarbons could be obtained through FTS from syngas and the CO_2 modified FTS. A typical FTS process is the catalytic syngas conversion to generate a mixture of linear alkanes and alkenes, whose distribution as a function of the number of carbons can be predicted by the Anderson-Schulz-Flory (ASF) model (**Figure 1.4**).[19] A predicted maximum fraction of C_2-C_4 hydrocarbons is about 56.7 %, but with an undesired methane percentage of 29.2 %.[55] Therefore, the catalysts required for the FTS should increase the selectivity to C_2-C_4 hydrocarbons while reduce the formation of methane.

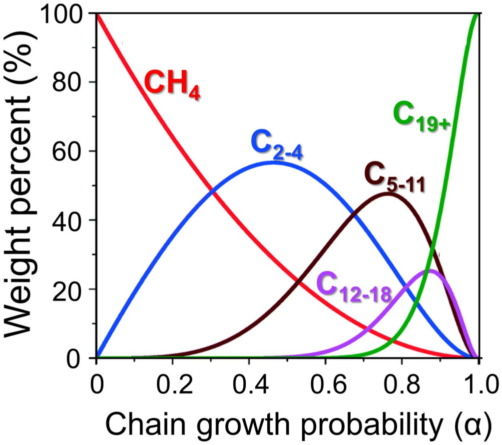

Figure 1.4. Products distribution according to the Anderson-Schulz-Flory model.[19]

Compared with the FTS, the CO_2 modified FTS integrates the CO_2 conversion to CO *via* the RWGS reaction and subsequent CO hydrogenation to hydrocarbons *via* FTS. Combination of the RWGS and the FTS in a single process is more favored because this transformation can be realized in one reactor, thus reducing manufacturing cost. The bifunctional catalysts used for the CO_2 modified FTS should be active in both endothermic RWGS and exothermic FTS under same operation conditions, namely, *CO generation and subsequent *CO hydrogenation, as shown in **Scheme 1.6**.[56]

The product distribution could be wide based on the structure and composition of the catalysts used in CO_2 hydrogenation. Thus, the development of appropriate catalysts that can drive the product selectivity towards C_{2+} hydrocarbons is significant in the area.

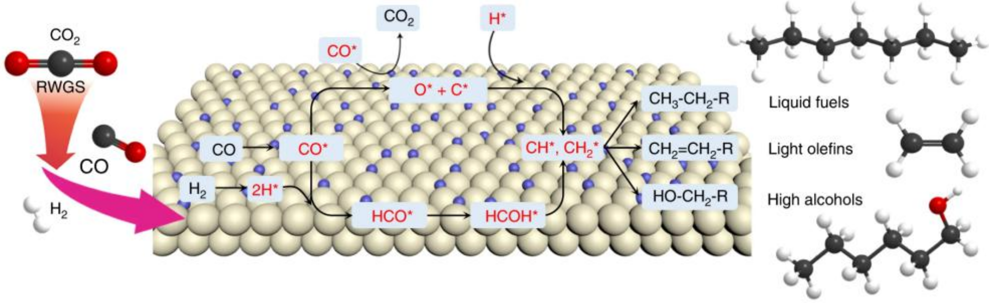

Scheme 1.6. Illustration of the CO_2 modified FTS-based catalytic mechanism.[56]

1.4 Catalysts for CO_2 Hydrogenation

The previous paragraphs have paid attention to the thermodynamics of CO_2 hydrogenation and the variety of products that could be obtained depending on the available reaction paths. However, due to its extreme inertness, all the reactions involving CO_2 are remarkably slow and do not exhibit significant reaction rates even at temperatures as high as 350 ^{o}C or above. One general way to increase the reaction rate is the use of catalysts with active sites, opening new reaction pathways by the interaction between catalysts and substrates.[57] Through the interaction between active sites and reactants, it is possible to achieve product selectivity towards target molecules.

Chemical industry prefers the use of solid catalysts that are in a different phase to that of reactants and products. The advantage of solid catalysts is that they are easy to separate from the reaction mixture through immobilization of the solid catalyst in a reactor while performing in a continuous flow process at an appropriate reaction temperature. **Figure 1.5** shows an overview of four currently used converter designs to illustrate the use of solid catalysts in large scale industrial processes.[58]

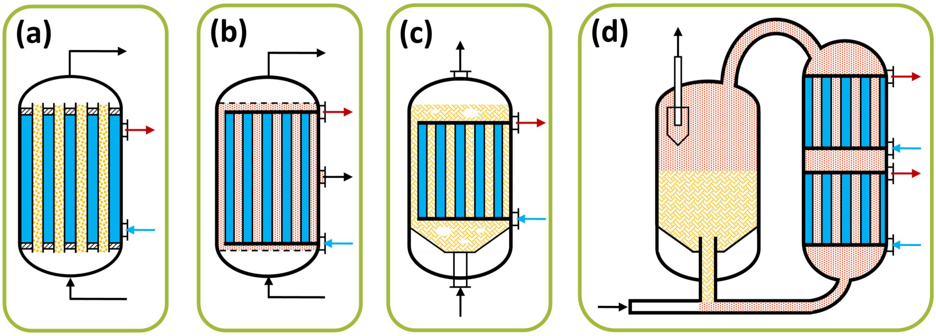

Figure 1.5. An overview of four currently used converter designs. (**a**: fixed bed; **b**: slurry phase; **c**: fluidized bed; **d**: circulating fluidized bed.)

1.4.1 Catalysts for CO_2 hydrogenation to methane

CO_2 methanation can be catalyzed by transition metals such as cobalt,[59] nickel,[60] ruthenium,[61] rhodium,[62] and palladium,[63] in which Ni-based catalysts are the most widely used in industry to obtain CH_4 due to the high CO_2 conversion, remarkable CH_4 selectivity and convenient availability. A typical highly-efficient catalyst for Sabatier reaction is Ni/SiO_2 with a high specific surface area.[64]

1.4.2 Catalysts for CO_2 hydrogenation to methanol

Early industrial-scale production of methanol was performed at high temperatures (320-450 ^{o}C) and pressures by using a sulfur-resistant ZnO/Cr_2O_3 catalyst at the facilities of BASF in 1923.[65] Then, the high-pressure process was gradually replaced by the current exclusively used low-pressure processes (50-100 bar). After the discovery by BASF of copper chromite ($CuCrO_3$) as a catalyst for CO_2 hydrogenation to methanol, the most widely used catalyst is copper and zinc oxide supported on alumina (Cu-ZnO/Al_2O_3) that is the current benchmark catalyst for the process.[66] The typical atomic proportion of Cu/Zn is 3:1 and loading on Al_2O_3 can be around 20 % in weight. Although the catalyst is generally denoted as Cu-ZnO, *in situ* studies suggest that under the reaction conditions, ZnO undergoes a chemical reduction to metallic Zn that forms a bronze alloy with Cu.[67] In another way, even though under ambient conditions, Zn is oxidized by atmospheric oxygen, and Cu and Zn become separate in different phases, the Cu-ZnO/Al_2O_3 should be considered a precursor of the active sites, rather than the real catalyst.[67]

In spite that Cu-ZnO/Al_2O_3 was reported many years ago and the intense research on catalytic CO_2 hydrogenation to methanol, the progress in the development of other more efficient catalysts that could promote the CO_2 conversion to methanol at lower temperatures has been limited. Besides alumina, zirconia in different crystallographic phases is also considered a suitable support.[68, 69] In this regard, one of the best catalysts so far reported in the literature is the one in which copper nanoparticles are incorporated inside the cavities of UiO-66(Zr) as described by Yaghi and coworkers.[70] **Scheme 1.7** shows a model and TEM image of this Cu NC-UiO-66 catalyst in which the $Zr_6O_4(OH)_4$ nodes of UiO-66 play a similar role as ZrO_2 support and the Cu particle size is limited by the dimensions of the UiO-66 cages to a few nanometers.

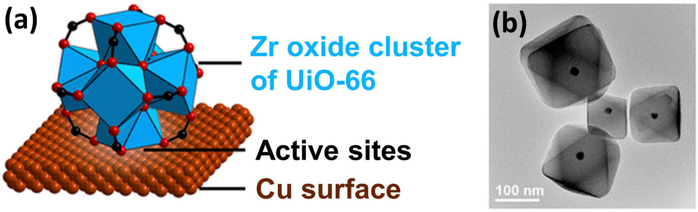

Scheme 1.7. Illustration of active site (**a**) and TEM image (**b**) of Cu NC-UiO-66 catalyst.[70]

In a totally different system, a series of noble metal based catalysts, such as Ga-Pd,[71] Pt-MoO_X/Co-TiO_2[72] and Au-CeOX/TiO_2[73] have been reported for CO_2 hydrogenation to methanol at low temperatures and pressures. Pure indium oxide can convert

7.1 % of CO_2 with a CH_3OH selectivity of 39.7% at 330 ^oC and 5 MPa.[74] However, copper and zinc are generally preferred compared with indium or gallium-based catalysts due to their larger abundance in Nature.[75] Although the introduction of transition metal oxides contributes to the catalytic CO_2 conversion to methanol, it also leads to excessive hydrogenation of CO_2 to CH_4, thereby reducing the selectivity of methanol.

In this context, Cu and ZnO supported on defective graphene could be considered as a potential catalyst for CO_2 hydrogenation to methanol in order to realize the low-temperature and high-efficiency CO_2 hydrogenation methanol. The target of this reaction would be to operate at a temperature around 200 ^oC, reaching the thermodynamic equilibrium of methanol.

1.4.3 Catalysts for CO_2 hydrogenation to C_{2+} hydrocarbons

Iron and cobalt-based supported catalysts with appropriate promoters are predominantly used in the field of CO_2 hydrogenation to obtain value-added C_{2+} hydrocarbons.[76] Currently, it has been found that certain Co catalysts, especially those exposed on the surface patches of cobalt oxide and metallic Co, can give certain selectivity to C_{2+} products under a specific operation condition. In the current of art, the selectivity to C_{2+} products can be achieved as high as 30 % but with low CO_2 conversions, typically below 25 %. Thus, it would be significant to develop highly selective Co or Co-Fe catalysts towards C_{2+} hydrocarbons at higher CO_2 conversions.

In the present Doctoral Thesis, the particle size of a series of Co-Fe alloy nanoparticles have been supported on nitrogen-doped graphene with the attempt to drive C_{2+} hydrocarbons formation with high selectivity at a higher conversion. Evidently, the RWGS reaction converting CO_2 into CO is a process closely related to the steam reforming that will be the main process producing CO. During the process of the water-gas shift reactions, the excess of CO with steam giving rise to CO_2 and H_2. The water-gas shift is industrially employed to balance the proportion between CO and H_2 formed in the steam reforming process having the correct CO/H_2 proportion for the FTS of hydrocarbons and alcohols. It appears as logical to also perform these Co-based catalysts for the reverse water-gas shift reaction. Therefore, in addition to develop the size window of the Co-Fe-based catalyst as it is required for FTS, it is also reasonable to employ these Co and Co-Fe-based catalysts to promote the RWGS reaction.

1.4.4 Influence of supports

The present PhD Thesis deals with the utilization of CO_2 as feedstock for the production of high-value fuels and chemicals and it is focused on the development of catalysts that could drive CO_2 hydrogenation selectively with high conversions towards a wide range of products directly from CO_2. There are vast numbers of studies that report different kinds of catalysts for CO_2 hydrogenation exhibiting selectivity towards specific hydrocarbons. These catalysts have in common that transition metals are supported on solid materials with large specific surface areas.

Among them, the use of noble metals such as Pd, Ru and Pt have received considerable attention.[77] However, due to the high price of those precious metals and for the sake of sustainability, current research is paying more attention to the first-row of transition metal that are considerably more abundant and affordable.

It is remarkable that the nature of the transition metal in the catalysts determine the final product in a large extent. Catalysts such as Fe, Co, Ni and Cu supported on silica and carbon materials have been comprehensively investigated in CO_2 hydrogenation.[78] Among them, Fe and Co-based catalysts are widely used in the CO_2 modified FTS, due to the significant selectivity to C_{2+} hydrocarbons.[79] These active transition metal in the form of small nanoparticles or even clusters and single atom supported on metal oxides with large surface areas, such as γ-Al_2O_3,[80] ZrO_2,[81] TiO_2[82] and CeO_2[83] have been frequently reported as solid catalysts for CO_2 hydrogenation. In addition to inorganic materials, organic-inorganic solid, such metal organic frameworks (MOFs),[84] organic polymer,[85] carbon nanotubes (CNTs),[86] graphene[87] and mesoporous carbons have also been used as supports.

The primary role of the support in CO_2 hydrogenation is to maintain the size of small metal NPs under reaction conditions. Typically, metal NPs tend to grow and agglomerate when activated under operation conditions. Therefore, the support plays an important role in maintaining a high metal dispersion by means of the interactions between catalytic active sites and supports, which could influence the activity of catalysts as well as the selectivity of products.

In addition, the supports can also cooperate with the reaction mechanism by absorbing CO_2 from the gas phase and putting it in contact with the metal or by the favorable sorption of oxygen and water from the surface of metal active sites.[88] In the case of Fe-based catalysts employed in CO_2 hydrogenation, it is considered that γ-Al_2O_3 performs best than other supports such as SiO_2 and TiO_2 due to the strong metal-support interaction established with the active sites,[89] and it could also avoid sintering during reaction. CNTs and graphenes catalysts with superior thermal and chemical stability are also good carbon supports for CO_2 hydrogenation. Nitrogen-doped CNTs have been used as supports to prepare Fe-based catalysts and the catalytic results show that the incorporation of N-doped CNTs greatly improved Fe dispersion and its reducibility because of the enhanced hydrophilicity and appropriate metal-support interaction. In comparison, oxygen-rich supports such as SiO_2 show an stronger interaction with the iron oxides species, which exhibits a negative influence on the reducibility of Fe, resulting in a worse CO_2 conversion and selectivity.[90]

In the present PhD Thesis, the only used support will be graphitic carbon, whose structure is constituted by the stacking of defective graphene layers and the active metal phases established by strong interactions with these graphene sheets. The electronic charge transfers between the graphene layers and the supported metal NPs can increase the catalytic activity compared with those NPs on other supports, particularly, those in VIII group on the surface. In addition, a common feature of the graphitic carbon employed in the PhD Thesis is that they are obtained by the pyrolysis of natural polysaccharides such as alginate and chitosan following procedures developed by our group.

1.4.4.1 Graphitic carbons as support

The earliest research on graphene could be traced back to 1895, when the highly lamellar structure of thermally reduced graphite oxide was noticed.[91] In the following decades, the structure of graphite was determined by powder X-ray diffraction and single-crystal diffraction.[92, 93] The term "*graphene*" was first proposed by German chemist Hanns-Peter Boehm in 1961[94] and then used to describe the single sheet of graphite when the property of graphite to form intercalation compounds was first observed.[95] It was noted that it was not until nearly half century later that independent graphene sheets were not properly isolated from graphite by a low-cost method and its electronic properties were studied.[96] Then, studies deserved the Nobel Prize in Physics in 2010 for the groundbreaking research on the two-dimensional (2D) material graphene and the discovery of the universe of 2D nanomaterials. The highly-crystallized graphite consists of the stacked graphene layers with an interplanar distance of 3.41 Å.[97] The van der Waals π-π attraction between the graphene layers is strong enough to result in the difficulty and low efficiency of complete exfoliation of graphite into individual graphene layers. For instance, the exfoliation of graphite by ultrasonication in a liquid medium requires the use of highly-viscous and low-volatility liquids, which does not produce exfoliation in a significant extent and later they are difficult to remove from the graphene. Evidently, graphene obtained from the sonication of graphite in organic solvents taken place typically with a yield of less than 1 wt.%.

Due to all the above problems, as shown in **Scheme 1.8**, the most widely used procedure to obtain graphene from graphite in large quantities involves three intermediate steps, consisting of the deep chemical oxidation of graphite to form graphite oxide, the subsequent exfoliation of graphite oxide and a final reduction of graphite oxide sheets. The key feature of the process is that during the oxidation process of graphite, functional groups such as hydroxyl and epoxide groups are inserted or bonded to the graphene layers, leading to an increased d-spacing from 3.4 Å to around 7.1 Å,[97] which makes the exfoliation process easier. In addition, the absence of π–π conjugated regions in graphite oxide also facilitates the exfoliation of graphite oxide compared to graphene sheets.

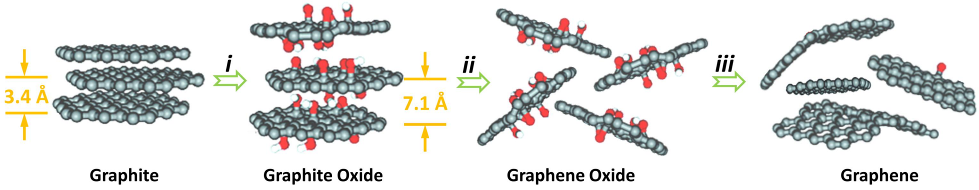

Scheme 1.8. Procedure used to obtain graphene from graphite, *i*: the oxidation of graphite to form graphite oxide, *ii*: the exfoliation of graphite oxide to form graphene oxide, *iii*: the reduction of graphene oxide to form graphene.

The main problem of graphite regarding its exfoliation is its high crystallinity. In this context, our group has shown that graphitic carbons lacking crystallization can be obtained from carbohydrates such as polysaccharides.[98] The conversion of polysaccharides to graphitic carbons can be easily performed by a thermal treatment at temperatures above 850 °C under inert atmosphere. The process is generally denoted as pyrolysis and can be adequately performed in a tubular electric oven, in which an inert gas flows or high vacuum ensure the absence of oxygen. During pyrolysis, the high initial oxygen content of carbohydrates that is generally over 50 wt.% decreases by the evolution of H_2O, CO_2, CO and other gases, remaining a residual oxygen content, typically about 10 wt.% or below depending on the pyrolysis conditions[99] Besides carbon and oxygen, other elements such as nitrogen, sulfur, phosphorous can also be present in the composition of polysaccharides and which can remain attached to the resulting graphitic carbon as dopant elements[100] The innovation of the preparation procedure developed by our group is that these graphitic carbons can be easily exfoliated into single or few layers defective graphene in a very high yield over 70 % upon sonication.

A typical case of a natural polysaccharide that can be converted into N-doped graphene is chitosan, a linear polysaccharide composed of glucosamine (deacetylated unit) and N-acetylglucosamine (acetylated unit) randomly distributed and bonded through β-(1-4) glycosidic bonds.[99] Chitosan can be obtained from the shells of shrimps and other crustaceans under alkaline hydrolysis conditions. During pyrolysis, the nitrogen atoms of chitosan, about 7 wt.% in weight, become grafted on the graphene layers. In this regard, doping of nitrogen can be considered as a type of defect. The term "*defective*" indicates the existence of differences respect to ideal graphene. These difference can be pentagons or heptagons carbocycle and carbon vacancies present on the graphene layers, while the ideal graphene is constituted exclusively by carbon atoms in hexagonal geometry. The presence of doping elements, such as N, O, S and P, on the carbon lattice can take place with different coordinations. The content of the doping elements on graphene can be decreased by increasing the temperature of the thermal treatment.[101] Therefore, the graphene derived from pyrolysis and exfoliation of chitosan is a type of defective N-doped graphene, in which two types of major nitrogen atoms, pyridinic or graphitic N, are the main constituents of the N families.[102] **Scheme 1.9** illustrates the formation process of the N, P-codoped graphitic carbon through the pyrolysis of a mixture of chitosan and phytic acid.

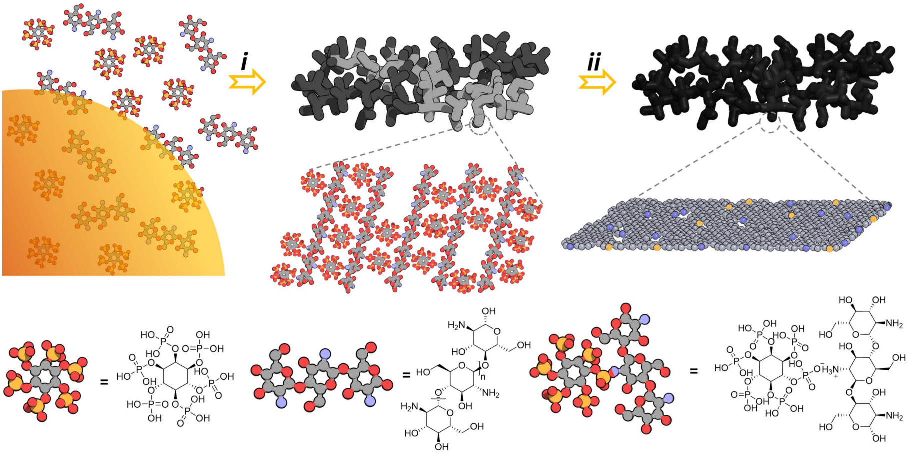

Scheme 1.9. Illustration of the formation of N, P-codoped graphitic carbon. *i*: mixture of phytic acid and chitosan; *ii*: pyrolysis in argon.

While graphene behaves as a zero-band semiconductor with the electron mobility on the sheet is even higher than in copper or other metals, the presence of N and other defects decreases the electrical conductivity. Therefore, semi-conductivity carbons can be prepared by nitrogen doping. Due to the presence of nitrogen, the semiconductivity is responsible for its electrocatalytic activity, favoring electrochemical processes such as oxygen generation and water electrolysis.[103]

Related to the topic of the present Doctoral Thesis, pyridinic nitrogen can establish strong interactions with metal atoms and nanoparticles. It is also reported that the existence of a extended π cloud on the graphene layers is suitable for interaction with d orbitals of the transition metals. Furthermore, graphene could also provide additional catalytic sites and contribute to the catalytic activity during oxidation and reduction reactions.[104] Therefore, N-doped defective graphene has been reported as a suitable support for metal nanoparticles, especially for transition metals.[105-108]

1.4.4.2 Precedents from our group

An appropriate procedure developed by our group to obtain metal nanoparticles strongly adhered to defective graphene is shown in **Scheme 1.10**. The procedure is based on the high adsorption capacity of polysaccharides and the chemical reduction of transition metals during the pyrolysis. The well-known property of chitosan and other polysaccharides is their ability to adsorb a high percentage of metal salts from aqueous solutions due to the formation of strong hydrogen bridges between the hydrated metal cations and the polysaccharides fibrits. In the folded polysaccharide chain, adsorbed metals undergo chemical reduction to the metallic state during the high-temperature pyrolysis. Our group has reported the formation of metal nanoparticles supported on graphene which have been used as catalysts for different reactions including photo-assisted methanation,[109] gas phase CO_2 reduction with hydrogen,[110] overall water splitting.[104] **Scheme 1.11** illustrates some nanoparticles supported on defective graphene prepared by pyrolysis of polysaccharides.

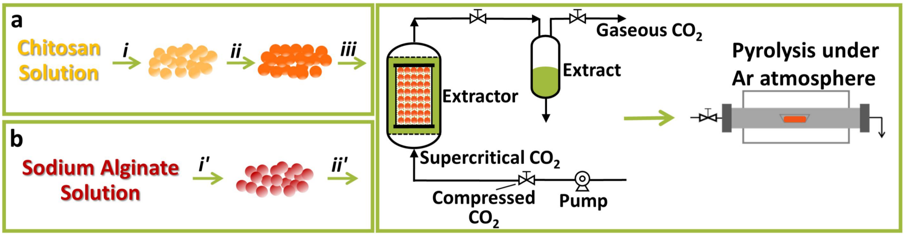

Scheme 1.10. Procedure used to prepare metal nanoparticles supported on graphene based on the high absorption capacity of polysaccharides.

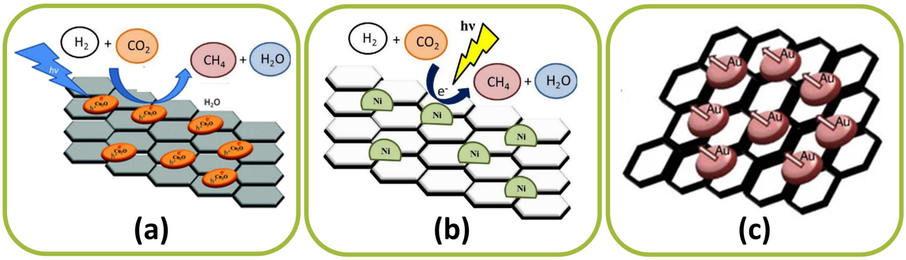

Scheme 1.11. Illustration of different metal nanoparticles supported on defective graphene prepared by pyrolysis of polysaccharides containing metal salts. (**a**: Cu_2O NPs; **b**: NiO/Ni NPs; **c**: 111 oriented gold NPs.) [104, 109, 110]

In the present PhD Thesis, previous preparation procedures and chitosan as a precursor will be used to develop a series of catalysts for selective CO_2 hydrogenation. As it will be commented in the following Chapters, before pyrolysis, an immediate supercritical CO_2 drying will be included. The reason for this intermediate step is to achieve the largest possible surface area of graphitic carbons formed in pyrolysis. Numerous studies indicate that polysaccharides containing a significant percentage of water, denoted as hydrates, become dense solids with a minor surface area due to the formation hydrogen bridges taking place on the polysaccharide. The surface area of these dense form of the polysaccharide upon dehydration is much below 100 $m^2 \cdot g^{-1}$ and typically about 50 $m^2 \cdot g^{-1}$. In contrast, if the hydrated form is converted into the alcogel form by the gradual replacement of water by ethanol, the resulting alcogel renders an aerogel of a very high surface area by removing ethanol using supercritical CO_2 drying. CO_2 is able to dissolve ethanol, but not water. Therefore, it is necessary to convert the hydrogel into alcogel. The specific surface area of the aerogel obtained following the supercritical CO_2 drying is over 400 $m^2 \cdot g^{-1}$ and in some cases, close to 500 $m^2 \cdot g^{-1}$. Scanning electron microscopy (SEM) images, shown in **Figure 1.6** reveal the different morphology of graphitic carbons obtained from the pyrolysis of the dry hydrogel form and the alcogel form of chitosan.

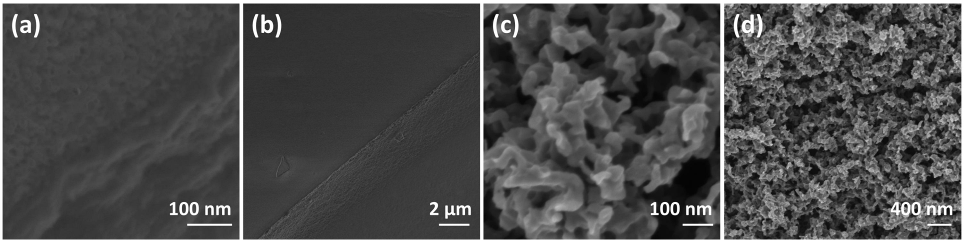

Figure 1.6. SEM images of graphene obtained from the pyrolysis of dry hydrogel form (**a**, **b**) and alcogel form (**c**, **d**) of chitosan.

1.4.5 Effect of metal particle size

In addition to the influence of the support, the particle size also remarkably affects the catalytic performance for CO_2 hydrogenation. It is found that when Ni@SiO_2 is used as catalyst in CO_2 methanation, CO formation is favored on small Ni clusters, while more CH_4 is formed on large Ni particles. This behavior is illustrated in **Scheme 1.12**, **a**.[111] A similar phenomenon was also observed on Rh@TiO_2 catalysts for CO_2 hydrogenation (**Scheme 1.12**, **b**).[112] In the case of Fe-based catalysts for CO_2 hydrogenation, with a particle size range of 2.5 to 12.9 nm, the overall selectivity of C_{2+} hydrocarbons increases continuously, while that of CO decreases with the increase in the particle size and more CH_4 is produced as a primary product on larger particles. Therefore, the geometric or ensemble effect on larger particles leads to a higher chain-growth probability for the reaction products, as shown in **Scheme 1.12**, **c**.[113] The results of both noble and non-noble metal-based catalysts for CO_2 hydrogenation indicate that, within a certain range of metal particle size, structuration at the atom-scale of the catalyst surface tend to favor the RWGS reaction, while the larger metal particles promote the formation of CH_4 and C_{2+} hydrocarbons.

As reported on the literature, the particle size distribution of the metal nanoparticles have significant influence on the selectivity of the catalysts in CO_2 hydrogenation. In the present PhD Thesis, different Co, Fe and Co-Fe alloy supported on N-doped defective graphene within a certain range of particle size were prepared in order to explore the influences of particle size on the selectivity of CO_2

hydrogenation at high conversions.

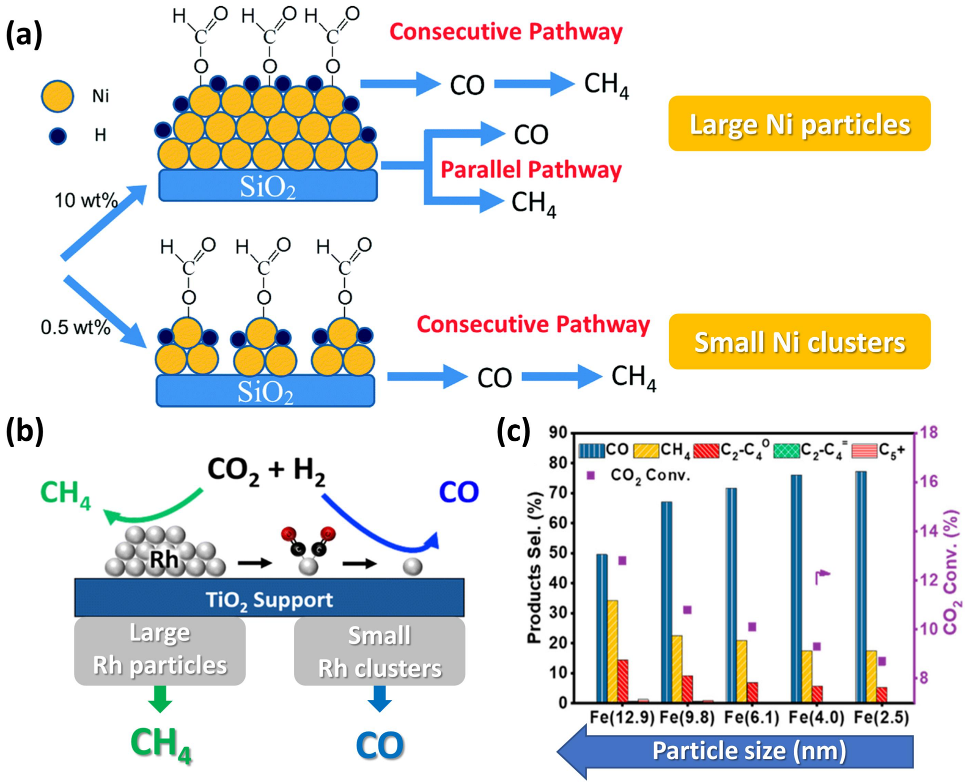

Scheme 1.12. Schematic illustration of the particle size effect on CO_2 hydrogenation over metal supported catalysts. (**a**: Ni@SiO_2; **b**: Rh@TiO_2; **c**: Influence of Fe nanoparticle average size on the product distribution in CO_2 hydrogenation.)[111-113]

1.4.6 Influence of promoters and poisons

It is well known that the catalytic activity and selectivity of active sites can be modulated by the presence of small amounts of other elements acting as promoters or poisons. Typical promoters in oxidation and hydrogenation are alkali and alkaline earth metals, such as sodium,[114] potassium,[115] calcium,[116] and cerium[117] which can increase the basicity of the support around the active metallic sites and the electron density on the metal-support interface. It has been reported that the addition of K and Na can increase the CO_2 conversion and result in a remarkable shift to longer chain hydrocarbons and the formation of olefin.[114] The presence of K has been proposed to promote CO_2 chemisorption while impeding H_2 adsorption, which could enhance the probability of C-C bond formation.[115] Another well-known example is the Pd-promoted catalysts for CO_2 hydrogenation,[118] in which the presence of oxygen leads to a decrease of the Pd activity, driving the reaction selectivity towards alkenes by partial hydrogenation of C-C. It is also been found that the presence the minute amount of noble metal can increase the activity of alkali metals by a significant effect, in which the small proportion of noble metal activates the molecular hydrogen breaking H-H bond and subsequently transferring the H atoms to the alkali metal. On the other hand, poisons such as S,[119] can moderate the hydrogenation activity of the most highly active sites altering the selectivity of the reaction. In the present PhD Thesis, different Co-Fe alloy NPs supported on defective graphene containing promoters such as Na, K, Ce Pd as well as a poison such as S were prepared in order to determine the influence of promoters and poisons on the selectivity of catalytic CO_2 hydrogenation.

As briefly described in the above paragraphs, the present PhD Thesis deals with the preparation and catalytic performance of a series of metal nanoparticles supported on defective N-doped defective graphene for CO_2 hydrogenation. By control of particle size and compositions, different value-added products as chemicals and fuels can be obtained. These studies are relevant to decrease the atmospheric CO_2 emissions and cover the shortage of dwindling fossil fuels, meanwhile adding value to carbon dioxide.

CHAPTER 1

References

[1] F.A. Macdonald, N.L. Swanson-Hysell, Y. Park, L. Lisiecki, O. Jagoutz, Arc-continent collisions in the tropics set Earth's climate state, *Science*, 364 **(2019)** 181-184.

[2] J. Ehlers, P. Gibbard, Encyclopedia of snow, ice and glaciers, Quaternary glaciation, **(2011)** 873-882.

[3] J.P. Severinghaus, E.J. Brook, Abrupt climate change at the end of the last glacial period inferred from trapped air in polar ice, *Science*, 286 **(1999)** 930-934.

[4] V. Acocella, G. Puglisi, Hazard mitigation of unstable volcanic edifices, *Eos Trans. Amer. Geophys. Union*, 91 **(2010)** 357-358.

[5] Best Clive, The Anglian Glaciation, **(2016)**. Available at: http://clivebest.com/blog/?p=7089.

[6] J.W. Rae, Y.G. Zhang, X. Liu, G.L. Foster, H.M. Stoll, R.D. Whiteford, Atmospheric CO_2 over the past 66 million years from marine archives, *Annu. Rev. Earth Planet. Sci.*, 49 **(2021)**.

[7] Global Monitoring Laboratory, Trends in atmospheric carbon dioxide, **(2021)**. Available at: https://www.esrl.noaa.gov/gmd/ccgg/trends/.

[8] B. Hileman, Ice core record extended, *Chem. Eng. News*, 83 **(2005)**.

[9] T. Machida, T. Nakazawa, Y. Fujii, S. Aoki, O. Watanabe, Increase in the atmospheric nitrous oxide concentration during the last 250 years, *Geophys. Res. Lett.*, 22 **(1995)** 2921-2924.

[10] S. Menon, K.L. Denman, G. Brasseur, A. Chidthaisong, P. Ciais, P.M. Cox, R.E. Dickinson, D. Hauglustaine, C. Heinze, E. Holland, Couplings between changes in the climate system and biogeochemistry, Lawrence Berkeley National Lab.(LBNL), Berkeley, CA (United States), **(2007)** 500-587.

[11] V. Smil, The Earth's biosphere: Evolution, dynamics, and change, Mit Press **(2003)** 107.

[12] V. Kind, Pedagogical content knowledge in science education: perspectives and potential for progress, *Stud. Sci. Educ.*, 45 **(2009)** 169-204.

[13] Climate Change 2013: Intergovernmental panel on climate change, Fifth Assessment Report (AR5), 13 **(2013)** 731.

[14] A. Kukreti, A.K. Painolli, N. Rana, Where do we stand: factors effecting sustainable development, **(2021)**.

[15] B.K. Sovacool, S.H. Ali, M. Bazilian, B. Radley, B. Nemery, J. Okatz, D.J.S. Mulvaney, Sustainable minerals and metals for a low-carbon future, *Scicence*, 367 **(2020)** 30-33.

[16] UNFCCC, Decision 1/CP.21: Adoption of the Paris Agreement. Paris Climate Change Conference, **(2015)**.

[17] D. Bodansky, The Copenhagen climate change conference: a postmortem, *Am. J. Int. Law*, 104 **(2010)** 230-240.

[18] A. Haines, P. Scheelbeek, European Green Deal: a major opportunity for health improvement, *Lancet*, 395 **(2020)** 1327-1329.

[19] H. Yang, C. Zhang, P. Gao, H. Wang, X. Li, L. Zhong, W. Wei, Y. Sun, A review of the catalytic hydrogenation of carbon dioxide into value-added hydrocarbons, *Catal. Sci. Technol.*, 7 **(2017)** 4580-4598.

[20] E.E. Benson, C.P. Kubiak, A.J. Sathrum, J.M. Smieja, Electrocatalytic and homogeneous approaches to conversion of CO_2 to liquid fuels, *Chem. Soc. Rev.*, 38 **(2009)** 89-99.

[21] M. Xu, A.R. Jupp, M.S. Ong, K.I. Burton, S.S. Chitnis, D.W. Stephan, Synthesis of urea derivatives from CO_2 and silylamines, *Angew. Chem. Int. Ed.*, 58 **(2019)** 5707-5711.

[22] T. Chang, M. Tamura, Y. Nakagawa, N. Fukaya, J. C. Choi, T. Mishima, S. Matsumoto, S. Hamura, K. Tomishige, An effective combination catalyst of CeO_2 and zeolite for the direct synthesis of diethyl carbonate from CO_2 and ethanol with 2,

2-diethoxypropane as a dehydrating agent, *Green Chem.*, 22 **(2020)** 7321-7327.

[23] X. Zhang, G. Zhang, W. Liu, F. Yuan, J. Wang, J. Zhu, X. Jiang, A. Zhang, F. Ding, C. Song, Reaction-driven surface reconstruction of $ZnAl_2O_4$ boosts the methanol selectivity in CO_2 catalytic hydrogenation, *Appl. Catal. B*, 284 **(2021)** 119700.

[24] F. Zeng, C. Mebrahtu, X. Xi, L. Liao, J. Ren, J. Xie, H.J. Heeres, R. Palkovits, Catalysts design for higher alcohols synthesis by CO_2 hydrogenation: Trends and future perspectives, *Appl. Catal. B*, 291 **(2021)** 120073.

[25] G. Centi, S. Perathoner, CO_2-based energy vectors for the storage of solar energy, *Greenh. Gases*, 1 **(2011)** 21-35.

[26] T. Schaub, R.A. Paciello, A process for the synthesis of formic acid by CO_2 hydrogenation: thermodynamic aspects and the role of CO, *Angew. Chem. Int. Ed.*,50 **(2011)** 7278-7282.

[27] M. Ronda-Lloret, L. Yang, M. Hammerton, V.S. Marakatti, M. Tromp, Z.k. Sofer, A. Sepúlveda-Escribano, E.V. Ramos-Fernandez, J.J. Delgado, G. Rothenberg, Molybdenum oxide supported on Ti_3AlC_2 is an active reverse water-gas shift catalyst, *ACS Sustain. Chem. Eng.*, 14 **(2021)** 4957-4966.

[28] F. Bustamante, R.M. Enick, A.V. Cugini, R.P. Killmeyer, B.H. Howard, K.S. Rothenberger, M. Ciocco, B. Morreale, S. Chattopadhyay, S. Shi, High-temperature kinetics of the homogeneous reverse water-gas shift reaction, *AIChE J.*, 50 **(2004)** 1028-1041.

[29] Y. Hartadi, D. Widmann, R.J. Behm, Methanol formation by CO_2 hydrogenation on Au/ZnO catalysts-effect of total pressure and influence of CO on the reaction characteristics, *J. Catal.*, 333 **(2016)** 238-250.

[30] M. Poutsma, L. Elek, P. Ibarbia, A. Risch, J. Rabo, Selective formation of methanol from synthesis gas over palladium catalysts, *J. Catal.*, 52 **(1978)** 157-168.

[31] M. Cui, Q. Qian, J. Zhang, Y. Wang, B.B.A. Bediako, H. Liu, B. Han, Liquid fuel synthesis *via* CO_2 hydrogenation by coupling homogeneous and heterogeneous

catalysis, *Chem*, 7 **(2021)** 726-737.

[32] N. Chen, W. Reagan, Evidence of autocatalysis in methanol to hydrocarbon reactions over zeolite catalysts, *J. Catal.*, 59 **(1979)** 123-129.

[33] J. Zhong, J. Han, Y. Wei, Z. Liu, Catalysts and shape selective catalysis in the methanol-to-olefin (MTO) reaction, *J. Catal.*, 396 **(2021)** 23-31.

[34] C.D. Chang, J.C. Kuo, W.H. Lang, S.M. Jacob, J.J. Wise, A. Silvestri, Process studies on the conversion of methanol to gasoline, *Ind. Eng. Chem. Process. Des. Dev.*, 17 **(1978)** 255-260.

[35] I. Pinilla-Herrero, E. Borfecchia, T. Cordero-Lanzac, U.V. Mentzel, F. Joensen, K.A. Lomachenko, S. Bordiga, U. Olsbye, P. Beato, S. Svelle, Finding the active species: The conversion of methanol to aromatics over Zn-ZSM-5/alumina shaped catalysts, *J. Catal.*, 394 **(2021)** 416-428.

[36] C. Wang, Y. Chu, J. Xu, Q. Wang, G. Qi, P. Gao, X. Zhou, F. Deng, Extra-framework aluminum-assisted initial C-C bond formation in methanol-to-olefins conversion on zeolite H-ZSM-5, *Angew. Chem.,* 130 **(2018)** 10354-10358.

[37] F. Xiong, Y.Y. Yu, Z. Wu, G. Sun, L. Ding, Y. Jin, X.Q. Gong, W. Huang, Methanol conversion into dimethyl ether on the anatase TiO_2 (001) surface, *Angew. Chem.,* 128 **(2016)** 633-638.

[38] Y. Wang, S. Kazumi, W. Gao, X. Gao, H. Li, X. Guo, Y. Yoneyama, G. Yang, N. Tsubaki, Direct conversion of CO_2 to aromatics with high yield *via* a modified Fischer-Tropsch synthesis pathway, *Appl. Catal. B,* 269 **(2020)** 118792.

[39] Y. Yan, Y. Dai, H. He, Y. Yu, Y. Yang, A novel W-doped Ni-Mg mixed oxide catalyst for CO_2 methanation, *Appl. Catal. B,* 196 **(2016)** 108-116.

[40] M. Götz, J. Lefebvre, F. Mörs, A.M. Koch, F. Graf, S. Bajohr, R. Reimert, T. Kolb, Renewable power-to-gas: A technological and economic review, *Renew. Energ.*, 85 **(2016)** 1371-1390.

[41] M.B. Choudhury, S. Ahmed, M.A. Shalabi, T. Inui, Preferential methanation of

CO in a syngas involving CO_2 at lower temperature range, *Appl. Catal. A*, 314 **(2006)** 47-53.

[42] R. Heryadi, S.M. Nur, Techno economic analysis of biomass to methanol plant vased on gasification of palm empty fruit bunch, E3S Web of Conferences, EDP Sciences, **(2021)**, 40.

[43] M. Garside, Global production capacity of methanol 2018-2030, **(2020)**. Available at: https://www.statista.com/statistics/1065891/global-methanol-production-capacity/.

[44] X. Xu, X. Zhang, Z. Xia, R. Sun, J. Wang, Q. Jiang, S. Yu, S. Wang, G. Sun, Fe-N-C with Intensified Exposure of Active Sites for Highly Efficient and Stable Direct Methanol Fuel Cells, *ACS Appl. Mater. Interfaces*, 14 **(2021)** 16279-16288.

[45] J. Andersson, S. Grönkvist, Large-scale storage of hydrogen, *Int. J. Hydrog. Energy*, 44 **(2019)** 11901-11919.

[46] G. Thomas, G. Parks, Washington, DC, Potential roles of ammonia in a hydrogen economy: a study of issues related to the use ammonia for on-board vehicular hydrogen storage, US Department of Energy, Washington, DC **(2006)**.

[47] C. Zamfirescu, I. Dincer, Using ammonia as a sustainable fuel, *J. Power Sources*, 185 **(2008)** 459-465.

[48] S. Verhelst, J.W. Turner, L. Sileghem, J. Vancoillie, Methanol as a fuel for internal combustion engines, *Prog. Energy Combust. Sci*.,70 **(2019)** 43-88.

[49] F. Xiao, Y.C. Wang, Z.P. Wu, G. Chen, F. Yang, S. Zhu, K. Siddharth, Z. Kong, A. Lu, C. Zhong, Z. Zhou, M. Shao, Recent advances in electrocatalysts for proton exchange membrane fuel cells and alkaline membrane fuel cells, *Adv. Mater.*, **(2021)** 2006292.

[50] N. Garg, S. Paira, B. Sundararaju, Efficient transfer hydrogenation of ketones using methanol as liquid organic hydrogen carrier, *ChemCatChem*, 12 **(2020)** 472-3476.

[51] K. Klier, V. Chatikavanij, R. Herman, G. Simmons, Catalytic synthesis of methanol from COH_2: IV. The effects of carbon dioxide, *J. Catal.*, 74 **(1982)** 343-360.

[52] G. Prieto, Carbon dioxide hydrogenation into higher hydrocarbons and oxygenates: Thermodynamic and kinetic bounds and progress with heterogeneous and homogeneous catalysis, *ChemSusChem*, 10 **(2017)** 1056-1070.

[53] C. Vogt, M. Monai, E.B. Sterk, J. Palle, A.E. Melcherts, B. Zijlstra, E. Groeneveld, P.H. Berben, J.M. Boereboom, E.J. Hensen, Understanding carbon dioxide activation and carbon-carbon coupling over nickel, *Nat. Commun.*, 10 **(2019)** 1-10.

[54] X. Wang, C. Zeng, N. Gong, T. Zhang, Y. Wu, J. Zhang, F. Song, G. Yang, Y. Tan, Effective suppression of CO selectivity for CO_2 hydrogenation to high-quality gasoline, *ACS Catal.*, 11 **(2021)** 1528-1547.

[55] H.M.T. Galvis, J.H. Bitter, C.B. Khare, M. Ruitenbeek, A.I. Dugulan, K.P. de Jong, Supported iron nanoparticles as catalysts for sustainable production of lower olefins, *Science*, 335 **(2012)** 835-838.

[56] R. P. Ye, J. Ding, W. Gong, M.D. Argyle, Q. Zhong, Y. Wang, C.K. Russell, Z. Xu, A.G. Russell, Q. Li, CO_2 hydrogenation to high-value products *via* heterogeneous catalysis, *Nat. Commun.*,10 **(2019)** 1-15.

[57] A. Corma, H. García, Lewis acids as catalysts in oxidation reactions: from homogeneous to heterogeneous systems, *Chem. Rev.*, 102 **(2002)** 3837-3892.

[58] V. Dieterich, A. Buttler, A. Hanel, H. Spliethoff, S. Fendt, Power-to-liquid *via* synthesis of methanol, DME or Fischer-Tropsch-fuels: a review, *Energy Environ. Sci.*, 13 **(2020)** 3207-3252.

[59] J. Tu, H. Wu, Q. Qian, S. Han, M. Chu, S. Jia, R. Feng, J. Zhai, M. He, B. Han, Low temperature methanation of CO_2 over an amorphous cobalt-based catalyst, *Chem. Sci.*,12 **(2021)** 3937-3943.

[60] Y. Li, Y. Men, S. Liu, J. Wang, K. Wang, Y. Tang, W. An, X. Pan, L. Li, Remarkably efficient and stable Ni/Y_2O_3 catalysts for CO_2 methanation: Effect citric acid addition,

Appl. Catal. B, **(2021)** 120206.

[61] E.M. Petersen, R.G. Rao, B.C. Vance, J.-P.l. Tessonnier, SiO_2/SiC supports with tailored thermal conductivity to reveal the effect of surface temperature on Ru-catalyzed CO_2 methanation, *Appl. Catal. B*, 286 **(2021)** 119904.

[62] M. Paviotti, B. Faroldi, L. Cornaglia, Ni-based catalyst over rice husk-derived silica for the CO_2 methanation reaction: Effect of Ru addition, *J. Environ. Chem. Eng.*, 9 **(2021)** 105173.

[63] K. Wang, W. Li, J. Huang, J. Huang, G. Zhan, Q. Li, Enhanced active site extraction from perovskite $LaCoO_3$ using encapsulated PdO for efficient CO_2 methanation, *J. Energy Chem.*, 53 **(2021)** 9-19.

[64] R.P. Ye, L. Liao, T.R. Reina, J. Liu, D. Chevella, Y. Jin, M. Fan, J. Liu, Engineering Ni/SiO_2 catalysts for enhanced CO_2 methanation, *Fuel*, 285 **(2021)** 119151.

[65] BASF, US Patent 1,569,775, 1923.

[66] B.A. Peppley, J.C. Amphlett, L.M. Kearns, R.F. Mann, Methanol-steam reforming on Cu/ZnO/Al_2O_3. Part 1: the reaction network, *Appl. Catal. A*, 179 **(1999)** 21-29.

[67] M. Zabilskiy, V.L. Sushkevich, D. Palagin, M.A. Newton, F. Krumeich, J.A. van Bokhoven, The unique interplay between copper and zinc during catalytic carbon dioxide hydrogenation to methanol, *Nat. Commun*., 11 **(2020)** 1-8.

[68] M.D. Rhodes, A.T. Bell, The effects of zirconia morphology on methanol synthesis from CO and H_2 over Cu/ZrO_2 catalysts: Part I. Steady-state studies, *J. Catal.*, 233 **(2005)** 198-209

[69] K. Samson, M. Sliwa, R.P. Socha, K. Góra-Marek, D. Mucha, D. Rutkowska-Zbik, J. Paul, M. Ruggiero-Mikołajczyk, R. Grabowski, J. Słoczynski, Influence of ZrO_2 structure and copper electronic state on activity of Cu/ZrO_2 catalysts in methanol synthesis from CO_2, *ACS Catal.*, 4 **(2014)** 3730-3741.

[70] B. Rungtaweevoranit, J. Baek, J.R. Araujo, B.S. Archanjo, K.M. Choi, O.M. Yaghi, G.A. Somorjai, Copper nanocrystals encapsulated in Zr-based metal-organic

frameworks for highly selective CO_2 hydrogenation to methanol, *Nano letters*, 16 **(2016)** 7645-7649.

[71] E.M. Fiordaliso, I. Sharafutdinov, H.W. Carvalho, J.-D. Grunwaldt, T.W. Hansen, I. Chorkendorff, J.B. Wagner, C.D. Damsgaard, Intermetallic $GaPd_2$ nanoparticles on SiO_2 for low-pressure CO_2 hydrogenation to methanol: Catalytic performance and in situ characterization, *ACS Catal.*, 5 **(2015)** 5827-5836.

[72] T. Toyao, S. Kayamori, Z. Maeno, S.H. Siddiki, K. Shimizu, Heterogeneous Pt and MoO_x Co-loaded TiO_2 catalysts for low-temperature CO_2 hydrogenation to form CH_3OH, *ACS Catal.*, 9 **(2019)** 8187-8196.

[73] X. Yang, S. Kattel, S.D. Senanayake, J.A. Boscoboinik, X. Nie, J.s. Graciani, J.A. Rodriguez, P. Liu, D.J. Stacchiola, J.G. Chen, Low pressure CO_2 hydrogenation to methanol over gold nanoparticles activated on a CeO_x/TiO_2 interface, *J. Am. Chem. Soc.*, 137 **(2015)** 10104-10107.

[74] K. Sun, Z. Fan, J. Ye, J. Yan, Q. Ge, Y. Li, W. He, W. Yang, C. Liu, Hydrogenation of CO_2 to methanol over In_2O_3 catalyst, *J. CO_2 Util.*,12 **(2015)** 1-6.

[75] D. Li, C. Lan, A. Manikandan, S. Yip, Z. Zhou, X. Liang, L. Shu, Y.L. Chueh, N. Han, J.C. Ho, Ultra-fast photodetectors based on high-mobility indium gallium antimonide nanowires, *Nat. Commun.*, 10 **(2019)** 1-10.

[76] W. Zhou, K. Cheng, J. Kang, C. Zhou, V. Subramanian, Q. Zhang, Y. Wang, New horizon in C_1 chemistry: breaking the selectivity limitation in transformation of syngas and hydrogenation of CO_2 into hydrocarbon chemicals and fuels, *Chem. Soc. Rev.*, 48 **(2019)** 3193-3228.

[77] S. Liang, C. Hao, Y. Shi, The power of single-atom catalysis, *ChemCatChem*, 7 **(2015)** 2559-2567.

[78] T.S. Galhardo, A.H. Braga, B.H. Arpini, J. Szanyi, R.V. Gonçalves, B.F. Zornio, C.R. Miranda, L.M. Rossi, Optimizing active sites for high CO selectivity during CO_2 hydrogenation over supported nickel catalysts, *J. Am. Chem. Soc.*, 143 **(2021)**

4268-4280.

[79] S. M. Hwang, S.J. Han, H.G. Park, H. Lee, K. An, K. W. Jun, S.K. Kim, Atomically alloyed Fe-Co catalyst derived from a N-voordinated Co single-atom structure for CO_2 hydrogenation, *ACS Catal.*, 11 **(2021)** 2267-2278.

[80] D. Ray, P. Chawdhury, K. Bhargavi, S. Thatikonda, N. Lingaiah, C. Subrahmanyam, Ni and Cu oxide supported γ-Al_2O_3 packed DBD plasma reactor for CO_2 activation, *J. CO_2 Util.*, 44 **(2021)** 101400.

[81] J. Yu, S. Liu, X. Mu, G. Yang, X. Luo, E. Lester, T. Wu, Cu-ZrO_2 catalysts with highly dispersed Cu nanoclusters derived from ZrO_2@HKUST-1 composites for the enhanced CO_2 hydrogenation to methanol, *Chem. Eng. J.*, 419 **(2021)** 129656.

[82] H. Zhang, Y. Li, J. Wang, N. Wu, H. Sheng, C. Chen, J. Zhao, An unprecedent hydride transfer pathway for selective photocatalytic reduction of CO_2 to formic acid on TiO_2, *Appl. Catal. B*, 284 **(2021)** 119692.

[83] J. Zhu, D. Ciolca, L. Liu, A. Parastaev, N. Kosinov, E. Hensen, Flame Synthesis of Cu/ZnO-CeO_2 catalysts: Synergistic metal-support interactions promote CH_3OH selectivity in CO_2 hydrogenation, *ACS Catal.*, 11 **(2021)** 4880-4892.

[84] T. Zurrer, K. Wong, J. Horlyck, E.C. Lovell, J. Wright, N.M. Bedford, Z. Han, K. Liang, J. Scott, R. Amal, Mixed-metal MOF-74 templated catalysts for efficient carbon dioxide capture and methanation, *Adv. Func. Mater.*, 31 **(2021)** 2007624.

[85] N.R. Bennedsen, D.B. Christensen, R.L. Mortensen, B. Wang, R. Wang, S. Kramer, S. Kegnæs, Heterogeneous formic acid production by hydrogenation of CO_2 catalyzed by Ir-bpy embedded in polyphenylene porous organic polymers, *ChemCatChem*, 13 **(2021)** 781-1786.

[86] L. Dai, Y. Chen, R. Liu, X. Li, N. Ullah, Z. Li, CO_2 hydrogenation to C_{5+} hydrocarbons over K-promoted Fe/CNT catalyst: Effect of potassium on structure-activity relationship, *J. Organomet. Chem.*, 6253.

[87] V. Deerattrakul, N. Yigit, G. Rupprechter, P. Kongkachuichay, The roles of

nitrogen species on graphene aerogel supported Cu-Zn as efficient catalysts for CO_2 hydrogenation to methanol, *Appl. Catal. A*, 580 **(2019)** 46-52.

[88] Y. Zhang, Z. R. Tang, X. Fu, Y. J. Xu, TiO_2-graphene nanocomposites for gas-phase photocatalytic degradation of volatile aromatic pollutant: is TiO_2-graphene truly different from other TiO_2-carbon composite materials?, *ACS Nano*, 4 **(2010)** 7303-7314.

[89] Y. Gao, S. Liu, Z. Zhao, H. Tao, Z. Sun, Heterogeneous catalysis of CO_2 hydrogenation to C_{2+} products, *Acta Phys. Chim. Sin.*, 34 **(2018)** 858-872.

[90] L.M. Chew, P. Kangvansura, H. Ruland, H.J. Schulte, C. Somsen, W. Xia, G. Eggeler, A. Worayingyong, M. Muhler, Effect of nitrogen doping on the reducibility, activity and selectivity of carbon nanotube-supported iron catalysts applied in CO_2 hydrogenation, *Appl. Catal. A*, 482 **(2014)** 163-170.

[91] A. Geim, Graphene prehistory, *Phys. Scr.*, T146 **(2012)** 14003.

[92] A. Hull, Crystal structure of alpha-iron, *Phys. Rev.*, 10 **(1917)** 661-696.

[93] J.D. Bernal, The structure of graphite, *Proceedings of the Royal Society of London. Series A*, 106 **(1924)** 749-773.

[94] H.P. Boehm, A. Clauss, G. Fischer, U. Hofmann, Surface properties of extremely thin graphite lamellae, Proceedings of the fifth conference on carbon, Pergamon Press New York, **(1962)** 73-80.

[95] S. Mouras, A. Hamm, D. Djurado, J. Cousseins, Synthesis of first stage graphite intercalation compounds with fluorides, *Revue de chimie minérale*, 24 **(1987)** 572-582.

[96] J. Y. Huang, F. Ding, B.I. Yakobson, P. Lu, L. Qi, J. Li, In situ observation of graphene sublimation and multi-layer edge reconstructions, *Proc. Nat. Acad. Sci.*, 106 **(2009)** 10103-10108.

[97] M.J. McAllister, J L. Li, D.H. Adamson, H.C. Schniepp, A.A. Abdala, J. Liu, M. Herrera-Alonso, D.L. Milius, R. Car, R.K. Prud'homme, Single sheet functionalized

graphene by oxidation and thermal expansion of graphite, *Chem. Mater.*, 19 **(2007)** 4396-4404.

[98] M. M. Trandafir, M. Florea, F. Neaţu, A. Primo, V. I. Parvulescu, H. García, Graphene from alginate pyrolysis as a metal-free catalyst for hydrogenation of nitro compounds, *ChemsusChem*, 9 **(2016)** 1565-1569.

[99] A. Primo, P. Atienzar, E. Sanchez, J.M. Delgado, H. García, From biomass wastes to large-area, high-quality, N-doped graphene: catalyst-free carbonization of chitosan coatings on arbitrary substrates, *Chem. Comm.*, 48 **(2012)** 9254-9256.

[100] M. Latorre-Sánchez, A. Primo, H. García, P-doped graphene obtained by pyrolysis of modified alginate as a photocatalyst for hydrogen generation from water-methanol mixtures, *Angew. Chem. Int. Ed.*, 52 **(2013)** 11813-11816.

[101] J. He, A. Anouar, A. Primo, H. García, Quality improvement of few-layers defective graphene from biomass and application for H_2 generation, *Nanomater.*, 9 **(2019)** 895.

[102] A. Primo, E. Sánchez, J.M. Delgado, H. García, High-yield production of N-doped graphitic platelets by aqueous exfoliation of pyrolyzed chitosan, *Carbon*, 68 **(2014)** 777-783.

[103] M. Latorre-Sánchez, I. Esteve-Adell, A. Primo, H. García, Innovative preparation of MoS_2-graphene heterostructures based on alginate containing $(NH_4)_2MoS_4$ and their photocatalytic activity for H_2 generation, *Carbon*, 81 **(2015)** 587-596.

[104] D. Mateo, I. Esteve-Adell, J. Albero, J. F. S. Royo, A. Primo, H. Garcia, 111 oriented gold nanoplatelets on multilayer graphene as visible light photocatalyst for overall water splitting, *Nat. Commun.*, 7 **(2016)** 1-8.

[105] G. Abellán, M. Latorre-Sánchez, V. Fornés, A. Ribera, H. García, Graphene as a carbon source effects the nanometallurgy of nickel in Ni, Mn layered double hydroxide-graphene oxide composites, *Chem. Comm.*, 48 **(2012)** 11416-11418.

[106] M. Latorre-Sanchez, P. Atienzar, G. Abellan, M. Puche, V. Fornés, A. Ribera, H.

García, The synthesis of a hybrid graphene-nickel/manganese mixed oxide and its performance in lithium-ion batteries, *Carbon*, 50 **(2012)** 518-525.

[107] A. Primo, I. Esteve-Adell, J.F. Blandez, A. Dhakshinamoorthy, M. Álvaro, N. Candu, S.M. Coman, V.I. Parvulescu, H. García, High catalytic activity of oriented 2.0.0 Copper(I) oxide grown on graphene film, *Nat. Commun.*, 6 **(2015)** 1-11.

[108] J. He, A. Dhakshinamoorthy, A.M. Primo Arnau, H. García Gómez, Iron nanoparticles embedded in graphitic carbon matrix as heterogeneous catalysts for the oxidative CN coupling of aromatic NH compounds and amides, *ChemCatChem*, 9 **(2017)** 3003-3012.

[109] D. Mateo, J. Albero, H. García, Photoassisted methanation using Cu_2O nanoparticles supported on graphene as a photocatalyst, *Energy Environ. Sci.*, 10 **(2017)** 2392-2400.

[110] D. Mateo, J. Albero, H. Garcia, Graphene supported NiO/Ni nanoparticles as efficient photocatalyst for gas phase CO_2 reduction with hydrogen, *Appl. Catal. B*, 224 **(2018)** 563-571.

[111] H. Wu, Y. Chang, J. Wu, J. Lin, I. Lin, C. Chen, Methanation of CO_2 and reverse water gas shift reactions on Ni/SiO_2 catalysts: the influence of particle size on selectivity and reaction pathway, *Catal. Sci. Technol.*, 5 **(2015)** 4154-4163.

[112] J.C. Matsubu, V.N. Yang, P. Christopher, Isolated metal active site concentration and stability control catalytic CO_2 reduction selectivity, *J. Am. Chem. Soc.*, 137 **(2015)** 3076-3084.

[113] J. Zhu, G. Zhang, W. Li, X. Zhang, F. Ding, C. Song, X. Guo, Deconvolution of the particle size effect on CO_2 hydrogenation over iron-based catalysts, *ACS Catal.*, 10 **(2020)** 7424-7433.

[114] P.H. Choi, K.W. Jun, S.J. Lee, M.J. Choi, K.W. Lee, Hydrogenation of carbon dioxide over alumina supported Fe-K catalysts, *Catal. Letters*, 40 **(1996)** 115-118.

[115] T. Numpilai, T. Witoon, N. Chanlek, W. Limphirat, G. Bonura, M. Chareonpanich,

J. Limtrakul, Structure-activity relationships of Fe-Co/K-Al_2O_3 catalysts calcined at different temperatures for CO_2 hydrogenation to light olefins, *Appl. Catal. A*, 547 **(2017)** 219-229.

[116] N. Koizumi, X. Jiang, J. Kugai, C. Song, Effects of mesoporous silica supports and alkaline promoters on activity of Pd catalysts in CO_2 hydrogenation for methanol synthesis, *Catal. Today*, 194 **(2012)** 16-24.

[117] F. Perez-Alonso, M. Ojeda, T. Herranz, S. Rojas, J. González-Carballo, P. Terreros, J. Fierro, Carbon dioxide hydrogenation over Fe-Ce catalysts, *Catal. Commun*, 9 **(2008)** 1945-1948.

[118] H. Bahruji, M. Bowker, G. Hutchings, N. Dimitratos, P. Wells, E. Gibson, W. Jones, C. Brookes, D. Morgan, G. Lalev, Pd/ZnO catalysts for direct CO_2 hydrogenation to methanol, *J. Catal.*, 343 **(2016)** 133-146.

[119] M. Oschatz, S. Krause, N. Krans, C.H. Mejía, S. Kaskel, K. De Jong, Influence of precursor porosity on sodium and sulfur promoted iron/carbon Fischer-Tropsch catalysts derived from metal-organic frameworks, *Chem. Comm.*, 53 **(2017)** 10204-10207.

CHAPTER 2

Objectives

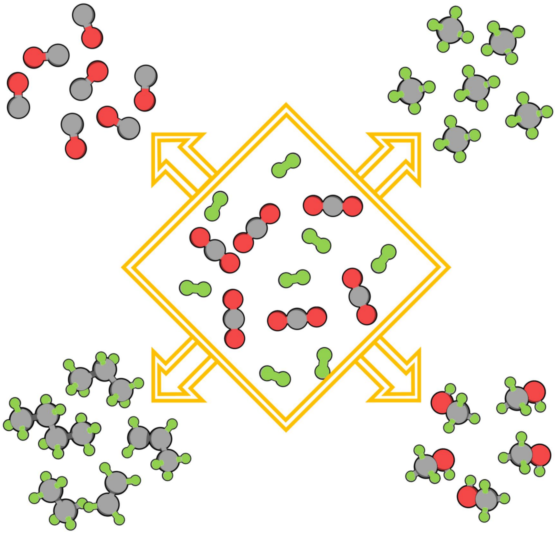

CHAPTER 2

CHAPTER 2

As commented at the end of the Introduction, the present PhD Thesis is mainly focused on the development of transition metal nanoparticles supported on defective N-doped graphenes as highly selective catalysts for CO_2 hydrogenation to obtain value-added carbon-containing chemicals and fuels. The objective of the thesis is to effectively control the selectivity of high-value products by modulating the particle size of metal nanoparticles supported on defective N-doped graphenes, the composition of catalysts and operation conditions, developing a series of catalysts optimized for different CO_2-derived products. More specifically, the objectives corresponding to each Chapter that will be presented are the following:

1) In order to decrease atmospheric CO_2 concentration and cope with the global warming, Co and Co-Fe alloy nanoparticles wrapped on defective N-doped graphenes will be prepared and performed as highly efficient and stable catalysts for Sabatier reaction to obtain methane directly from CO_2.

2) Taking into account the influence of catalysts composition on the catalytic performance, single Co or Fe metals and their alloys in the form of clusters and small nanoparticles supported on defective N-doped graphenes with metal loading of different orders of magnitude will be prepared, characterized and tested regarding their catalytic performance for the reverse-water-gas-shift reaction. It is expected that high dispersion of the metal and metal alloy nanoparticles result in the formation of small clusters on defective N-doped graphenes during high-temperature pyrolysis and this factor should be reflected in their catalytic activity.

3) Considering the particle size effect on the catalytic reaction, a series of Co-Fe alloy nanoparticles supported on defective N-doped graphenes with controlled nanoparticle size distribution will be developed in order to achieve the best selectivity towards C_{2+} hydrocarbons at high conversions. This objective of size-selective catalytic activity is planned to be achieved by controlling the metal nanoparticle size, to find a dimensional window optimization.

4) In order to study the effect of promoters and poison on catalysis, Co-Fe-based catalysts will be prepared by different synthetic routes and then modified with promoters and poison will be presented for CO_2 hydrogenation. The purpose is to study the influence of these additions on the activity and selectivity of CO_2 hydrogenation.

5) In order to meet the huge market demand for methanol, an attempt will be made to prepare Cu and Cu-ZnO nanoparticles supported on defective N-doped graphenes to be used as catalysts for CO_2 conversion to methanol. Considering that Zn is a case of volatile metal, the preparation procedure should avoid the high temperature treatment after the incorporation of Zn in the catalytic system.

In case that the above specific objects are achieved, the present work would contribute to the field of CO_2 conversion by providing a set of highly selective catalysts based on abundant, non-noble metals and the use of natural polysaccharides as graphene precursors for the formation of high-value fuels and chemicals directly from CO_2. The concept behind these catalysts is the ability of the graphene to tune the electron density at the metal nanoparticles and this effect is expected to have a strong influence on the catalytic activity and selectivity for CO_2 hydrogenation. It also expected that the metal-graphene interaction could provide stability to the metal nanoparticles, avoiding particle growing and therefore, produce catalysts with long-term stability under conditions of high temperature, in the presence of H_2 and water occurring during the catalytic reactions. It is known that H_2 and H_2O act as mobilizers of metal atoms and this effect, as well as carbonization, result in a short-term catalyst deactivation and it is expected that this deactivation will not occur in our case due to the interaction with N-doped graphene.

CHAPTER 2

CHAPTER 3

Co-Fe Nanoparticles Wrapped on N-Doped Graphitic Carbons as Highly Efficient CO_2 Methanation Catalysts

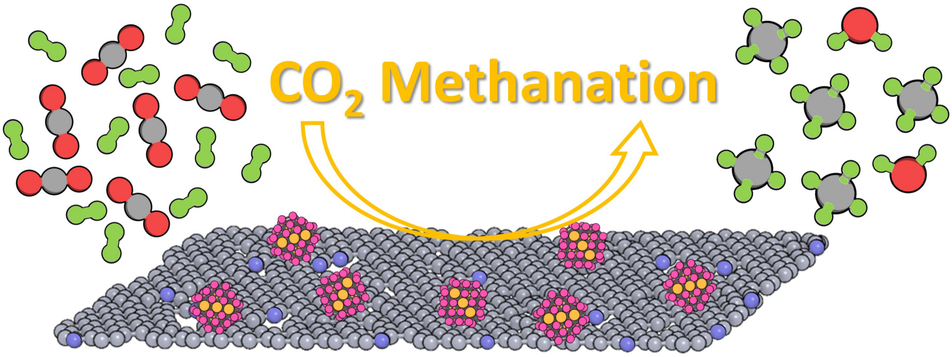

CHAPTER 3

CHAPTER 3

3.1 Introduction

As described in the Introduction, the proposal of the present PhD Thesis is to develop Co-Fe alloy nanoparticles supported on N-doped graphitic carbons, in such a way, that the catalytic activity can be tuned for the selective obtainment of different carbon-containing products directly from CO_2 based on the properties and preparation procedures of these catalysts.

In the present Chapter, Co-Fe alloy NPs wrapped on N-doped graphitic carbons derived from chitosan, exhibiting a remarkable catalytic activity and stability as CO_2 methanation catalysts will be reported. The performance of these Co-Fe alloy NPs wrapped on N-doped graphitic carbon is improved compared with that of similar Co-Fe alloy NPs supported on TiO_2, illustrating the advantage of N-doped graphitic carbon as support.

3.2 Results and Discussion

3.2.1 Samples Preparation and Characterization

As indicated in **Scheme 3.1**, the samples Co-Fe@(N)C under study were prepared by two different procedures. Thus, samples **3.1**-**3.3** (**Scheme 3.1**, **a**) were prepared in the form of quasi-spherical submillimetric beads by co-precipitation with sodium hydroxide of an aqueous chitosan solution acidified by acetic acid containing appropriate amounts of cobalt acetate and iron acetate. Medium and high molecular weight chitosan is soluble in acidic aqueous solutions, but precipitates under neutral or basic conditions. Subsequently, the chitosan spheres containing Co^{2+} and Fe^{2+} salts were dried by a gradual exchange of H_2O by ethanol and a final supercritical CO_2 extraction of ethanol. This procedure has previously been reported as resulting in a highly porous, large surface area chitosan aerogels.[1-3] The final pyrolysis at 900 °C converts the chitosan beads into turbostratic graphitic carbon, accompanied by the simultaneous formation of metallic Co-Fe alloy NPs. Chemical reduction of Co^{2+} and Fe^{2+} ions occurs during the pyrolysis simultaneously with chitosan graphitization due to the reductive conditions of the process derived from the absence of oxygen.[4-6]

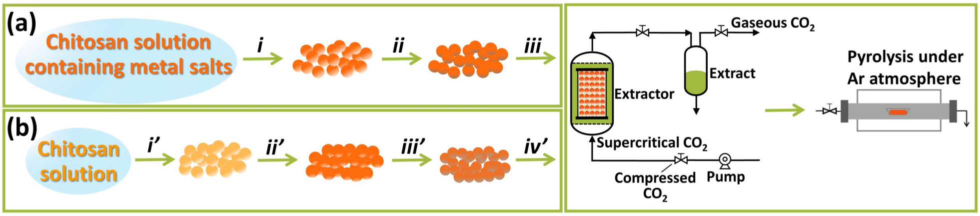

Scheme 3.1. Illustration of preparation procedures. (**a**) Samples **3.1**-**3.3** underwent *i*) precipitation in NaOH; *ii*) water/ethanol exchange and reduction in $NaBH_4$ ethanol solution; *iii*) supercritical CO_2 drying. (**b**) Samples **3.4**-**3.5** underwent *i'*) precipitation in NaOH; *ii'*) water/ethanol exchange and metal salt impregnation; *iii'*) reduction in $NaBH_4$ ethanol solution; *iv'*) supercritical CO_2 drying.

In an alternative procedure also indicated in **Scheme 3.1**, **b**, Co-Fe@(N)C samples **3.4** and **3.5** were prepared through first formation of the chitosan beads by NaOH precipitation of acidic aqueous chitosan solution, then, exchange H_2O by ethanol before impregnation of $Co(OAc)_2$ and $Fe(OAc)_2$ from the ethanol solution. Subsequently, Co^{2+} and Fe^{2+} were reduced by sodium borohydride in ethanol before the final pyrolysis. For the sake of comparison, one additional sample using TiO_2 as a support was also prepared by wet impregnation of TiO_2 with an aqueous solution of $Co(OAc)_2$ and $Fe(OAc)_2$, followed by drying and H_2 reduction of the resulting powder at 600 °C.

The list of samples, their most important analytical data and the average particle size of Co-Fe NPs are collected in **Table 3.1**, while **Table 8.1.1** in **CHAPTER 8** indicates the exact amounts of chitosan, $Co(OAc)_2$, and $Fe(OAc)_2$ used in the preparation of each of the five Co-Fe@(N)C samples. As it can be seen in **Table 3.1**, sample **3.1** contains only Co, while the other samples **3.2**-**3.5** contain a similar Fe content between 4.3 to 5.0 wt.%, varying in the Co content from 12.0 to 17.5 wt.%. Of note is that the exact metal content of samples **3.1**-**3.5** is difficult to predict beforehand in the adsorption step due to high weight loss (over 80 %) resulting in the pyrolysis converting moist chitosan into the N-doped graphitic carbon. Importantly, samples **3.1**-**3.5** contain a residual weight percentage of N from the original chitosan composition that ranges from 0.31 to 1.48 wt.% (see **Table 3.1**). In previous studies, it has been found that the N content of graphitic carbon derived from chitosan can vary from 6.5 wt.% to a negligible value depending on the pyrolysis conditions and the presence of metals that can promote graphitization.[7, 8]

Table 3.1. Analytical data and average Co-Fe particle size for the samples under study.

Sample No.	Co (wt.%)[a]	Fe (wt.%)[a]	Total Co+Fe content (wt.%)[a]	C (wt.%)[b]	N (wt.%)[b]	Average particle size (nm)[c]
3.1	4.9	-	4.9	85.85	1.48	9.5±2
3.2	12.0	5.0	17.0	76.80	1.21	6.9±2
3.3	13.6	5.2	18.8	72.36	0.31	9.7±5
3.4	13.1	4.6	17.7	64.37	0.75	13.3±4
3.5	17.5	4.3	21.8	63.91	1.05	11.2±3

[a] Determined by ICP-OES analysis after dissolving the metals in *aqua regia*; [b] It is assumed that the rest to 100 % is residual oxygen; [c] Determined by the high-resolution transmission electron microscopy in dark field (DF-HRTEM).

X-ray diffraction patterns of samples **3.1**-**3.5** show that they are constituted by metallic Co and Fe, mainly in the fcc (sample **3.1**) or bcc phase, accompanied by less intense peaks of the fcc (samples **3.2**-**3.5**). No other peaks attributable to metal oxides were recorded in these patterns, indicating that, as expected, Co^{2+} and Fe^{2+} ions have become reduced to metallic state during the pyrolysis process. Previous studies have widely documented that pyrolysis of carbon precursors results in the chemical reduction of transition metals,[5, 9-13] including Fe.[11] To determine if the Co and Fe elements present in the samples are independent Co and Fe particles or they are alloyed, experimental XRD data were analyzed by Rietveld refinement.

As an example, **Figure 3.1** shows the fitting of the Rietveld analysis and the experimental data. However, although this XRD analysis supports the formation of Co-Fe alloy,[14-16] the similarity between the cell parameters of metallic Co and Fe makes necessary additional confirmation by transmission electron microscopy to address this issue.

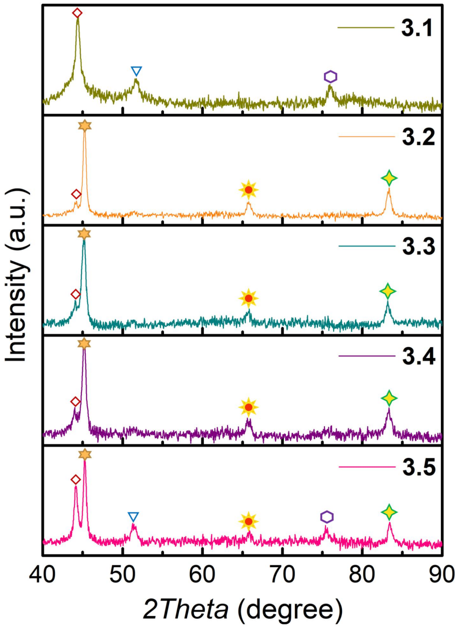

Figure 3.1. XRD data and the best Rietveld refinement for samples **3.1**-**3.5**. Symbols: Co (111) fcc (◇); Co (200) fcc (▽); Co (220) fcc (⬡); Co(0.7)Fe(0.3)(110)bcc (✶); Co(0.7)Fe(0.3)(200)bcc (✹); Co(0.7)Fe(0.3)(211)bcc (✦)

Transformation of chitosan into N-doped graphitic carbon was assessed by Raman spectroscopy. In Raman spectroscopy, graphene and graphitic carbons present three characteristic vibration bands at wavenumbers between 3000 and 2600, 1590 and 1350 cm^{-1} corresponding to overtones, G and D bands. **Figure 3.2** shows representative Raman spectra for the Co-Fe@(N)C samples under study. The width of the G and D peaks and their relative intensity (I_G/I_D) are taken as quantitative indicators of the quality of the graphene layers.[3, 17, 18] In the present case, the G and D peaks are notably narrower than those previously reported in the pyrolysis of chitosan at 900 °C, probably reflecting the influence of Co-Fe NPs promoting a better graphitization of the N-doped graphitic carbon residue. This proposal would be in agreement with the previously commented lower than expected N content of the samples indicated in **Table 3.1**. In addition, particularly for samples **3.1**-**3.3**, the Raman spectra show a narrow 2D peak in the high-frequency region at about 2700 cm^{-1}. Observation of narrow 2D peaks is associated generally with the presence of few layers of graphene stacking since this 2D peak becomes broader and eventually disappears as the number of stacked graphene layers increases.[17-19] Thus, Raman spectra indicate that the carbon residue, particularly in samples **3.1**-**3.3** is constituted by the stacking of a few N-doped defective graphene layers.

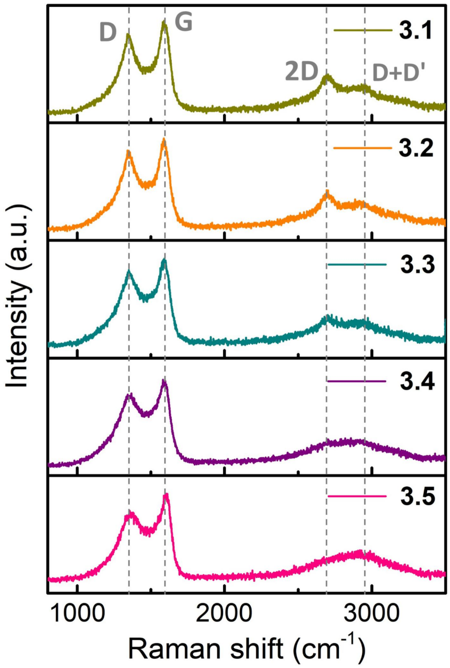

Figure 3.2. Raman spectrum of the samples **3.1**-**3.5** recorded upon 514 nm laser excitation.

The morphology of the materials was determined by field emission scanning electron microscopy. It seems that the known morphology of chitosan aerogels constituted by the agglomeration of cotton-like, fluffy fibrils are mostly preserved in the pyrolysis during the transformation of chitosan into N-doped graphitic carbon residue. **Figure 3.3** shows representative FESEM images of the samples under study in which the loose, coral-shaped, spongy morphology of the samples with considerable macroporosity can be observed. The presence of MNPs could not be visualized by FESEM, meaning that these metal NPs should be smaller enough to not become visualized at the 100 nm scale of the technique.

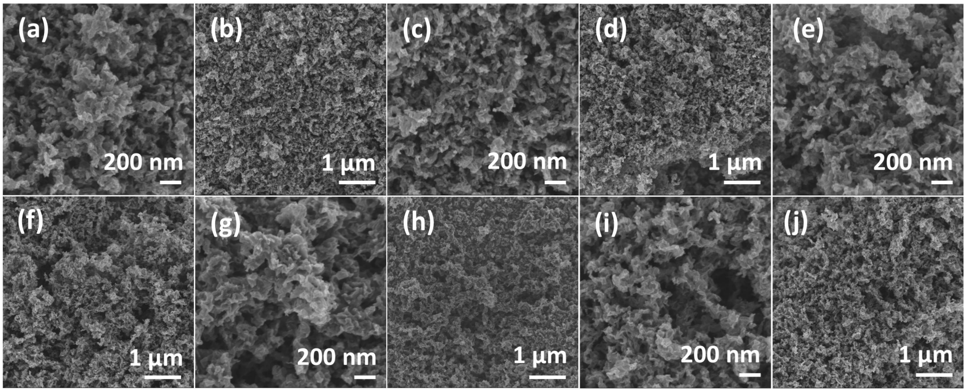

Figure 3.3. FESEM images of samples **3.1**-**3.5**. (**a**, **b**: sample **3.1**; **c**, **d**: sample **3.2**; **e**, **f:** sample **3.3**; **g**, **h**: sample **3.4** and **i**, **j**: sample **3.5**.)

The presence of nanometric Co-Fe NPs supported on graphene layers of a few micrometers dimensions could be clearly detected in high-resolution transmission electron microscopy images of the samples after ultrasound dispersion of the black carbon powders, both in bright and dark fields. **Figure 3.4** shows selected images of the samples under study. The particle size distribution and the average size was determined by measuring a statistically significant number of metal NPs. These values are collected in **Table 3.1**, while the corresponding histograms are inserted in the HRTEM images. Average Co-Fe particle size between 6.9 and 13.3 nm with somewhat broad size distribution were estimated from these images. From the high-resolution images, measurement of a fringe distance of 0.22 nm corresponding to the 110 distance of the bcc phase indicates that the Co-Fe NPs correspond to a random alloy since these values are between those corresponding to independent Co and Fe bcc phases.

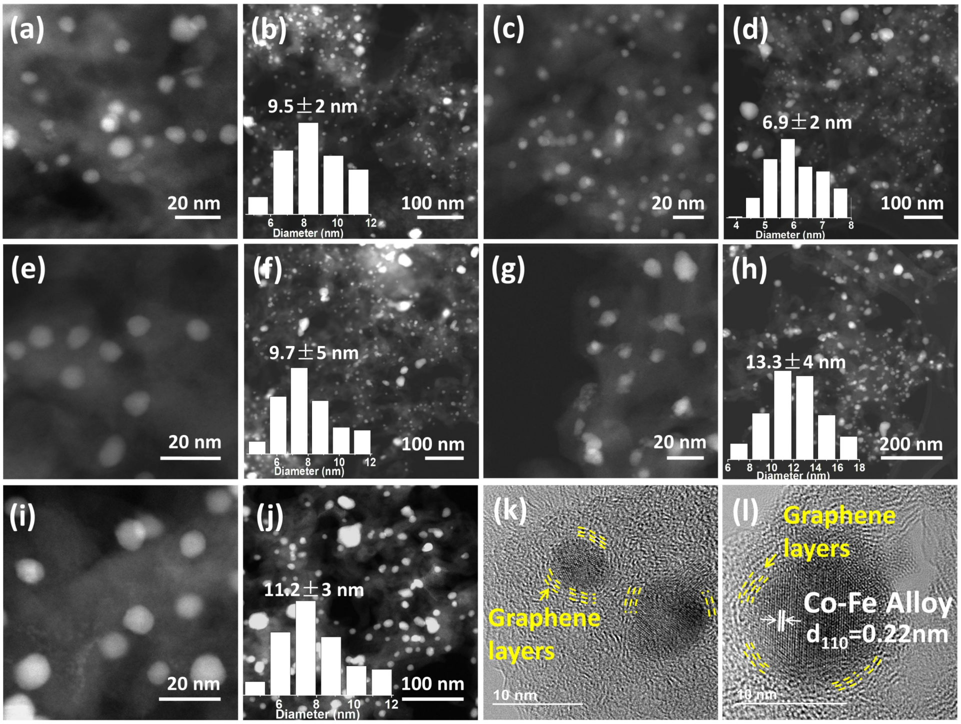

Figure 3.4. DF-TEM images of samples **3.1**-**3.5** and HRTEM images of samples **3.4**. (**a**, **b**: sample **3.1**; **c**, **d**: sample **3.2**; **e**, **f**: sample **3.3**; **g**, **h**, **k**, **l**: sample **3.4** and **i**, **j**: sample **3.5**. Inset: statistical particle size distributions of samples **3.1**-**3.5** according to the main frame image.)

High-resolution TEM images in bright field also revealed that Co-Fe NPs are wrapped by a few (three and four) layers of N-doped graphene characterized by its typical 0.34 nm interplanar distance. It appears that this wrapping is not complete, but covers partially the surface of the Co-Fe NP. To illustrate this important point that can serve to understand the role of N-doped graphitic carbon on the catalytic activity, (**Figure 3.4**, **k**, **l**) has marked a representative case. As commented in the Introduction, theoretical calculations on models have suggested that graphene can donate charge density to the Co-Fe NP and this charge transfer enriching the electron density at certain atoms of the MNPs in contact with graphene basal plane can act as catalytic sites exhibiting stronger CO_2 binding.

3.2.2 Catalytic Activity

The catalytic activity of samples **3.1**-**3.5** for CO_2 methanation was performed in a pressurized fixed-bed, stainless steel reactor in the range of temperatures from 300 to 500 ^oC. Each catalyst was submitted to catalytic tests in which the reactor temperature is increased in 50 ^oC increments with a dwell time of 1 h. The activity data at each temperature was the average of three analysis of the reaction mixture performed at 30, 45 and 55 min. For all data, the variation among the three analyses was less than 5 %. Preliminary controls at 500 ^oC in the absence of any catalyst or using (N)C without any metal as catalyst showed a CO_2 conversion of 6 and 12.9 %, respectively, methane being the main product with a selectivity over 95 %. Previous reports in the literature have shown that N-doped graphene can act as a methanation catalyst,[20] although the activity measured under our conditions was much lower than that measured for the Co-Fe@(N)C samples.

All samples Co-Fe@(N)C exhibit a remarkable catalytic activity for CO_2 hydrogenation. The main product was CH_4, accompanied by a less percentage of CO. The formation of minute, but detectable, amounts of C_{2+} products constituted by ethane, propane, butane, ethylene and propylene were also observed. Thermodynamic calculations on CO and CO_2 hydrogenation, validated in the case of CO, indicate that under the present reaction conditions the equilibrium should be reached at very high CO_2 conversion with 100 % selectivity to CH_4 up to temperatures of 500 °C. Therefore, although in some cases close to the equilibrium, the data achieved in the present study are not limited by equilibrium considerations. As a general trend of all the samples, CO_2 conversion and CH_4 selectivity increase with the temperature, the highest values in the temperature range under study being measured at 500 °C. **Figure 3.5** summarizes the results obtained for the Co-Fe@(N)C samples under study at 500 °C, while **Figure 3.6** and **Tables 8.4.1.1** to **8.4.1.5** (in **CHAPTER 8**) gather the full set of data for all the catalytic study.

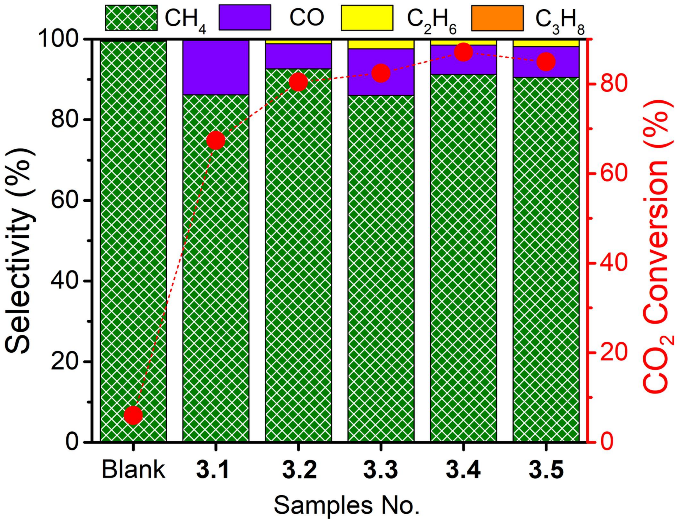

Figure 3.5. CO_2 methanation activity for samples **3.1**-**3.5** at 500 °C under the same conditions. Reaction conditions: H_2/CO_2 ratio of 7, total flow 4 mL/min, 10 bar, 40 mg catalyst.

As it can be seen in **Figure 3.5**, CO_2 conversion and CH_4 selectivity varied also depending on the sample composition. It was observed that sample **3.1** containing less total metal loading reaches lower CO_2 conversions and exhibits higher unwanted CO percentages, compared to the rest of the samples that contain Co-Fe alloy. On the other hand, the catalytic activity of sample **3.5** that contained a somewhat higher total metal percentage was lower than for samples **3.2**-**3.4**. Worth noting is the observation of a high percentage of about 20 % of C_{2+} products for samples **3.3** and **3.4** at 400 °C for CO_2 conversion above 60 %. Formation of C_{2+} products in high selectivity will be the subject of **CHAPTER 5**.

It was determined that the best performing catalyst was sample **3.4** that reached 87 % CO_2 conversion with a CH_4 selectivity of 91 % operating at 500 °C and a space velocity of 75 h^{-1} at 10 bar. The better performance of sample **3.4** is observed in spite of the notably larger particle size (13.3 nm) compared particularly with sample **3.2** that has a similar composition, but smaller particle size (6.9 nm). This different behavior between samples **3.2** and **3.4** is most probably due to the different preparation procedures. When the different total metal content of the samples is taken into account and turnover frequencies are considered as the figure of merit of the catalytic performance, sample **3.1** is the best performing due to its low metal content (TOF 25.7 s^{-1}), while the other samples have similar TOF values ranging from 8.7 s^{-1} for sample **3.4**, 8.5 s^{-1} for sample **3.2**, 7.9 s^{-1} for sample **3**, and 7.0 s^{-1} for sample **3.5**. A plausible reaction mechanism based on the literature for the catalytic CO_2 methanation on Co-Fe@(N)C is provided in **Scheme 3.2**.

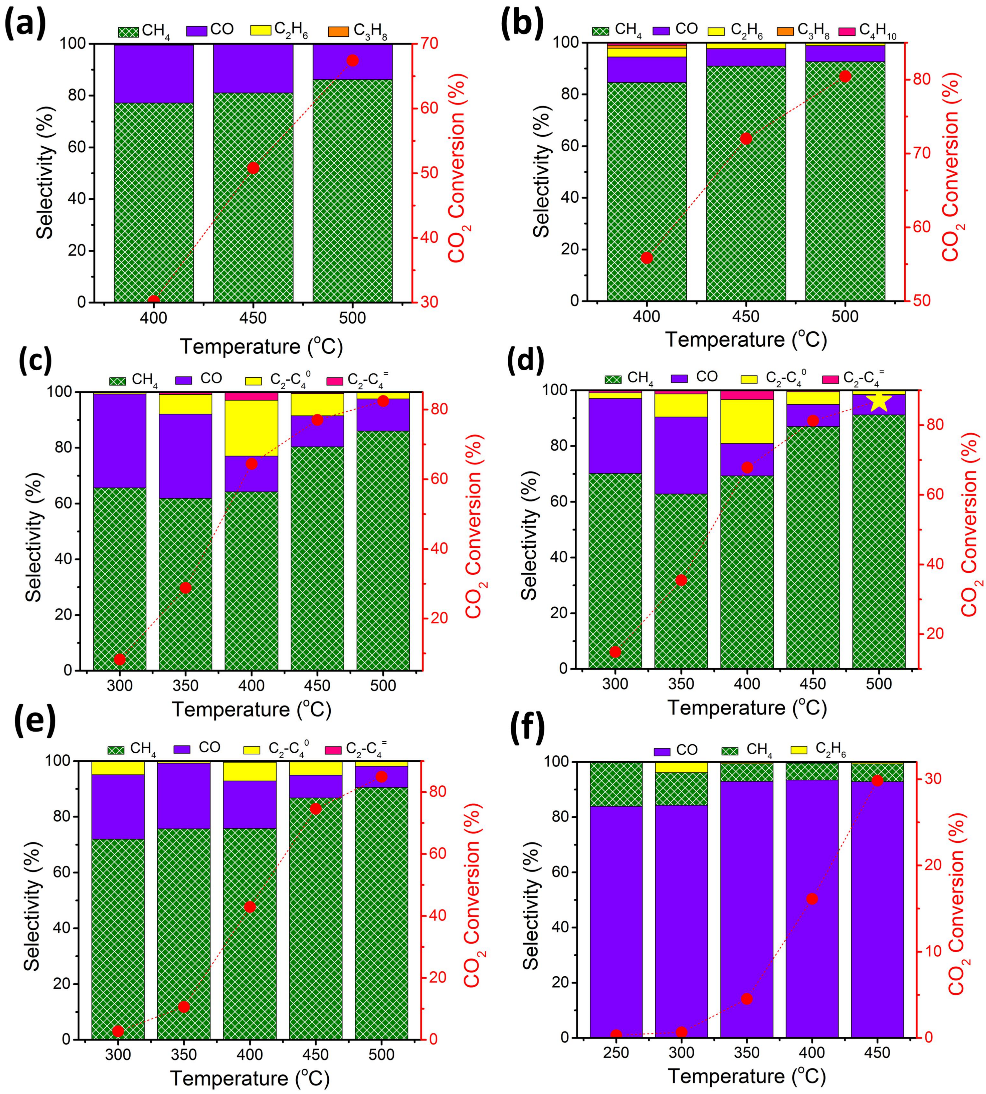

Figure 3.6. CO$_2$ methanation activity of samples **3.1**-**3.5** and Co-Fe/TiO$_2$ at different temperature. (**a**, **b**, **c**, **d**, **e**, **f** corresponding to sample **3.1**-**3.5** and Co-Fe/TiO$_2$, respectively.) Reaction conditions: H$_2$/CO$_2$ ratio of 7, total flow 4 mL/min, 10 bar, 40 mg catalyst.

Associative: Hydrogen atoms being incorporated to adsorb CO_2.

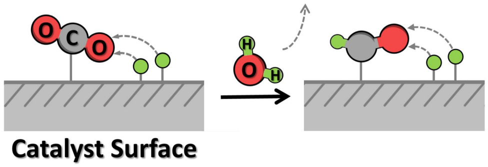

Dissociative: Oxygen being split from CO_2 before H attack.

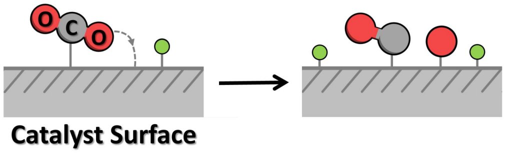

Scheme 3.2. Possible alternative pathways leading to methanation.

Stability of sample **3.4** was assessed by performing a long run 30 h experiment at 500 °C, observing a constant CO_2 conversion and product distribution. After a 30 h reaction at 500 °C, the sample was screened again for its catalytic activity at each temperature between 300 and 500 °C, observing a consistent reproducibility in CO_2 conversion values and product distribution.

3.2.3 Influence of the Support

The influence of N-doped graphitic carbon as the support of Co-Fe alloy NPs was assessed by comparing the activity data of samples **3.1**-**3.5** with that of Co-Fe alloy NPs supported on TiO_2. The results are also presented in **Figure 3.6**. In this case, the main product under the same reaction conditions was CO with a selectivity of 92.8 % at a CO_2 conversion of 29.8 % measured at 450 °C. **Table 8.4.1.6** in **CHAPTER**

8 contains the full catalytic data for Co-Fe/TiO_2 as a function of the reaction temperature.

3.3 Conclusions

The present Chapter discloses two different preparation procedures of Co-Fe alloy NPs wrapped on N-doped graphitic carbon, in which the metal NPs are partially wrapped by two to four graphene layers that exhibit remarkable catalytic activities for the CO_2 methanation. The selectivity of CH_4 formation is over 90 % at high CO_2 conversion values over 85 %. This catalytic activity contrasts with that of similar Co-Fe alloy NPs supported on TiO_2, for which CO is the main product. Catalysts Co-Fe@(N)C **3.1**-**3.5** appear to be stable for long-time runs.

Overall, the present Chapter shows the potential of chitosan to form metal NPs wrapped on N-doped graphitic carbon as efficient catalysts for the CO_2 methanation with remarkable activity and stability. As it will show in the subsequent Chapters, the performance of these Co-Fe alloy NPs wrapped on N-doped graphitic carbon can be further turned to selectively promote the reverse water-gas shift reaction or CO_2 hydrogenation to obtain value-added C_2-C_4 hydrocarbons by controlling in a narrow window particle size of Co-Fe nanoparticles.

References

[1] A. El Kadib, M. Bousmina, Chitosan bio-based organic-inorganic hybrid aerogel microspheres, *Chem. Eur. J.*, 18 **(2012)** 8264-8277.

[2] R. Valentin, K. Molvinger, F. Quignard, D. Brunel, Supercritical CO_2 dried chitosan: an efficient intrinsic heterogeneous catalyst in fine chemistry, *New J. Chem.*, 27 **(2003)** 1690-1692.

[3] A. Primo, P. Atienzar, E. Sanchez, J.M. Delgado, H. García, From biomass wastes to large-area, high-quality, N-doped graphene: catalyst-free carbonization of chitosan coatings on arbitrary substrates, *Chem. Comm.*, 48 **(2012)** 9254-9256.

[4] G. Abellan, M. Latorre-Sanchez, V. Fornes, A. Ribera, H. García, Graphene as a carbon source effects the nanometallurgy of nickel in Ni, Mn layered double hydroxide-graphene oxide composites, *Chem. Comm.*, 48 **(2012)** 11416-11418.

[5] M. Latorre-Sanchez, P. Atienzar, G. Abellan, M. Puche, V. Fornés, A. Ribera, H. García, The synthesis of a hybrid graphene-nickel/manganese mixed oxide and its performance in lithium-ion batteries, *Carbon*, 50 **(2012)** 518-525.

[6] A. Primo, E. Sánchez, J.M. Delgado, H. García, High-yield production of N-doped graphitic platelets by aqueous exfoliation of pyrolyzed chitosan, *Carbon*, 68 **(2014)** 777-783.

[7] D. Mateo, I. Esteve-Adell, J. Albero, J.F.S. Royo, A. Primo, H. Garcia, 111 oriented gold nanoplatelets on multilayer graphene as visible light photocatalyst for overall water splitting, *Nat. Commun.*, 7 **(2016)** 1-8.

[8] J. He, A. Anouar, A. Primo, H. García, Quality Improvement of few-layers defective graphene from biomass and application for H_2 generation, *Nanomater.*, 9 **(2019)** 895.

[9] G. Abellán, M. Latorre-Sánchez, V. Fornés, A. Ribera, H. García, Graphene as a carbon source effects the nanometallurgy of nickel in Ni, Mn layered double hydroxide–graphene oxide composites, *Chem. Comm.*, 48 **(2012)** 11416-11418.

[10] A. Primo, I. Esteve-Adell, J.F. Blandez, A. Dhakshinamoorthy, M. Álvaro, N. Candu, S.M. Coman, V.I. Parvulescu, H. García, High catalytic activity of oriented 2.0.0 Copper (I) oxide grown on graphene film, *Nat. Commun.*, 6 **(2015)** 1-11.

[11] J. He, A. Dhakshinamoorthy, A.M. Primo Arnau, H. García Gómez, Iron nanoparticles embedded in graphitic carbon matrix as heterogeneous catalysts for the oxidative CN coupling of aromatic NH compounds and amides, *ChemCatChem*, 9 **(2017)** 3003-3012.

[12] D. Mateo, J. Albero, H. Garcia, Graphene supported NiO/Ni nanoparticles as efficient photocatalyst for gas phase CO_2 reduction with hydrogen, *Appl. Catal. B*, 224 **(2018)** 563-571.

[13] Z. Ma, C. Tsounis, P.V. Kumar, Z. Han, R.J. Wong, C.Y. Toe, S. Zhou, N.M. Bedford, L. Thomsen, Y.H. Ng, Enhanced electrochemical CO_2 reduction of Cu@CuxO nanoparticles decorated on 3D vertical graphene with intrinsic sp^3-type defect, *Adv. Funct. Mater.*, 30 **(2020)** 1910118.

[14] S.L. Zhang, B.Y. Guan, X.W. Lou, Co-Fe alloy/N-doped carbon hollow spheres derived from dual metal-organic frameworks for enhanced electrocatalytic oxygen reduction, *Small*, 15 **(2019)** 1805324.

[15] G. Chen, R. Gao, Y. Zhao, Z. Li, G.I. Waterhouse, R. Shi, J. Zhao, M. Zhang, L. Shang, G. Sheng, Alumina-supported CoFe alloy catalysts derived from layered-double-hydroxide nanosheets for efficient photothermal CO_2 hydrogenation to hydrocarbons, *Adv. Mater.*, 30 **(2018)** 1704663.

[16] T. Numpilai, T. Witoon, N. Chanlek, W. Limphirat, G. Bonura, M. Chareonpanich, J. Limtrakul, Structure-activity relationships of Fe-Co/K-Al_2O_3 catalysts calcined at different temperatures for CO_2 hydrogenation to light olefins, *Appl. Catal. A*, 547 **(2017)** 219-229.

[17] A. Eckmann, A. Felten, A. Mishchenko, L. Britnell, R. Krupke, K.S. Novoselov, C. Casiraghi, Probing the nature of defects in graphene by Raman spectroscopy, *Nano*

letters, 12 **(2012)** 3925-3930.

[18] J. Hong, M.K. Park, E.J. Lee, D. Lee, D.S. Hwang, S. Ryu, Origin of new broad Raman D and G peaks in annealed graphene, *Sci. Rep.*, 3 **(2013)** 1-5.

[19] O. Frank, M. Mohr, J. Maultzsch, C. Thomsen, I. Riaz, R. Jalil, K.S. Novoselov, G. Tsoukleri, J. Parthenios, K. Papagelis, Raman 2D-band splitting in graphene: theory and experiment, *ACS nano*, 5 **(2011)** 2231-2239.

[20] B. Jurca, C. Bucur, A. Primo, P. Concepción, V.I. Parvulescu, H. García Gómez, N-doped defective graphene from biomass as catalyst for CO_2 hydrogenation to methane, *ChemCatChem*, 11 **(2018)** 985-990.

CHAPTER 4

Co-Fe Clusters Supported on N-Doped Graphitic Carbon as Highly Selective Catalysts for Reverse Water-Gas Shift Reaction

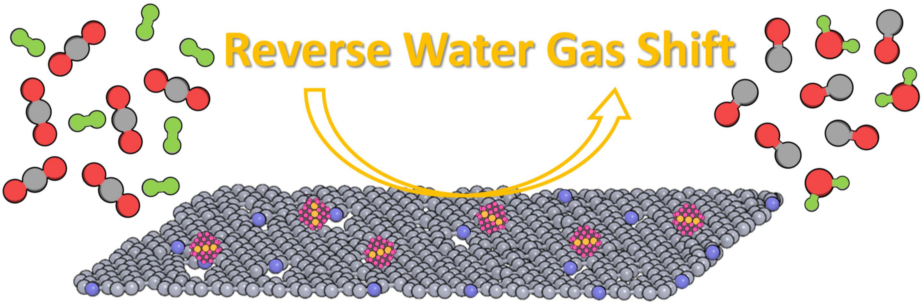

CHAPTER 4

CHAPTER 4

4.1 Introduction

Continuing with the target of the present PhD Thesis, that is aimed at the development of Co-Fe-based catalysts supported on N-doped graphitic carbons as highly selective catalysts for CO_2 hydrogenation, the present Chapter deals with the catalytic performance of Co-Fe alloy clusters and small nanoparticles of single Co, Fe metals and their alloys. The catalytic data show that Co-Fe alloy clusters supported on N-doped graphitic carbons exhibit a remarkable reverse water-gas shift selectivity and significantly higher activity values than that of analogous catalysts with metal NPs of size ranging from 1 to 5 nm. The catalytic behavior of these Co-Fe alloy CLs supported on N-doped graphitic carbons contrasts with the performance of an analogous catalyst using SiO_2 as the support or catalysts with Co-Fe alloy NPs of larger size commented in **CHAPTER 3**, on which a notably different selectivity towards methane is observed.

4.2 Results and Discussion

4.2.1 Samples preparation and characterization

The catalysts under study were prepared by impregnation of millimetric hydrogel chitosan beads with $Co(OAc)_2$, $Fe(OAc)_2$ or appropriate $Co(OAc)_2$ and $Fe(OAc)_2$ mixtures dissolved in 1:1 water/ethanol, followed by ethanol exchange, the supercritical CO_2 drying of the metal-containing alcogel microspheres and a final pyrolysis. **Scheme 4.1** illustrates the preparation procedure for samples **4.1**-**4.10**.

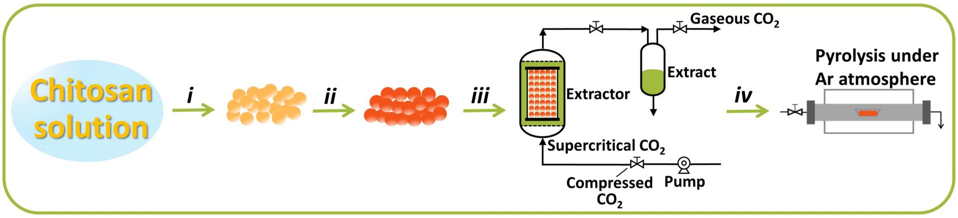

Scheme 4.1 Simplified process used to prepare the Co-Fe@(N)C samples under study. *i*) Precipitation in NaOH solution; *ii*) water/ethanol exchange, metal salt impregnation and ethanol exchange; *iii*) supercritical CO_2 drying; *iv*) pyrolysis in Ar.

As shown in the previous Chapter, the process starts with the precipitation as microspheres of chitosan dissolved in acidic aqueous solution by neutralization with NaOH. One property of chitosan and related polysaccharides is their ability to adsorb metal salts from aqueous solution, due to strong hydrogen bond interactions.[1-2] This adsorption capacity has been used advantageously to co-incorporate Fe and Co salts on chitosan. The resulting hydrogels containing Co or Fe salts or their mixtures were converted to alcogels by dispersing consecutively the beads in water-ethanol solutions of increased ethanol content up to absolute ethanol. The alcogel microspheres containing Co^{2+} or Fe^{2+} ions were finally dried in supercritical CO_2. It is well documented in the literature that this procedure renders highly porous chitosan aerogels with a large surface area.[3-6] Subsequent pyrolysis of chitosan beads have been reported to form graphitic carbon residues that can be exfoliated easily by sonication into the defective N-doped graphene. [5, 7] It is worth noting that chitosan as a glucosamine polymer is simultaneously the source of C and

N, resulting in the pyrolysis of N-doped defective graphene with a N content about 5 wt.%. According to the analyses of X-ray photoelectron spectroscopy (see **Figure 4.3**, **g-i**), the two main types of N atoms present in N-doped defective graphene are pyridinic (binding energy: 398.2 eV, sp^2 N atoms at the periphery bonded to two C atoms and giving one electron to the π cloud) and graphitic (binding energy: 400.7 eV, sp^2 N atoms bonded to three C atoms and giving one electron to the π cloud) in a proportion ~ 47:53.[5, 8] If the chitosan beads contain adsorbed transition metals, they are typically converted into metal NPs during the pyrolysis at 900 ^oC or higher temperature due to the reductive conditions of the process. The term carbochemical reduction has been previously coined to denote the formation of metal NPs or metal alloy NPs upon heating their salts at high temperatures in the presence of materials generating carbon residues.[7, 9, 10]

Three Co-Fe alloy samples with increasing Co content were prepared. The total metal content of these three samples is low, below 0.2 wt.%. To determine the role of metal loading and particle size on the performance of the catalyst, three more Co-Fe alloy samples were obtained following an identical procedure, but using a higher salt concentration in the range of about 10 wt.%. Single Fe or Co metals supported on N-doped graphitic carbons were also synthesized for comparison. The set of catalysts includes an additional sample using SiO_2 as a support. **Table 4.1** lists the codes and relevant analytical data of the samples under study.

Table 4.1. List of samples under study and their main analytical and physicochemical parameters.

Sample No.	Co (wt.%)[a]	Fe (wt.%)[a]	Total Co+Fe content (wt.%)[a]	Fe/Co ratio	C (wt.%)[b]	N (wt.%)[b]	Average particle size (nm)[c]
4.1	0.042	0.053	0.042	1.26	75.84	5.84	<1 nm (CLs)
4.2	0.081	0.052	0.081	0.64	75.80	5.65	<1 nm (CLs)
4.3	0.120	0.053	0.120	0.44	78.53	5.06	<1 nm (CLs)
4.4	0.049	-	0.049	-	73.25	5.07	<1 nm (CLs)
4.5	-	0.054	0.054	-	76.35	5.47	<1 nm (CLs)
4.6	5.21	10.32	5.21	1.98	56.85	3.38	4.8±0.7 (NPs)
4.7	5.07	6.65	5.07	1.31	62.45	4.00	3.8±0.7 (NPs)
4.8	4.09	2.55	4.09	0.62	69.13	3.56	2.6±0.7 (NPs)
4.9	6.10	-	6.10	-	76.34	3.03	1.0±0.3 (NPs)
4.10	-	7.89	7.89	-	77.35	3.10	1.4±0.3 (NPs)
4.11[d]	11.38	3.92	11.38	0.34	38.40	-	7.0±2.6 (NPs)
4.12[e]	9.97	4.79	9.97	0.48	-	-	-

[a] Determined by ICP-OES analysis after dissolving the metals in *aqua regia*; [b] It is assumed that the rest to 100 % is residual oxygen; [c] Determined by DF-TEM; [d] Graphitic carbon from pyrolysis of alginic acid as support; [e] SiO_2 as support.

The metal content was determined by ICP-OES elemental analysis after dissolving the metals in *aqua regia*. Co and Fe content values are summarized in **Table 4.1**. As it can be seen there, elemental analysis for samples **4.1**-**4.3** showed similar Fe content, but increasing Co loadings, agreeing with the preparation procedure of these samples in which higher amounts of Co were added from samples **4.1** to **4.3**. The total Co-Fe content of these three samples **4.1**-**4.3** was very low, varying from about 0.10 to 0.17 wt.%, this being one of the main differences with respect to samples **3.1**-**3.5**. Two additional samples having only either Co (sample **4.4**) or Fe (sample **4.5**) at low loadings were also prepared. As expected, in view of the higher salt concentrations used, the Co and Fe content in samples **4.6** to **4.8** were about two orders of magnitude higher than in samples **4.1**-**4.5** and in the same range as those of single Co or Fe metal (samples **4.9** and **4.10**), the sample using undoped graphitic carbon **4.11** or that of the control sample **4.12** in which the Co-Fe alloy NPs were supported on SiO_2.

The Fe and Co contents of samples samples **4.1**-**4.5** were too low and their dispersion too high to detect peaks of these metals in powder X-ray diffraction. In contrast samples **4.6** to **4.12** exhibit in XRD the patterns characteristic of fcc phase for Co and bcc phase for Fe and Co-Fe alloy, confirming the presence of metallic Co-Fe NPs and the occurrence of carbochemical reduction during the pyrolysis. For samples **4.6**-**4.8**, **4.11** and **4.12** containing mixtures of Fe and Co, the minor variations in the position of the diffraction peak at $2\theta \approx 44^o$ suggest that the metal NPs are real Co-Fe alloys, rather than independent Fe and Co NPs, although the very similar cell parameters of Co and Fe make this conclusion somewhat uncertain. **Figure 4.1** presents the XRD patterns of samples **4.6**-**4.8**, **4.11** and **4.12** having bcc cubic phase, where the peaks appearing at 44.9^o (110) and 65.5^o (200) are assigned to Co-Fe alloy. In comparison, the sample **4.9** exhibits a Co fcc cubic (Fm3m) structure, showing characteristic diffraction peaks at 2θ = 44.3° (111), 51.6° (200) and 75.9° (220).[11, 12] In any case, XRD data for samples **4.6** to **4.12** conclusively rule out the presence of detectable amount of metal oxides or the formationof the detectable amounts of metal carbides during pyrolysis.

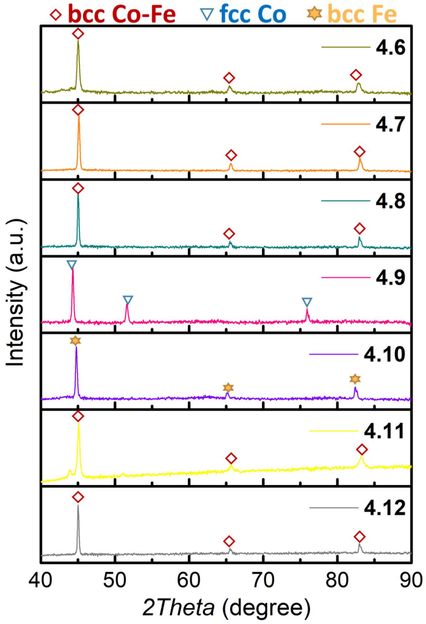

Figure 4.1. XRD patterns of the samples **4.6**-**4.12**.

The elemental composition and chemical environments of Co-Fe@(N)G, Co@(N)G, and Fe@(N)G are examined by X-ray photoelectron spectroscopy (XPS). **Figure 4.2**, **a**, **b** exhibits the Co 2p and Fe 2p spectra of sample **4.1**. The high-resolution XPS spectrum of Co $2p_{3/2}$ in **Figure 4.2**, **a** exhibits distinct peaks at 778.3, 780.5, and 786.6 eV, ascribable to zero-valence cobalt, the oxidation state of Co(II), and the satellite peak, respectively. In accordance, the peak corresponding to Co $2p_{1/2}$ can also be deconvoluted with three components, corresponding to metallic Co, Co^{2+}, and the satellite peak, respectively. Analogously, the deconvolution of the Fe 2p peak in **Figure 4.2**, **b** shows the peaks corresponding to metallic Fe (707.4 eV for Fe $2p_{3/2}$ and 721.0 eV for Fe $2p_{1/2}$), Fe^{2+} (709.2 eV for Fe $2p_{3/2}$ and 722.8 eV for Fe $2p_{1/2}$), Fe^{3+} (710.9 eV for Fe $2p_{3/2}$ and 724.5 eV for Fe $2p_{1/2}$), and satellite peaks (714.5 eV for Fe $2p_{3/2}$ and 728.1 eV for Fe $2p_{1/2}$). The ratio of metallic Co/Co species in sample **4.1** was about 46.7%, and the ratio of metallic Fe/ total Fe was even less than 26.4%. This could be attributed to the high susceptibility of the small Co-Fe clusters to air and surface oxidization, making the surface metallic atoms mainly exist in the form of high-valent states, and the low permeability of the X-ray, making the zero-valent Co and Fe in the bulk of Co-Fe clusters less detectable by XPS. The Fe/Co atomic ratio for sample **4.1** according to XPS is 1.3, which is in good accordance with the value determined by ICP-OES analysis. Similarly, the high-resolution Co $2p_{3/2}$ XPS spectrum of sample **4.4** in **Figure 4.2**, **c** exhibits distinct peaks at 778.3, 780.5, and 786.5 eV, ascribable to metallic Co, Co^{2+}, and the satellite peak, respectively. The high-resolution Fe $2p_{3/2}$ XPS spectrum of sample **4.5** in **Figure 4.2**, **d** exhibits distinct peaks at 707.0, 709.3, 711.8, and 713.5 eV, corresponding to metallic Fe, the oxidation states of Fe(II) and Fe(III), and the satellite peak, respectively. The ratios of zero-valence metal/metal species in samples **4.4** and **4.5** were 43.8 and 25.3%, respectively.

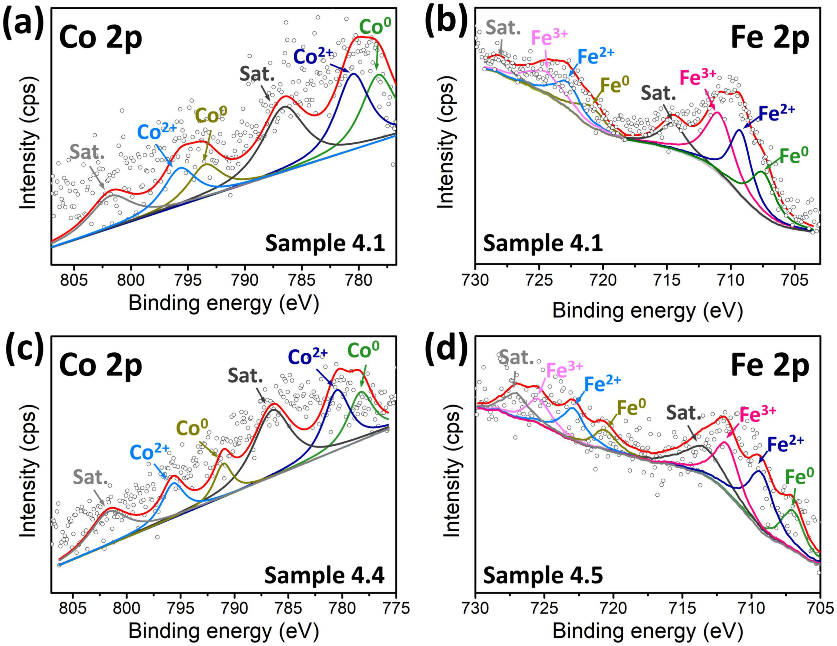

Figure 4.2. High-resolution Co 2p spectra of sample **4.1** (**a**) and sample **4.4** (**c**) and high-resolution Fe 2p spectra of sample **4.1** (**b**) and sample **4.4** (**d**).

Figure 4.3 shows the high-resolution C 1s, O 1s, and N 1s XPS spectra of samples **4.1**, **4.4**, and **4.5**. The high-resolution XPS C 1s peak for all of the samples was conveniently deconvoluted into four individual components appearing at 284.5, 285.4, 286.4, and 288.7 eV, attributable to graphitic C atoms, C atoms bonded to O or N with single or double bonds, and C atoms of carboxylic groups, respectively. **Figure 4.3**, **a-c** shows a representative XPS C 1s peak with the best fitting to its individual components. XPS analysis also revealed the presence of O and N in Co-Fe@(N)G, Co@(N)G, and Fe@(N)G in similar atomic percentage vs C of about 5 wt.% N doping, which was in agreement with the thermal behavior of chitosan that formed N-doped graphene. The high-resolution XPS O 1s peak was also appropriately deconvoluted into four main components, appearing at 530.5, 531.9, 533.1, and 534.2 eV, attributable to O atoms in the metal oxide, C=O, C-O, and O-C=O, respectively. Of note is that the good fit between the experimental and deconvoluted O 1s peaks indicates that O atoms in metal oxides should be present in very low proportions. **Figure 4.3**, **g-i** illustrates the distribution of high-resolution XPS N 1s peak into two major components (pyridinic N and graphitic N) and different N families are in similar proportions for all of the samples.

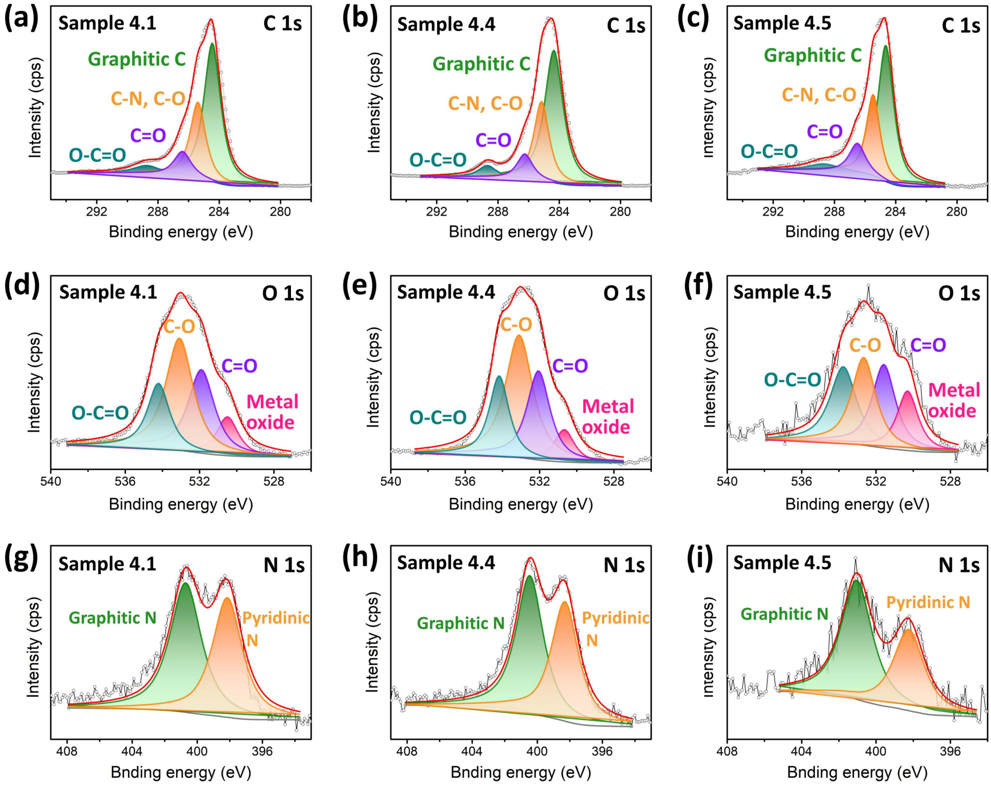

Figure 4.3. High-resolution C 1s (**a**-**c**), O 1s (**d**-**f**), and N 1s spectra (**g**-**i**) of sample **4.1**, sample **4.4** and sample **4.5**.

In accordance to the literature, the occurrence of the graphitization during the pyrolysis at 900 °C of chitosan beads (step *iv* in **Scheme 4.1**) was assessed by Raman spectroscopy. As an example to illustrate this point, **Figure 4.4** includes the Raman spectra recorded for sample **4.1-4.11**. As shown in **Figure 4.4**, the characteristic vibration bands expected for defective graphenes were recorded in the Raman spectra. The bands are 2960, 2700, 1580 and 1350 can be assigned to the D+D', 2D, G and D, respectively. In particular, the relative intensity of the G to the D peak of 1.1 is among the expected values for defective graphene.[7, 13, 14] The presence of N and C in the graphitic residues of samples **4.1** to **4.10** was determined by combustion chemical analyses, giving a consistent value between 3 and 6 wt.% of N. **Table 4.1** summarizes the main analytical data of the samples under study.

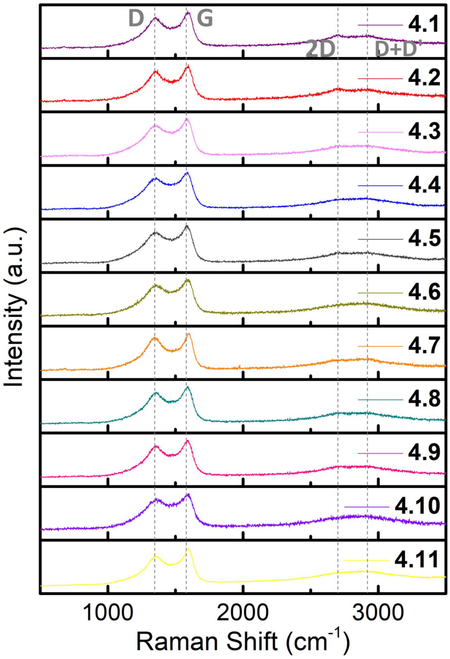

Figure 4.4. Raman spectroscopy of sample **4.1**-**4.11**.

Field-emission scanning electron microscopy shows that at the micrometer scale samples **4.1** to **4.10** are constituted by highly porous, fluffy, cotton-like fibrils. This morphology is inherited from the chitosan aerogel precursor that is also highly porous, cotton-like beads constituted by the agglomeration of chitosan fibrils. Images corresponding to the samples under study are provided in **Figure 4.5**.

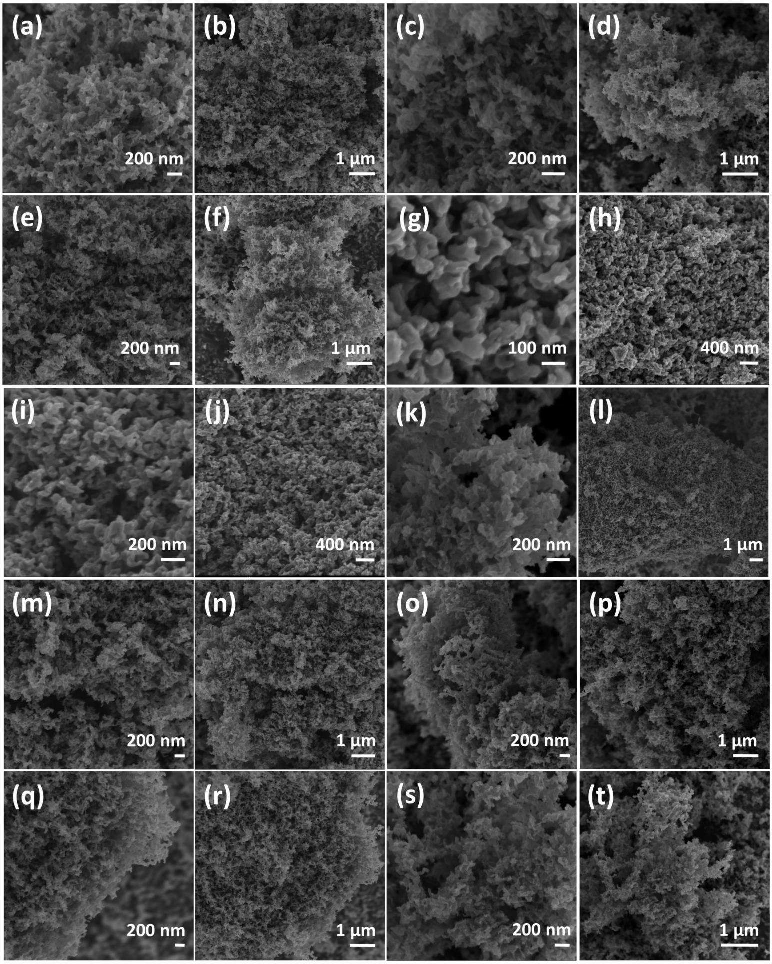

Figure 4.5. FESEM images of samples **4.1**-**4.10**. (**a**, **b**: sample **4.1**; **c**, **d**: sample **4.2**; **e**,

f: sample **4.3**; **g**, **h**: sample **4.4**; **i**, **j**: sample **4.5**; **k**, **l**: sample **4.6**; **m**, **n**: sample **4.7** and **o**, **p**: sample **4.8**; **q**, **r**: sample **4.9** and **s**, **t**: sample **4.10**.)

Transmission electron microscopy images of the samples reveal clear differences depending on the total metal content. These differences will be highly relevant to rationalize the catalytic activity of the samples. Thus, DF-TEM images for samples **4.1**-**4.5** reveal the presence of well dispersed metal as a cloud throughout the carbon matrix without observation in any part of the samples of dots of measurable dimensions that would correspond to small NPs. These images indicate that, at the nanometer resolution of the TEM instrument, samples **4.1** to **4.5** are constituted by clusters and that metal NPs of size above 1 nm are absent in these samples (indicated in **Table 4.1** as CL). **Figure 4.6** presents representative DF-TEM images illustrating metal dispersion throughout the carbon matrix. As it can be seen, DF-TEM images show a bright contrast revealing the location of Co-Fe in the field, but absence of NPs at the 1-2 nm resolution of the TEM instrument. In the literature, there is ample number of precedents showing similar features that are attributed as corresponding to metal CLs.[15, 16] **Figure 4.6** presents DF-TEM images and energy dispersive spectrometry mappings of sample **4.1** at micrometer scale. There were no bright dots detected that could correspond to small NPs in any part of sample **4.1** and EDS mappings of **Figure 4.6** display that the Co-Fe species are highly dispersed.

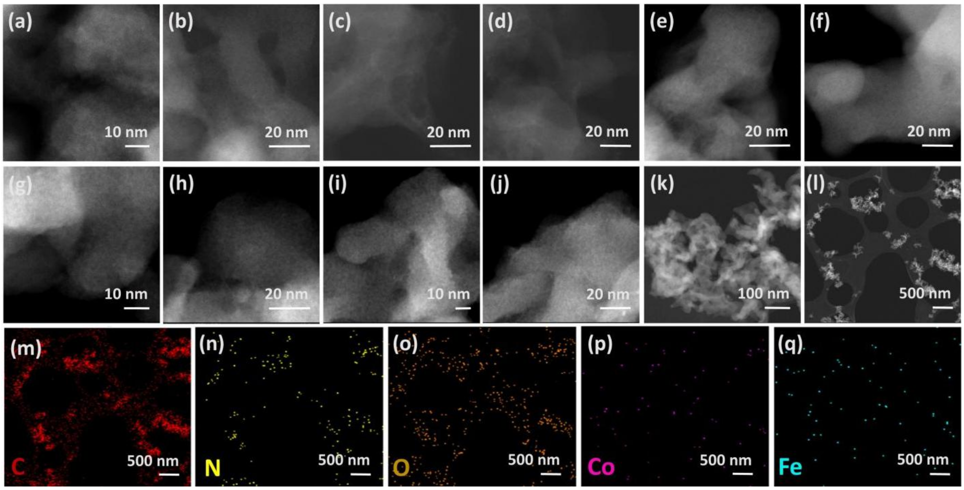

Figure 4.6. DF-TEM images of samples **4.1**-**4.5** and energy dispersive spectrometry mappings of samples **4.1** at micrometer scale. (**a**, **b**, **k**, **l**: sample **4.1**; **c**, **d**: sample **4.2**; **e**, **f**: sample **4.3**; **g**, **h**: sample **4.4**; **i**, **j**: sample **4.5** and **m**-**q**: energy dispersive spectrometry mappings corresponding to **Figure 4.6**, **l**.)

In contrast to the case of samples **4.1**-**4.5**, **Figure 4.7** shows selected DF-TEM images corresponding to samples **4.6** to **4.11**, where bright dots due to small metal NPs can be clearly distinguished. The particle size distribution was determined by measuring a statistically relevant number of these NPs. **Figure 4.7** also includes the corresponding histograms from which the average particle sizes indicated in **Table 4.1** were determined. It should be, however, commented that the average particle size determined by these measurements probably overestimates the average size, since these histograms cannot take into account the presence of an undefined number of CLs without measurable dimensions. In any case, it is clear that the particle sizes of samples **4.4** to **4.8** are very small in the range from 1 to 5 nm. This small particle size is a remarkable fact, considering that the Co and Fe salts were submitted in the pyrolysis step to 900 °C for hours and the well-known effect of the temperature on increasing the size of the metal particles by aggregation.[17] In this regard, it is proposed that the good dispersion of the Co and Fe salts on the highly porous chitosan precursor and the interaction of the metal particles with the defective N-doped graphene support should be the main reasons responsible for these small particle sizes. The difference in particle size between samples **4.1** to **4.5** on one hand, and samples **4.6** to **4.10,** on the other hand, is reasonable considering the previously commented remarkably higher total metal loading of samples **4.4**-**4.10** compared to samples **4.1**-**4.5**.

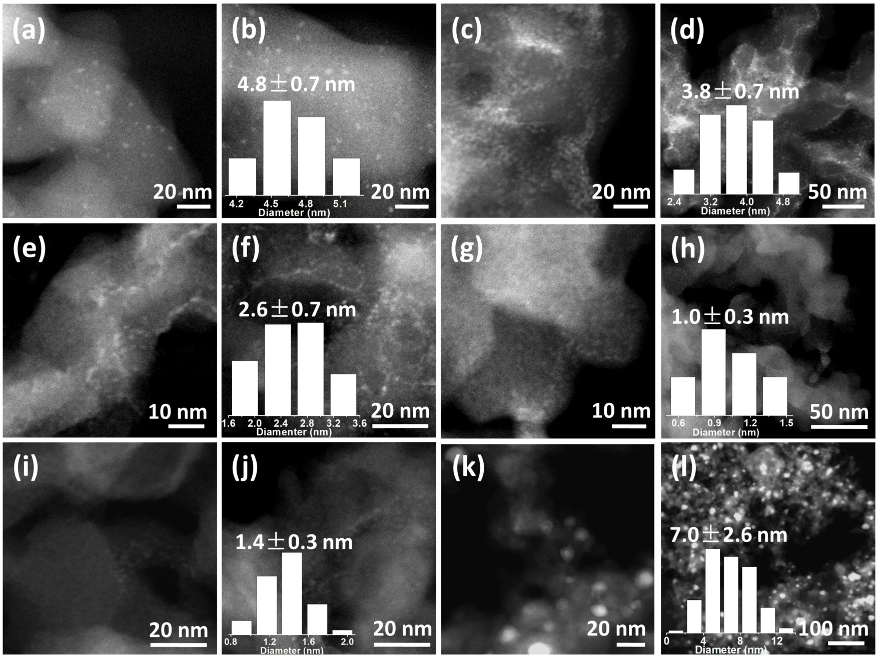

Figure 4.7. DF-TEM images of samples **4.6**-**4.11**. (**a**, **b**: sample **4.6**; **c**, **d**: sample **4.7**; **e**,

f: sample **4.8**; **g**, **h**: sample **4.9**; **i**, **j**: sample **4.10** and **k**, **l**: sample **4.11**. Insets: statistical particle size distributions of samples **4.6**-**4.11** according to the main frame image.)

A careful inspection of DF-TEM images for samples **4.6**-**4.10** shows that in contrast to samples **4.1**-**4.5**, the brightness indicating the presence of metal is concentrated preferentially in some areas, suggesting that the metals are inhomogeneously distributed on the graphene support (compare images of **Figure 4.6** and **4.7**). For samples **4.6**-**4.10**, the Co-Fe metals are mainly located at the ridges and borders of the graphene sheets.

4.2.2 Catalytic activity

The difference in particle size between samples **4.1**-**4.5** and **4.6**-**4.10** having CLs or NPs is crucial to rationalize their distinctive activity and selectivity for CO_2 hydrogenation. Reactions were carried out in pressurized stainless steel tubular reactors at 10 bar under a H_2/CO_2 molar ratio of 7, by heating the system at temperatures from 300 to 450 ^oC in 50 ^oC steps. Each temperature was maintained for 1 h and the reaction products were analyzed at 30, 45 and 55 min after the temperature was set. The complete time of the experiment was 5 h. Preliminary control experiments showed that in the absence of any catalyst or in the presence of N-doped graphitic carbon, CO_2 conversion at 450 ^oC under the reaction conditions was 1.9 and 6.0 %, respectively, with complete selectivity to CH_4.

As expected, as a general trend, CO_2 conversion increased for all the catalysts with the temperature, and product selectivity changed with temperature and conversion, making comparison of selectivity for different catalysts at different conversions meaningless. Nevertheless, remarkable differences in catalytic activity and selectivity were observed for samples **4.1**-**4.5** respect to **4.6**-**4.10**. For the CL series (samples **4.1**-**4.5**), sample **4.2** with intermediate Fe/Co ratio perform worst, while for the NP series (samples **4.6**-**4.10**), CO_2 conversion increased with the decrease in Fe/Co ratio. This different trend could indicate specific arrangements of Fe and Co atoms in CLs or NPs or at the interface with N-doped graphene. Although modelling and theoretical calculations are needed to gain further understanding on how the Fe/Co ratio determines activity, the results clearly show that for the same catalyst mass (40 mg sample no binder employed), samples having CLs were far more active and remarkably selective towards RWGS than those having NPs. To illustrate the different catalytic performance, **Figures 4.8** and **4.9** shows conversion and selectivity for these ten samples at 450 ^{o}C, under the same conditions. As it can be seen in **Figure 4.8**, in spite of the two orders of magnitude lower metal content of samples **4.1**-**4.5**, the samples with CLs were at least two-fold more active than those containing NPs. This higher activity of samples **4.1**-**4.5** with negligible Co and Fe loadings is a reflection of the notable influence of the particle size on the performance, which is more important than the influence of Co-Fe alloying.

Besides differences in conversion, CO was the predominant product in all the samples **4.1**-**4.10**. To further optimize the conditions, the performance of samples **4.1**-**4.5** was studied at different temperatures from 300 to 500 ^{o}C in 50 ^{o}C steps

(**Figure 4.8**, **b**-**f**). Sample **4.1** was the best performing catalyst reaching a conversion at 500 °C of 56 % with 98 % CO selectivity at a space velocity of 600 h^{-1} (**Figure 4.8**, **b**). It should be noted that CO_2 conversion increases as the space velocity decreases and, thus, even higher conversions over 60 % without selectivity change were obtained by using higher amounts (60 mg) of sample **4.1**. Furthermore, sample **4.1** was remarkably stable, as confirmed by performing a 30 h run experiment at 450 °C, observing constant conversion and selectivity.

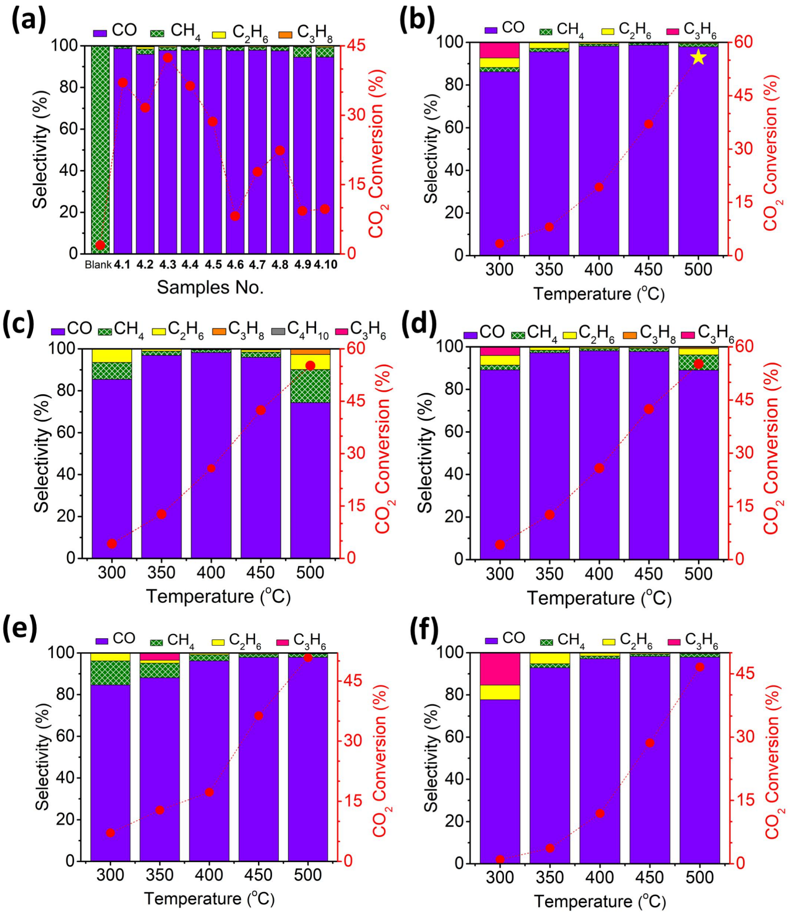

Figure 4.8. CO_2 conversion and selectivity of samples **4.1**-**4.10** at 450 °C (**a**), samples

4.1-**4.5** (**b**-**f**) at temperatures from 300 to 500 °C. (**b**-**f** corresponding to samples **4.1**-**4.5**, respectively.) Reaction conditions: H_2/CO_2 molar ratio of 7, total flow 4 mL/min; pressure: 10 bar; catalyst amount: 40 mg; space velocity: 600 h^{-1}.

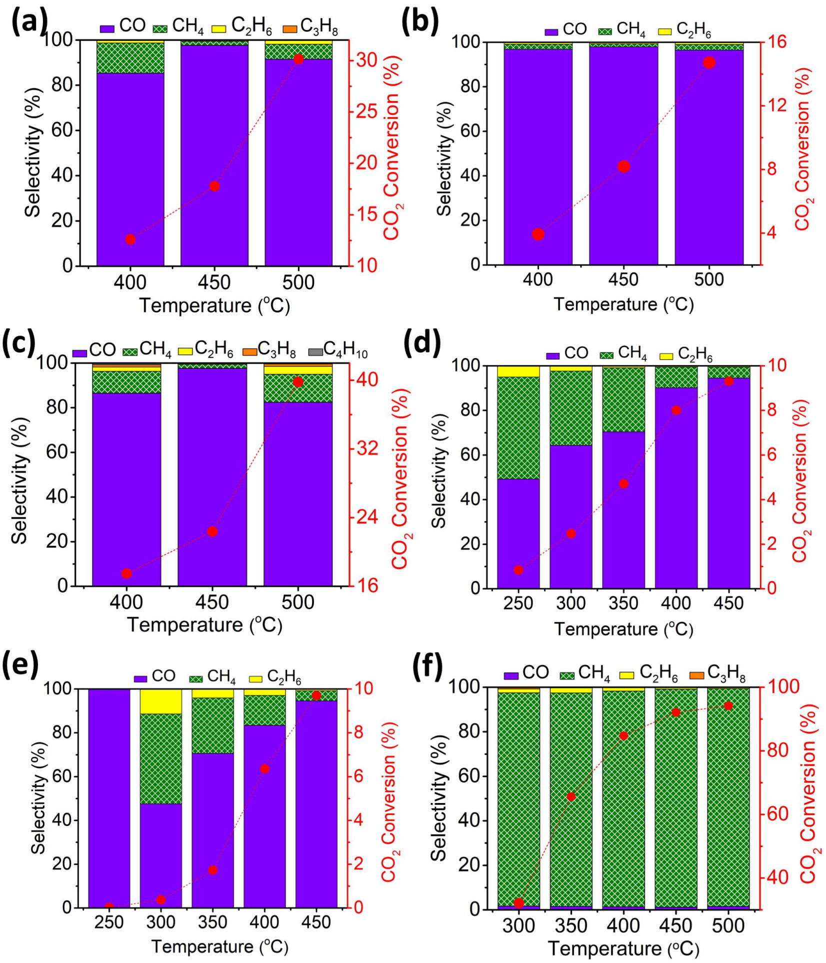

Figure 4.9. CO_2 conversion and selectivity of samples **4.6**-**4.11** at temperatures from 250 to 500 °C. (**a**-**f** corresponding to samples **4.6**-**4.11**, respectively.) Reaction conditions: H_2/CO_2 molar ratio of 7, total flow 4 mL/min; pressure: 10 bar; catalyst

amount: 40 mg; space velocity: 600 h^{-1}.

However, DF-TEM characterization of the used sample **4.1** showed in TEM the appearance of metal NPs (**Figure 4.8**), indicating that some CL agglomeration and particle growth took place under these conditions. This CL agglomeration should be minor since it is not reflected in the catalytic activity of sample **4.1** in the 30 h run, although it could be the cause of longer-term deactivation.

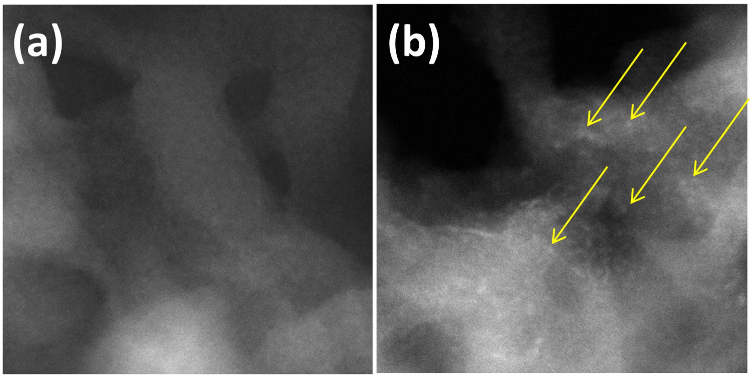

Figure 4.10. DF-TEM images of samples **4.1**. (**a**: fresh; **b**: used.)

4.2.3 Influence of the metal alloy

The influence of alloy increasing the activity can be inferred from the comparison of the performance of samples **4.4** and **4.5** or **4.9** and **4.10**, having only Co or Fe, with those of samples **4.1**-**4.3** and **4.6**-**4.8**, respectively (**Figure 4.6**, **a**). At 450 °C, the activity of sample **4.4** (only Co, 36 % CO_2 conversion) was better than that of sample **4.5** (only Fe, 29 % CO_2 conversion) and both of them were less active that samples

4.1 (37 % CO_2 conversion) and **4.3** (42 % CO_2 conversion). Worth nothing is that higher activity, even in a few percent, may represent a large competitive advantage in large-scale reactions. This influence of alloy is also observed for NPs in which the performance of samples **4.9** and **4.10** is worst in spite that their particle size is notably smaller. It seems that in the range of atomic ratio studied, the increase of the Co proportion results in an increase of the catalytic activity. In addition, alloy also increases significantly the selectivity towards RWGS. **Figure 4.9**, **a**-**c** presents the performance of samples **4.6**-**4.8** at different temperatures, while **Tables 8.4.2.1** to **8.4.2.12** in **CHAPTER 8** gather the full set of data for all samples **4.1**-**4.12**.

4.2.4 Influence of the support

The role of N-doped graphitic carbon as the support was finally addressed by preparing an alternative Co-Fe alloy NPs supported on SiO_2. The catalytic activity data for sample **4.12** is given in **Figure 4.11**. Although Co-Fe alloy NPs supported on SiO_2 exhibits a comparable activity for CO_2 hydrogenation in terms of CO_2 conversion, the main product for sample **4.12** was consistently methane over 50 % selectivity in all the range of temperatures from 300 to 450 ^oC. The presence of minor amounts of ethane (4.8 %) and propane (0.5 %) could be detected at 450 ^oC. This contrasting selectivity for Co-Fe alloy NPs supported on (N)C or SiO_2 illustrate once again that the support plays an important role in the catalyst performance and product selectivity of active centers. This influence of the support derives from the delicate balance among charge transfer from the support to the Co-Fe alloy sites, adsorption of reaction intermediates, and surface acidity, among other properties of the support.

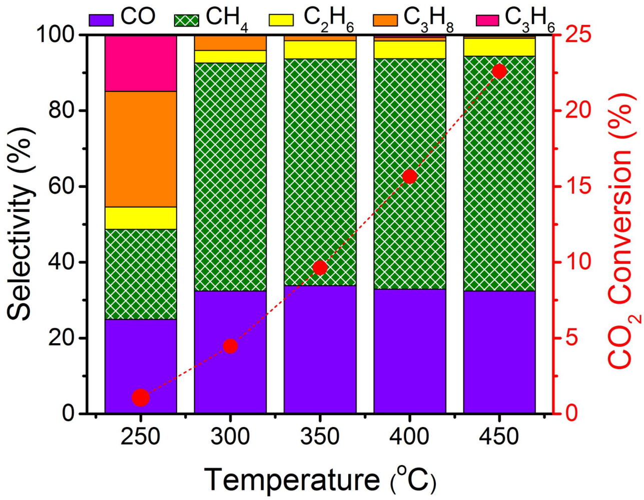

Figure 4.11. CO_2 conversion and selectivity of sample **4.12**. Reaction conditions: H_2/CO_2 molar ratio of 7, total flow 4 mL/min; pressure: 10 bar; catalyst amount: 40 mg; space velocity: 600 h^{-1}.

4.3 Conclusions

The present Chapter has shown the remarkable performance of Co-Fe alloy clusters of (sub)nanometer size supported on defective N-doped graphitic carbon compared with analogous catalysts with metal alloy NPs of size ranging from 1 to 5 nm supported on the same support. A minute metal amount about 0.1 wt.% of highly dispersed Co-Fe clusters is sufficient to achieve optimal catalytic activity with a remarkable RWGS selectivity and high catalytic stability. It seems, however, that clusters agglomeration into nanoparticles could eventually decrease the catalytic activity and product selectivity at times longer than the 30 h run performed.

The present results draw the attention to the influence of the particle size on the nanometer regime and the nature of the support on the activity and selectivity of Co-Fe catalyst in the CO_2 hydrogenation, which is known in Fischer-Tropsch synthesis but much less documented for the CO_2 hydrogenation.

References

[1] E. Onsøyen, O. Skaugrud, Metal recovery using chitosan, *J. Chem. Technol. Biotechnol. (Oxford, Oxfordshire: 1986)*, 49 **(1990)** 395-404.

[2] J. He, A. Dhakshinamoorthy, A.M. Primo Arnau, H. García Gómez, Iron nanoparticles embedded in graphitic carbon matrix as heterogeneous catalysts for the oxidative CN coupling of aromatic NH compounds and amides, *ChemCatChem*, 9 **(2017)** 3003-3012.

[3] A. El Kadib, M. Bousmina, Chitosan bio-based organic-inorganic hybrid aerogel microspheres, *Chem. Eur. J.*, 18 **(2012)** 8264-8277.

[4] R. Valentin, K. Molvinger, F. Quignard, D. Brunel, Supercritical CO_2 dried chitosan: an efficient intrinsic heterogeneous catalyst in fine chemistry, *New J. Chem.*, 27 **(2003)** 1690-1692.

[5] A. Primo, E. Sánchez, J.M. Delgado, H. García, High-yield production of N-doped graphitic platelets by aqueous exfoliation of pyrolyzed chitosan, *Carbon*, 68 **(2014)** 777-783.

[6] J. He, A. Anouar, A. Primo, H. García, Quality improvement of few-layers defective graphene from biomass and application for H_2 generation, *Nanomater.*, 9 **(2019)** 895.

[7] A. Primo, P. Atienzar, E. Sanchez, J.M. Delgado, H. García, From biomass wastes to large-area, high-quality, N-doped graphene: catalyst-free carbonization of chitosan coatings on arbitrary substrates, *Chem. Comm.*, 48 **(2012)** 9254-9256.

[8] D. Wei, Y. Liu, Y. Wang, H. Zhang, L. Huang, G. Yu, Synthesis of N-doped graphene by chemical vapor deposition and its electrical properties, *Nano Letters*, 9 **(2009)** 1752-1758.

[9] G. Abellan, M. Latorre-Sanchez, V. Fornes, A. Ribera, H. García, Graphene as a carbon source effects the nanometallurgy of nickel in Ni, Mn layered double hydroxide-graphene oxide composites, *Chem. Comm.*, 48 **(2012)** 11416-11418.

[10] M. Latorre-Sanchez, P. Atienzar, G. Abellan, M. Puche, V. Fornés, A. Ribera, H. García, The synthesis of a hybrid graphene-nickel/manganese mixed oxide and its performance in lithium-ion batteries, *Carbon*, 50 **(2012)** 518-525.

[11] S.L. Zhang, B.Y. Guan, X.W. Lou, Co-Fe alloy/N-doped carbon hollow spheres derived from dual metal-organic frameworks for enhanced electrocatalytic oxygen reduction, *Small*, 15 **(2019)** 1805324.

[12] S.M. Hwang, S.J. Han, H.G. Park, H. Lee, K. An, K.W. Jun, S.K. Kim, Atomically alloyed Fe-Co catalyst derived from a N-voordinated Co single-atom structure for CO_2 hydrogenation, *ACS Catal.*, 11 **(2021)** 2267-2278.

[13] A. Eckmann, A. Felten, A. Mishchenko, L. Britnell, R. Krupke, K.S. Novoselov, C. Casiraghi, Probing the nature of defects in graphene by Raman spectroscopy, *Nano letters*, 12 **(2012)** 3925-3930.

[14] J. Hong, M.K. Park, E.J. Lee, D. Lee, D.S. Hwang, S. Ryu, Origin of new broad Raman D and G peaks in annealed graphene, *Sci. Rep.*, 3 **(2013)** 1-5.

[15] S. An, G. Zhang, T. Wang, W. Zhang, K. Li, C. Song, J.T. Miller, S. Miao, J. Wang, X. Guo, High-density ultra-small clusters and single-atom Fe sites embedded in graphitic carbon nitride (g-C_3N_4) for highly efficient catalytic advanced oxidation processes, *ACS Nano*, 12 **(2018)** 9441-9450.

[16] R. Wang, J. Yang, X. Chen, Y. Zhao, W. Zhao, G. Qian, S. Li, Y. Xiao, H. Chen, Y. Ye, G. Zhou, F. Pan, Highly dispersed cobalt clusters in nitrogen-doped porous carbon enable multiple effects for high-performance Li–S battery, *Adv. Energy Mater.*, 10 **(2020)** 1903550.

[17] A. Sandoval, A. Gómez-Cortés, R. Zanella, G. Díaz, J.M. Saniger, Gold nanoparticles: Support effects for the WGS reaction, *J. Mol. Catal. A Chem.*, 278 **(2007)** 200-208.

CHAPTER 5

Particle Size Control of Co-Fe Nanoparticles Wrapped on Defective N-doped Graphitic Carbons as Efficient Catalysts for High Selectivity of C_2-C_4 Hydrocarbons in CO_2 Hydrogenation

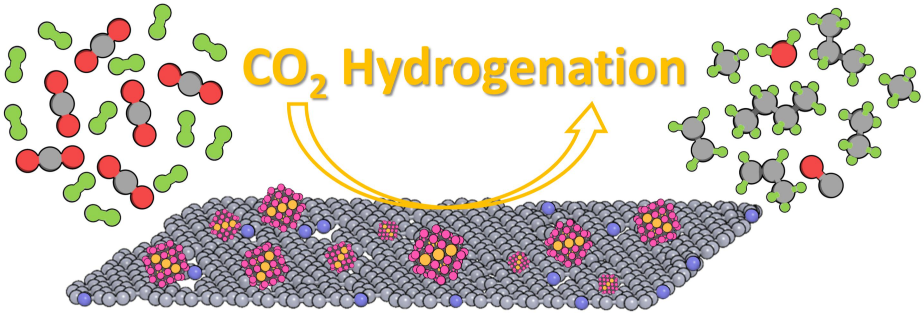

CHAPTER 5

CHAPTER 5

5.1 Introduction

In the previous Chapters, highly selective Co-Fe catalysts for CH_4 and CO under remarkable CO_2 conversions have been described. One of the main challenges in CO_2 hydrogenation is how to control the chain-growth over hydrogenation in a similar way as in the Fischer-Tropsch synthesis.[1, 2] In the Fischer-Tropsch synthesis, starting from CO instead of CO_2, hydrogenation over Co-Fe-based catalysts leads to a distribution of hydrocarbons following the Anderson-Schulz-Flory distribution of carbon atoms that can have a maximum abundance between 6 and 12 carbons.[3-6] In contrast, the chain growth starting from CO_2 is much less favorable and one of the main targets is to obtain C_2 hydrocarbons and beyond products directly from CO_2 in a selectivity higher than 20 %.[7-11]

Continuing with the research objective of the present PhD Thesis, the present Chapter is aimed at the study on the catalytic CO_2 hydrogenation of Co-Fe alloy nanoparticles wrapped on defective N-doped graphitic carbons with a narrow particle size distribution ranging from 7 to 17 nm. It will be shown that Co-Fe alloy nanoparticles of about 10 nm average size embedded on N-doped graphitic carbon can present a remarkable selectivity towards C_2, C_3 and C_4 over 50 % under optimal conditions. In addition, the catalyst exhibits a remarkable stability, conversion and selectivity being maintained in 20 h run measurements. The work derives from the systematic study on the influence of the average Co-Fe alloy NPs size on the catalytic activity of CO_2 hydrogenation. In the case of the related CO hydrogenation, there is a window of particle size that is optimal to achieve the highest selectivity towards long-chain hydrocarbons.[12-15] The results presented in this Chapter seem to indicate that a similar trend could also be operated for the selectivity towards C_{2+} hydrocarbons from CO_2 hydrogenation in the case of Co-Fe alloy NPs and the adequate control of the particle size distribution is necessary.

5.2 Results and Discussion

5.2.1 Samples preparation and characterization

Continuing with the PhD Thesis objectives, it is considered of interest to expand the study on the systematic preparation of Co-Fe alloy NPs wrapped on defective N-doped graphitic carbon having defined particle size. Five samples **5.1-5.5** were prepared following exactly the same preparation procedure that affords a narrow particle size distribution, but increasing the total metal loading from 9 to 23 wt.%. The preparation method is sketched in **Scheme 5.1**, while **Table 5.1** summarizes analytical data of the samples under study. The Co and Fe content were determined by ICP-OES analysis after dissolving the metals in the samples with *aqua regia*, while combustion chemical analysis allows quantification of N and C. The N content of the five samples was similar around 1.5 wt.%.

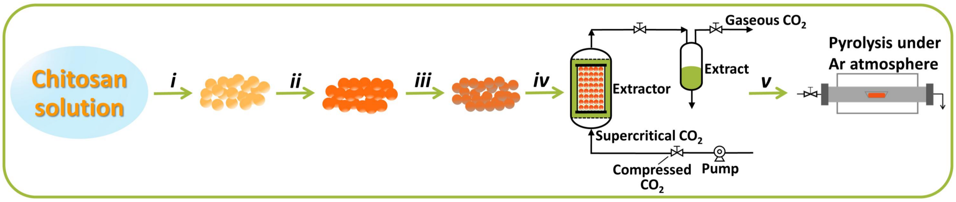

Scheme 5.1. Procedure used to prepare the Co-Fe@(N)C samples under study. *i)* Precipitation in NaOH solution; *ii*) water/ethanol exchange and metal salt

impregnation; *iii*) reduction in $NaBH_4$ ethanol solution; *iv*) supercritical CO_2 drying; *v*) pyrolysis in Ar atmosphere.

Table 5.1. List of samples under study and their main analytical and physicochemical parameters.

Sample No.	Co (wt.%)[a]	Fe (wt.%)[a]	Total Co+Fe content (wt.%)[a]	C (wt.%)[b]	N (wt.%)[b]	Average particle size (nm)[c]
5.1	7.9	1.6	9.5	74.30	1.97	7.3±2
5.2	14.0	3.5	17.5	69.60	1.60	8.8±2
5.3	14.1	3.5	17.5	63.57	1.37	10.5±2
5.4	17.2	4.0	21.3	64.53	1.76	14.1±3
5.5	19.2	4.1	23.3	57.11	1.35	17.3±3

[a] Determined by ICP-OES analysis after dissolving the metals in *aqua regia*; [b] It is assumed that the rest to 100 % is residual oxygen; [c] Determined by DF-TEM.

As it can be seen in **Scheme 5.1**, the precursor of the N-doped graphitic carbon is chitosan, a homopolymer of glucosamine obtained by deacetylation of natural chitin, and the main waste of the fishery industry.[16-18] As mentioned in the previous Introduction, chitosan containing N and C acts simultaneously as a source of C and N forming turbostratic N-doped graphitic carbon.[19-23] One of the known properties of chitosan is to adsorb a large percentage of metal salts from aqueous solutions due to the complexation of the metal ions and the formation of numerous strong hydrogen bridges.[24-26]

In the present case, millimetric alcogel beads of chitosan, formed by flocculation of acid chitosan aqueous solution with NaOH and gradual replacement from H_2O to ethanol, were impregnated with a mixture of cobalt chloride ($CoCl_2$) and iron chloride ($FeCl_2$). After impregnation, the formation of metal alloy NPs was performed by the reduction with $NaBH_4$, subsequent supercritical CO_2 drying and a final pyrolysis. A crucial step in the preparation of the catalysts is the $NaBH_4$ reduction since analogous samples have been prepared following the same procedure, but without the $NaBH_4$ reduction step, resulting in a notoriously broad particle size distribution.

Samples **5.1**-**5.5** were characterized by XRD that shows that the Co-Fe alloy NPs present bcc phase, accompanied by the bcc (200) that only prevails in the case of sample **5.5**.[27-29] No peaks attributable to Co or Fe oxides or carbides were observed. The very similar unit cell parameters of metallic Co and Fe make uncertain to distinguish between separate metal phases or alloys, being necessary electron microscopy to address this issue properly (*vide infra*). Raman spectroscopy was coincident for all the samples and very similar to that reported for the turbostratic graphitic carbon derived from the pyrolysis of chitosan.[19, 20] The presence of the D+D’, 2D, G and D bands appearing at 2960, 2700, 1590 and 1350 cm^{-1} was recorded with a relative intensity of the G over the D band of 1.15, which indicates that the samples are constituted by defective graphene sheets with a quality similar to that of reduced graphenes.[23, 30, 31] **Figure 5.1** presents the XRD patterns and Raman spectra of samples **5.1**-**5.2**.

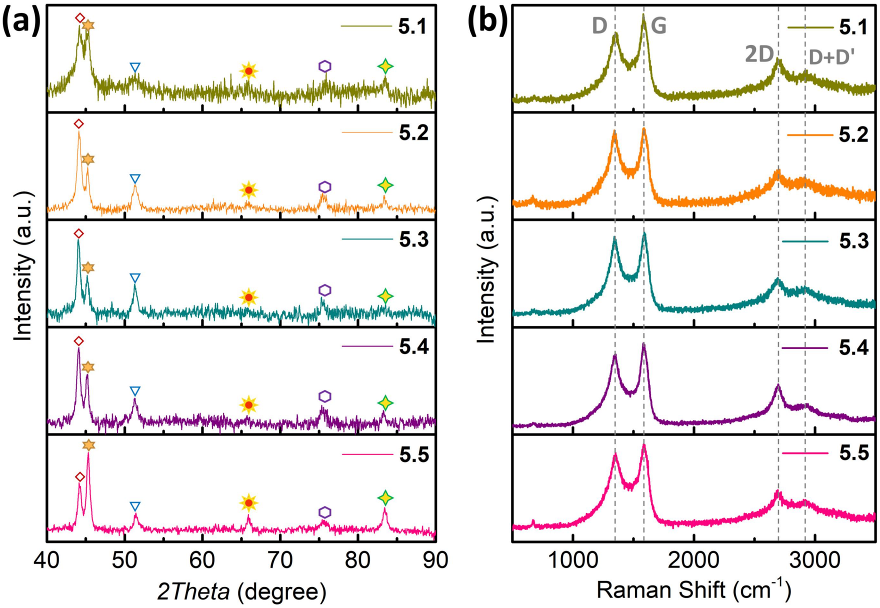

Figure 5.1. XRD patterns (**a**) and Raman spectra (**b**) of the samples **5.1**-**5.5**. Symbols: Co (111) fcc (◇); Co (200) fcc (▽); Co (220) fcc (⬡); Co(0.7)Fe(0.3)(110)bcc (✸); Co(0.7)Fe(0.3)(200)bcc (✹); Co(0.7)Fe(0.3)(211)bcc (✦)

Field emission scanning electron microscopy images of samples **5.1**-**5.5** were very similar showing a spongy, highly-porous carbon residue without any hint of metal particles at the micrometric scale. Selected FESEM images of the materials are provided in **Figure 5.2**.

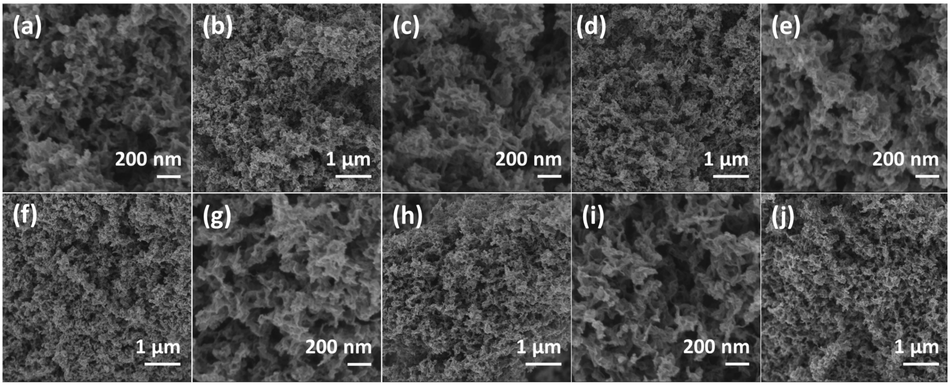

Figure 5.2. FESEM images of samples **5.1**-**5.5**. (**a**, **b**: sample **5.1**; **c**, **d**: sample **5.2**; **e**, **f**: sample **5.3**; **g**, **h**: sample **5.4**; **i**, **j**: sample **5.5**.)

The information provided by transmission electron microscopy was very relevant to understand the nature and size of the MNPs. Thus, in the dark-field mode, TEM images reveal that the samples are constituted by NPs, accompanied with a bright background that corresponds to dispersed metal clusters. **Figure 5.3** provides selected images. Statistical determination of the particle size indicates that the average size increases with the total metal loading raging from 7 to 17 nm (see **Table 5.1**). The tendency of larger particle size as the loading increases is well established in the literature.[11, 32-34] Importantly, the particle size distribution was notably narrow, particularly in comparison of analogous samples prepared omitting the $NaBH_4$ reduction step. **Figure 5.4** provides TEM images of the sample prepared without $NaBH_4$ reduction. Evidently, the use of $NaBH_4$ to obtain metal NPs with narrow particle size distribution is well established in the literature.[35-38] It seems that preformed metal NPs do not tend to evolve into a broad size distribution during the pyrolysis step, probably due to the interaction either with the chitosan fibrils or with the graphitic carbon derived from chitosan during the thermal treatment.

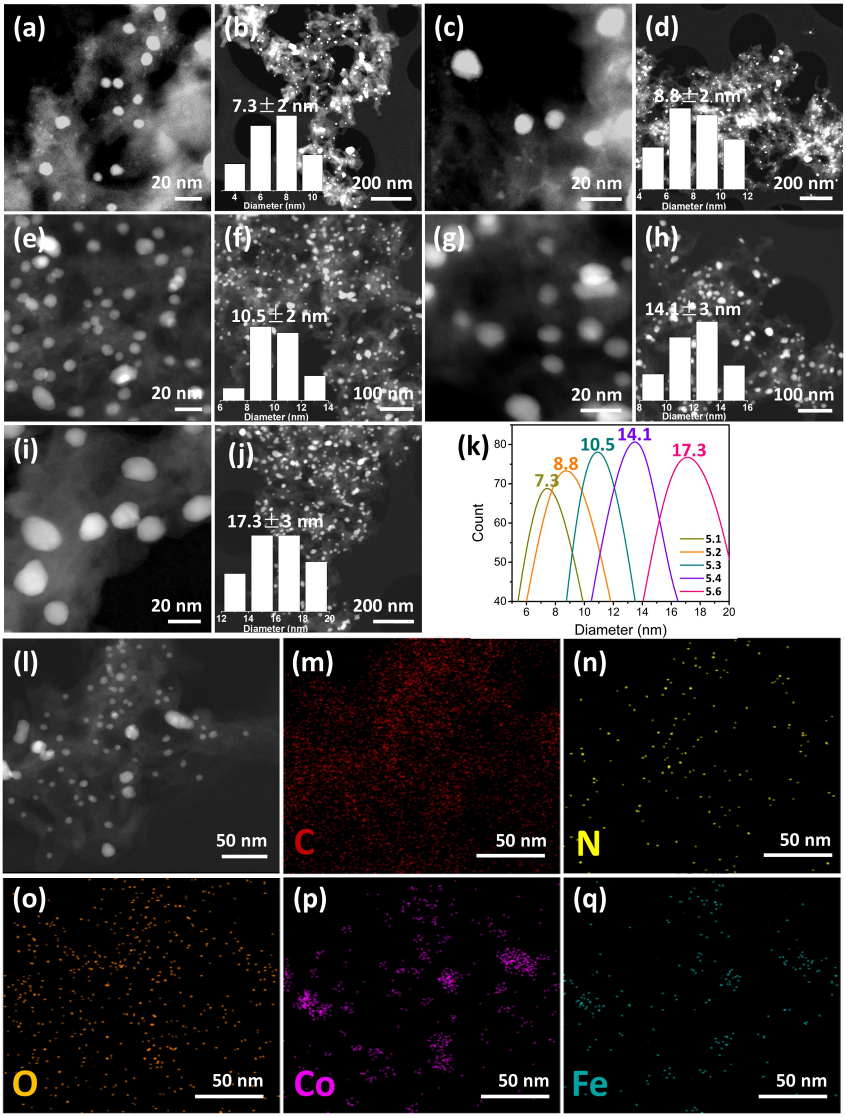

Figure 5.3. DF-TEM images (**a**-**j**), particle size distribution curve (**k**) of samples **5.1**-**5.5** and energy dispersive spectrometry mappings (**m**-**q**) of samples **5.3**. (**a**, **b**:

sample **5.1**; **c**, **d**: sample **5.2**; **e**, **f, l**: sample **5.3**; **g**, **h**: sample **5.4**; **i**, **j**: sample **5.5**. **k**, Inset: statistical particle size distributions of samples **5.1**-**5.5** according to the main frame image.)

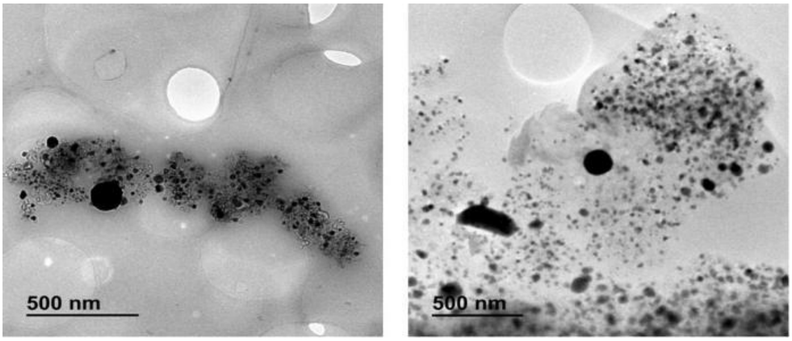

Figure 5.4. TEM images of the sample prepared without reduction showing a broad particle size distribution with the presence of very large nanoparticls.

HRTEM images also give two crucial pieces of information. Measurement of an interplanar distance of 2.1 Å corresponding to the 110 plane, indicates that the NPs are constituted by random Co-Fe alloy, with no evidence of independent Co or Fe NPs. Energy dispersive spectrometry elemental mapping (**Figure 5.3**) of the Co-Fe nanoparticles by TEM also shows a spatial coincidence of Co and Fe in the NPs. The other information is that the Co-Fe alloy NPs within the graphitic carbon matrix are wrapped by a few layers of defective N-doped graphene, observing a large interfacial contact between the two components. **Figure 5.5** presents images providing support to the above claims of random alloy between Co and Fe and the wrap of the Co-Fe alloy NPs by a few layers of graphene.

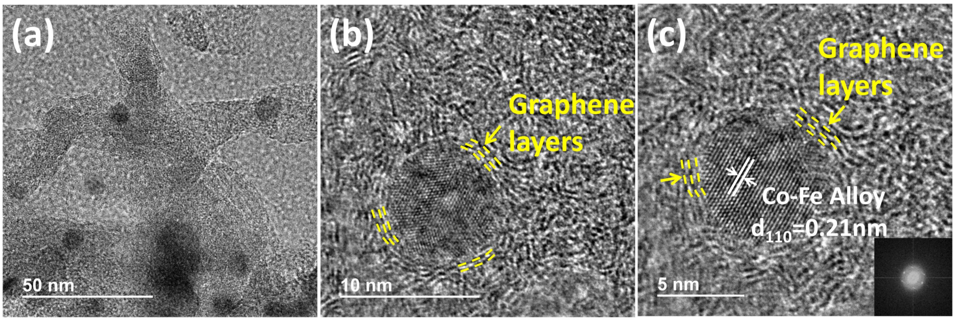

Figure 5.5. HRTEM images at three different magnifications of sample **5.3**. The interplanar distance for the Co-Fe alloy nanoparticle measured by HRTEM is indicated in image **c**. The inset in image **c** corresponds to the Fast Fourier transformed (FFT) electron diffraction of the particle.

5.2.2 Catalytic activity

Reactions were carried out in a pressurized stainless steel tubular reactor at temperatures between 300 and 500 °C. After catalyst activation at 300 °C under N_2, each sample was submitted to a 5 h test starting at 300 °C and increasing the temperature in 50 °C steps. Each temperature is maintained for 1 h. Analysis of the reaction products was carried out on line with multichannel gas chromatography that quantifies the percentage of CO_2, CO, CH_4 and C_{2+} products. Data at each temperature correspond to the average value of three analyses measured for each temperature at 30, 45 and 55 min. Controls in the absence of any catalyst or using N-doped graphitic residue prepared as indicated in **Scheme 5.1**, but in the absence of Co-Fe metals, show a CO_2 conversion at 400 °C of 5 and 10 %, respectively. And methane is the only product detected.

When samples **5.1**-**5.5** were used as catalysts, besides the formation of CH_4 as the main product, formation of CO and C_2-C_4 hydrocarbons was also observed in variable proportions. In the distribution of C_2-C_4 products, ethane was always the major component, followed by propane and less amounts of *n*-butane. In addition, the presence of ethylene (major) and propylene (minor) was also detectable. **Figure 5.6** contains full analytic data of the reaction for each catalyst, at each temperature range from 300 to 500 °C under the conditions screened in the present work. As an example, **Figure 5.7** presents CO_2 conversion and product distribution for samples **5.1**-**5.5**working at 400 °C, 10 bar with a H_2/CO_2 ratio of 7 and a space velocity of 600 h^{-1}. As it can be seen there, the percentage of CO decreases, while the proportion of CH_4 increases in general with the particle size.

General trends were observed in the activity of samples **5.1**-**5.5** as CO_2 hydrogenation catalysts. Conversion of CO_2 increases with temperature, particularly in the range from 300 to 450 °C, while the increase from 450 to 500 °C is less notable. Product selectivity depends on the nature of catalyst, CO_2 conversion and operation conditions, including temperature, H_2/CO_2 ratio and pressure. Caution should be taken when making comparison of selectivity values at different conversions among the various catalysts.

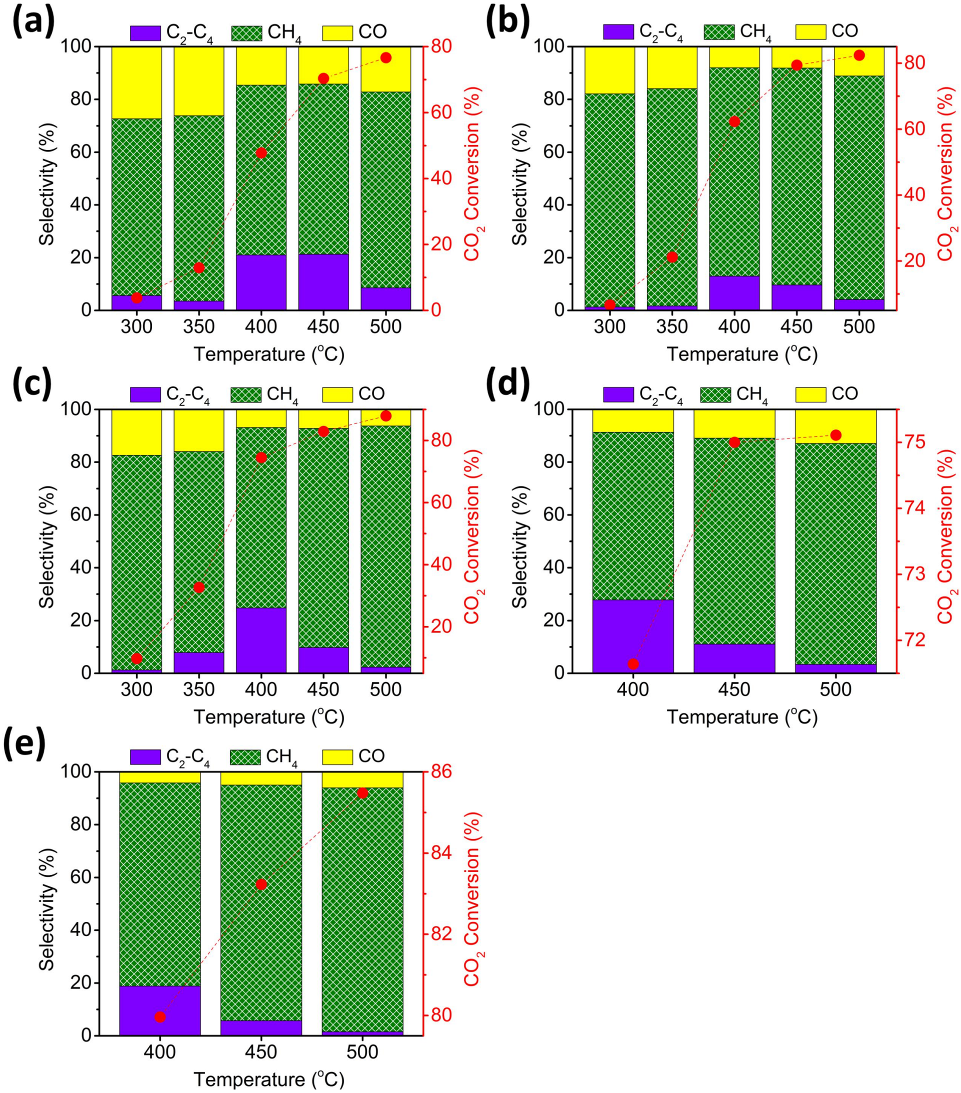

Figure 5.6. CO_2 conversion and selectivity for samples **5.1**-**5.5** at different reaction temperatures, under the same conditions.(**a**-**e** corresponding to samples **5.1**-**5.5**, respectively.) Reaction conditions: H_2/CO_2 ratio of 7, total flow 4 mL/min, 10 bar, 40 mg catalyst.

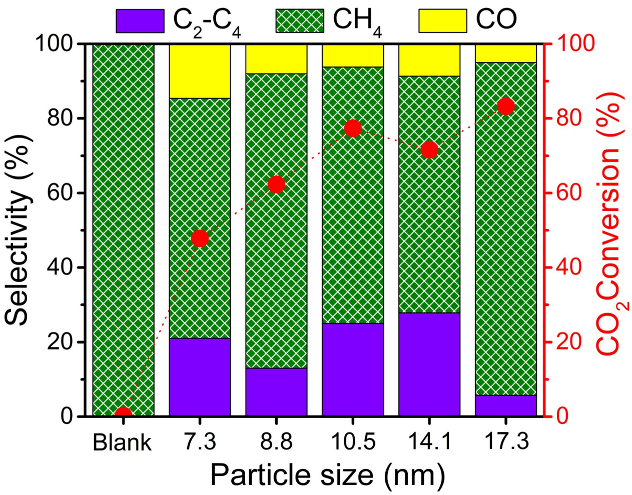

Figure 5.7. CO_2 conversion and selectivity for samples **5.1**-**5.5** having different particle sizes at 400 °C, under the same conditions. Reaction conditions: H_2/CO_2 ratio of 7, total flow 4 mL/min, 10 bar, 40 mg catalyst.

Regarding the unique catalytic behavior of samples **5.1**-**5.5**, a comparison with an analogous Co-Fe sample embedded in defective N-doped graphitic carbon at the same total metal loading and Co/Fe ratio, but exhibiting a broad particle size distribution shows the selective formation of CH_4 under the same conditions. This control sample was prepared by pyrolysis of $CoCl_2$ and $FeCl_2$ adsorbed on chitosan without the $NaBH_4$ reduction step. Similarly, as mentioned in **CHAPTER 4**, samples of Co-Fe alloy clusters supported on N-doped graphitic carbon exhibits over 98 % CO selectivity at high conversions.[39]

Regarding the influence of temperature, it was a general trend that the combined C_{2+} selectivity increased first and then decreased with the temperature, reaching maximum selectivity values at intermediate temperatures of 400 or 450 °C (**Figure 5.6**). Since CO selectivity decreases with temperature, the maximum CH_4 selectivity for all samples **5.1**-**5.5** can be observed at 500 °C.

From the catalytic data it was concluded that samples **5.3** and **5.4** were those exhibiting the highest selectivity to C_{2+} hydrocarbons at the highest conversion. Since the metal loading and the average Co-Fe particle size were lower for sample **5.3** than sample **5.4** (see **Table 5.1**), sample **5.3** was selected for the further stability test and optimization of operation conditions.

5.2.3 Stability study

Stability of the catalytic activity of sample **5.3** was assessed performing four consecutives 5 h runs at 10 bar, H_2/CO_2 ratio of 7 and 600 h^{-1} space velocity. Note that this stability test submits the sample to stress derived from changes in the temperature each 1 h interval and that these conditions are harsher to maintain reproducible conversion and selectivity to the various products than keeping constant operation parameters. **Figure 5.8** shows the results of this stability test. It was observed that catalyst **5.3** was stable with reproducible conversion and selectivity values at each temperature in cycles 2, 3 and 4. It was also noted, however, that particularly at lower temperatures of 300 and 350 °C, the used sample **5.3** outperforms CO_2 conversion and C_{2+} selectivity values than those measured for the fresh sample.

This improvement of the performance has also been observed for Co-Fe alloy clusters supported on N-doped graphitic carbon and attributed to surface modification of the Co-Fe alloy particles by partial oxidation due to CO_2 during the first stages of the test. And the effect of this surface conditioning is more noticeable at low temperatures. However, it is worth noting that reproducibility based on the activity data of the four cycles was remarkable, in which CO_2 conversion in the temperature range from 400 to 500 ^oC was getting higher.

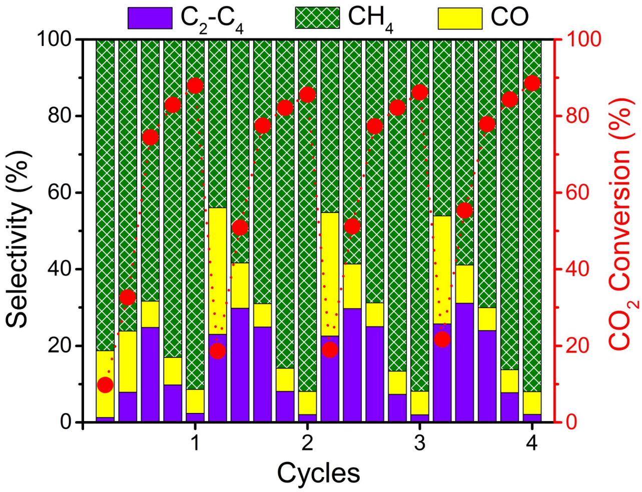

Figure 5.8. Stability test of sample **5.3** at temperature starting from 300 ^oC and increasing in 50 ^oC each steps up to a final temperature of 500 ^oC. Reaction conditions: H_2/CO_2 ratio of 7, total flow 4 mL/min, 10 bar, 40 mg catalyst.

5.2.4 Influence of H_2/CO_2 ratios

Having confirmed catalyst stability, the reaction conditions were optimized to achieve the maximum selectivity for C_{2+} hydrocarbons. Thus, the influence of the

H_2/CO_2 ratio was studied in the range from 7 to 1. A general tendency that CO_2 conversion decreases, while C_{2+} selectivity increases, upon decreasing the H_2/CO_2 ratio was observed. **Figure 5.9** contains the full sets of catalytic data. A good compromise between conversion and C_{2+} selectivity was achieved at H_2/CO_2 ratios of 3 and 4, for which a CO_2 conversion of 51 % with a C_{2+} selectivity over 36 % was measured at a temperature of 400 °C with a H_2/CO_2 ratio of 3.

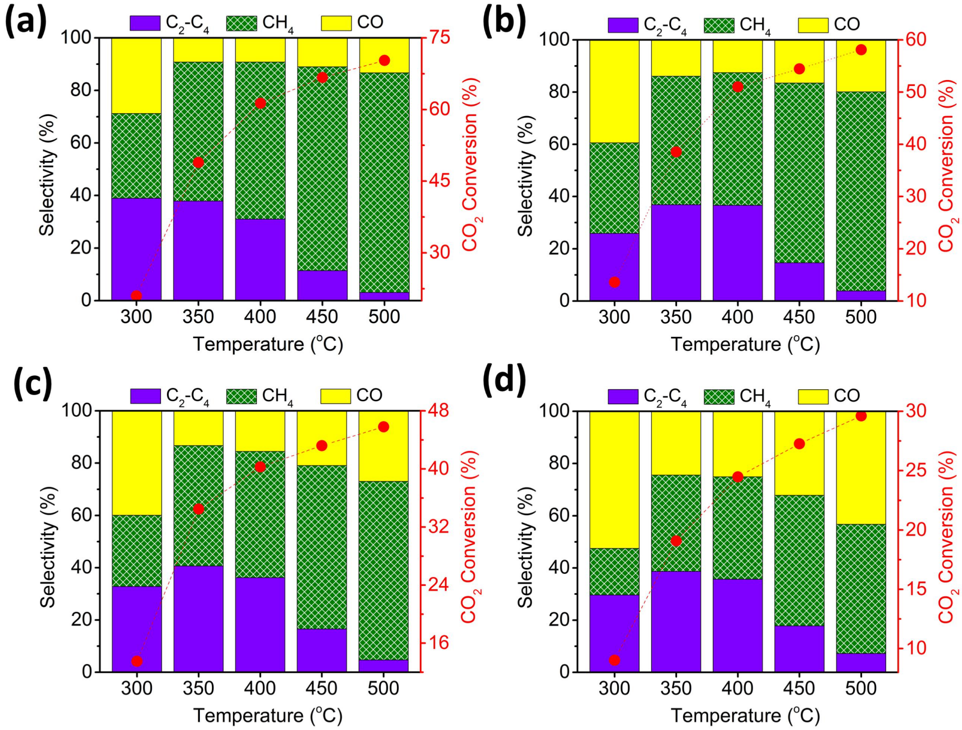

Figure 5.9. CO_2 conversion and selectivity for sample **5.3** at different temperature. (**a**-**d** corresponding to H_2/CO_2 ratio of 4, 3, 2, 1, respectively.) Reaction conditions: total flow 4 mL/min, 10 bar, 40 mg catalyst.

5.2.5 Influence of reaction pressure

Further optimization of C_{2+} selectivity for sample **5.3** was carried out by varying the reaction pressure from 5 to 40 bar. **Figure 5.10** summarizes the results at 300 °C for a H_2/CO_2 ratio of 4. The full activity data are also provided in **Figures 5.11**-**5.13** and **Tables 8.4.3.1**-**8.4.3.21** in **CHAPTER 8**. Evidently, a good balance between CO_2 conversion that increases with the reaction pressure and C_{2+} selectivity was found at 300 °C and 40 bar, for which a CO_2 conversion of 58 % with a C_{2+} selectivity of 44 % was achieved (see **Figure 5.10**). Under these conditions, the percentage of ethane, propane, and *n*-butane being values of 17, 14, and 10 %, respectively, are absolutely remarkable for CO_2 hydrogenation. Of note is that under these H_2 lean conditions, selectivity values of ethylene and propylene as high as 30 % were measured at CO_2 conversion over 34 % (see **Figure 5.11**, **a**, performing at a H_2/CO_2 ratio of 4, 300 °C and 5 bar pressure). Something that could be expected and hints to alkenes as being involved in the reaction mechanism. It should be noted, however, that CO_2 conversion under the present conditions is limited by the space velocity and higher CO_2 conversion values could be easily reached by employing higher amounts of catalyst or diminishing the flow rate.

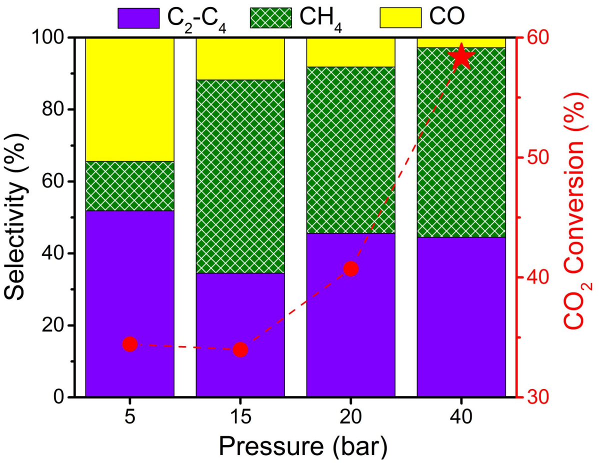

Figure 5.10. CO_2 conversion and selectivity for sample **5.3** at 300 °C on different pressure. Reaction conditions: H_2/CO_2 ratio of 4, total flow 4 mL/min, 40 mg catalyst.

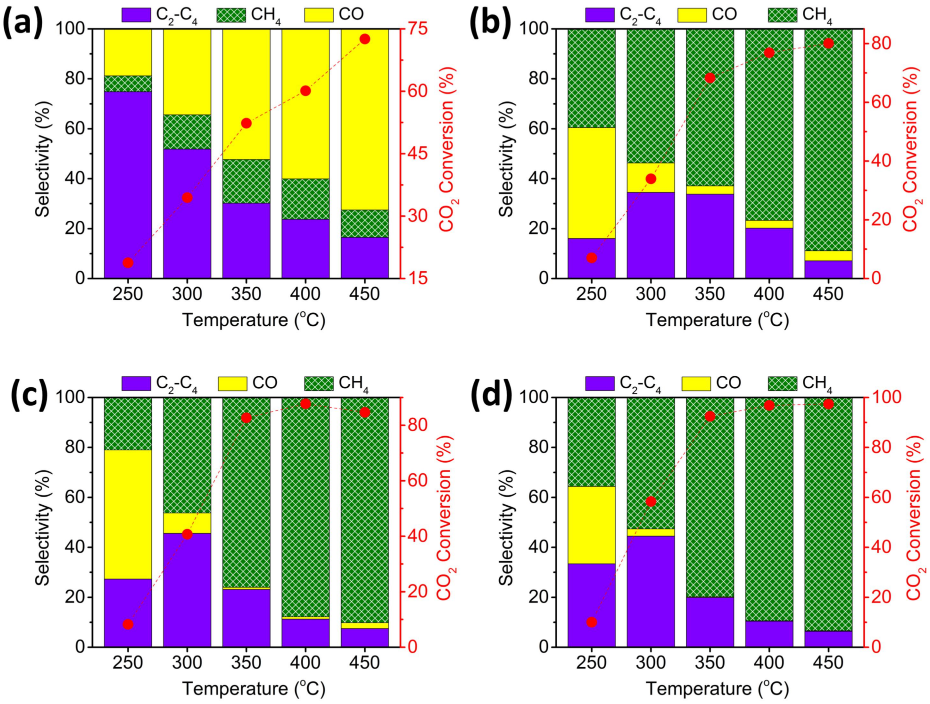

Figure 5.11. CO_2 conversion and selectivity for sample **5.3** at different temperature,

under the same conditions at a H_2/CO_2 ratio of 4. (**a**-**d** corresponding to pressure of 5, 15, 20, 40 bar, respectively.) Reaction conditions: total flow 4 mL/min, 40 mg catalyst.

Similar pressure optimization was also carried out for H_2/CO_2 ratio of 2 and 1 (see **Figures 5.12** and **5.13**). Although C_{2+} selectivity values as high as 61 % were achieved with the percentage of CH_3-CH_3 almost 4 times higher than that of CH_4 for a H_2/CO_2 ratio of 1 at 300 ^{o}C and 15 bar, CO_2 conversion was barely 22 % (see **Figure 5.13**, **b**). The activity of sample **5.3** is markedly higher than that of most active Fe or Co-based catalysts and even ruthenium carbon catalysts we found in the literature. **Table 5.2** summarizes the selectivity for C_2-C_4 hydrocarbons of Fe or Co-based catalysts reported in previous studies on CO_2 hydrogenation.[40-47]

Table 5.2. Comparison of selectivity for C_2-C_4 hydrocarbons of Fe or Co-based catalysts reported in previous studies on CO_2 hydrogenation.[40-47]

Catalyst	Reaction conditions				Metal loading (wt. %)	C (%)	S (%)	S (%)	Ref.
	T (^{o}C)	P (bar)	CO_2/H_2	$m_{catalyst}$ (mg)		CO_2	CH_4	C_2-C_4	
Sample 3	300	40	1/4	40	17.6	58.4	52.7	44.5	This work
Sample 3	300	20	1/4	40	17.6	**40.7**	**46.3**	45.6	
$Fe_2N@C$	250	10	1/4	300	-	33.7	46.0	46.4	[40]

Fe@C	250	10	1/4	300	-	3.3	66.1	32.3	[40]
Ru@C–EDTA-20	160	1	1/3	210	20.2	4.6	99.9	0.1	[41]
Co/CNT	340	10	1/3	220	9.6	36.1	99.3	0.7	[42]
$CoFe_2O_4$_CNT	340	10	1/3	220	8.7	25.2	55.3	37.5	[42]
Fe_2O_3	300	25	1/3	3000	-	30.8	30.1	38.4	[43]
10Fe0.8K0.53Co	300	25	1/3	3000	100	54.6	18.9	32.1	[43]
Ni_3Fe_1/ZrO_2	400	1	1/2	100	-	37.4	86.0	0	[44]
Fe-Co(0.17)	400	10	1/3	200	100	26.5	49.0	39.0	[45]
Fe/Al_2O_3	300	10	1/3	100	-	19.6	36.8	39.4	[46]
NP-MoC_{1-x}/C	300	20	1/3	100	3.66	19.8	17.4	8.9	[46]
Fe	540	-	1/4	1000	100	26.7	15.9	0	[47]
Co	388	-	1/4	1000	100	71.2	98.6	0	[47]

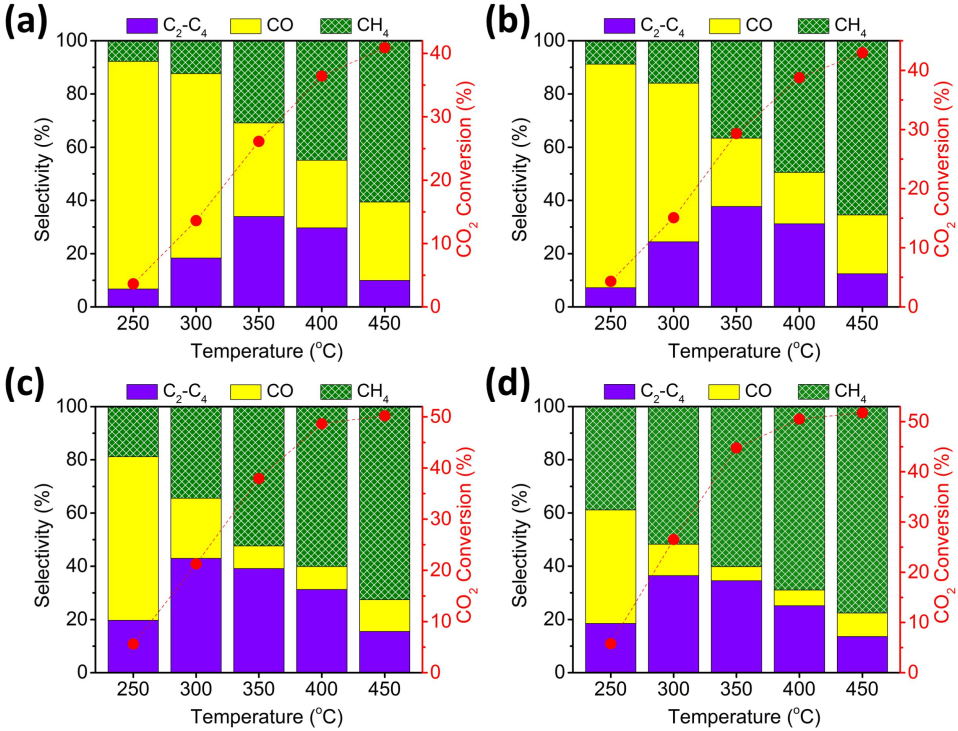

Figure 5.12. CO_2 conversion and selectivity for sample **5.3** at different temperature, under the same conditions at a H_2/CO_2 ratio of 2. (**a**-**d** corresponding to pressure of 5, 7.5, 15, 20 bar, respectively.) Reaction conditions: total flow 4 mL/min, 40 mg catalyst.

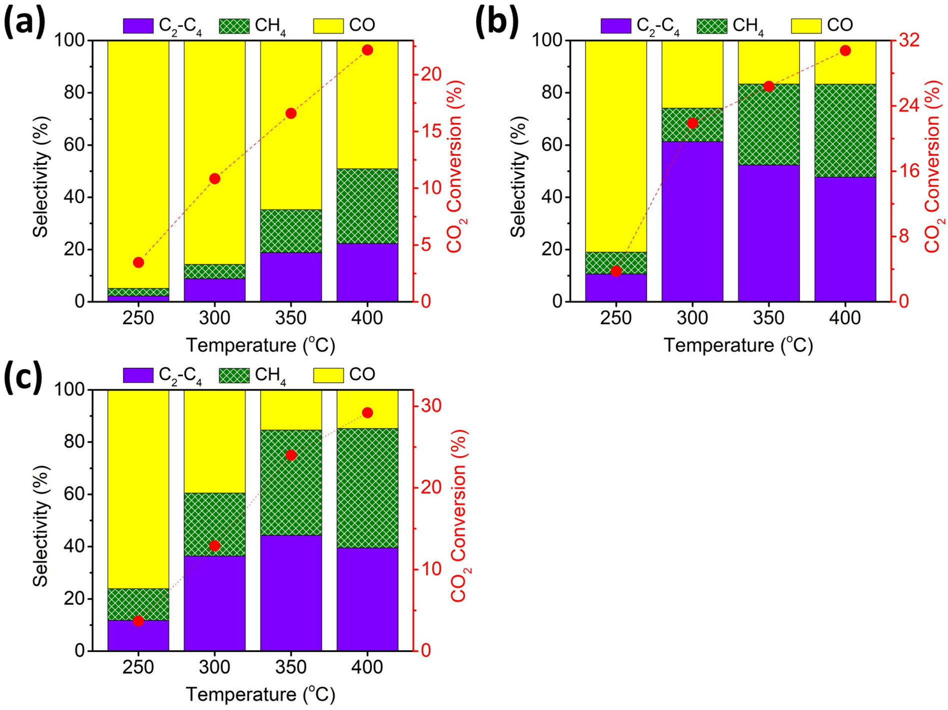

Figure 5.13. CO_2 conversion and selectivity for sample **5.3** at different temperatures, under the same conditions at a H_2/CO_2 ratio of 1. (**a**-**c** corresponding to pressure of 5, 15, 20 bar, respectively.) Reaction conditions: total flow 4 mL/min, 40 mg catalyst.

5.3 Conclusions

The present Chapter has shown the potential of size control on Co-Fe alloy NPs wrapped on N-doped graphitic carbon to increase the of formation C-C bond during CO_2 hydrogenation. There is a window of the Co-Fe alloy particle size that favors the formation of C_2-C_4 hydrocarbons and in this regard, CO_2 hydrogenation follows the trend in Fischer-Tropsch synthesis for which catalysts with a particle size about 10 nm are most adequate to promote the formation of longer-chain hydrocarbons. Under certain operating conditions, high selectivity to C_2-C_4 hydrocarbons and even unsaturated hydrocarbons can be achieved at moderate CO_2 conversions (about 60%). To the best of our knowledge, the high C_2-C_4 selectivity values reached with the present Co-Fe alloy NPs wrapped on N-doped graphitic carbons have not precedent in CO_2 hydrogenation that could be useful to increase the economic attractiveness in the large-scale industrial production.

References

[1] V. Dieterich, A. Buttler, A. Hanel, H. Spliethoff, S. Fendt, Power-to-liquid *via* synthesis of methanol, DME or Fischer-Tropsch-fuels: a review, *Energy Environ. Sci.*, 13 **(2020)** 3207-3252.

[2] Y. Wang, S. Kazumi, W. Gao, X. Gao, H. Li, X. Guo, Y. Yoneyama, G. Yang, N. Tsubaki, Direct conversion of CO_2 to aromatics with high yield *via* a modified Fischer-Tropsch synthesis pathway, *Appl. Catal. B*, 269 **(2020)** 118792.

[3] L. Dai, Y. Chen, R. Liu, X. Li, N. Ullah, Z. Li, CO_2 hydrogenation to C_{5+} hydrocarbons over K-promoted Fe/CNT catalyst: Effect of potassium on structure-activity relationship, *J. Organomet. Chem.*, **(2021)** e6253.

[4] M. Cui, Q. Qian, J. Zhang, Y. Wang, B.B.A. Bediako, H. Liu, B. Han, Liquid fuel synthesis *via* CO_2 hydrogenation by coupling homogeneous and heterogeneous catalysis, *Chem*, 7 **(2021)** 726-737.

[5] F. Perez-Alonso, M. Ojeda, T. Herranz, S. Rojas, J. González-Carballo, P. Terreros, J. Fierro, Carbon dioxide hydrogenation over Fe-Ce catalysts, *Catal. Commun*, 9 **(2008)** 1945-1948.

[6] R-P. Ye, J. Ding, W. Gong, M.D. Argyle, Q. Zhong, Y. Wang, C.K. Russell, Z. Xu, A.G. Russell, Q. Li, CO_2 hydrogenation to high-value products *via* heterogeneous catalysis, *Nat. Commun.*, 10 **(2019)** 1-15.

[7] X. Wang, C. Zeng, N. Gong, T. Zhang, Y. Wu, J. Zhang, F. Song, G. Yang, Y. Tan, Effective suppression of CO selectivity for CO_2 hydrogenation to high-quality gasoline, *ACS Catal.*, 11 **(2021)** 1528-1547.

[8] M. Zabilskiy, V.L. Sushkevich, D. Palagin, M.A. Newton, F. Krumeich, J.A. van Bokhoven, The unique interplay between copper and zinc during catalytic carbon dioxide hydrogenation to methanol, *Nat. Commun.*, 11 **(2020)** 1-8.

[9] F. Zeng, C. Mebrahtu, X. Xi, L. Liao, J. Ren, J. Xie, H.J. Heeres, R. Palkovits, Catalysts design for higher alcohols synthesis by CO_2 hydrogenation: Trends and

future perspectives, *Appl. Catal. B*, **(2021)** 120073.

[10] W. Zhou, K. Cheng, J. Kang, C. Zhou, V. Subramanian, Q. Zhang, Y. Wang, New horizon in C_1 chemistry: breaking the selectivity limitation in transformation of syngas and hydrogenation of CO_2 into hydrocarbon chemicals and fuels, *Chem. Soc. Rev.*, 48 **(2019)** 3193-3228.

[11] J. Zhu, G. Zhang, W. Li, X. Zhang, F. Ding, C. Song, X. Guo, Deconvolution of the particle size effect on CO_2 hydrogenation over iron-based catalysts, *ACS Catal.*, 10 **(2020)** 7424-7433.

[12] W. Wang, S. Wang, X. Ma, J. Gong, Recent advances in catalytic hydrogenation of carbon dioxide, *Chem. Soc. Rev.*, 40 **(2011)** 3703-3727.

[13] J. Albero, Y. Peng, H. García, Photocatalytic CO_2 reduction to C_{2+} products, *ACS Catal.*, 10 **(2020)** 5734-5749.

[14] Y. Gao, S. Liu, Z. Zhao, H. Tao, Z. Sun, Heterogeneous catalysis of CO_2 hydrogenation to C_{2+} products, *Acta Phys. Chim. Sin*, 34 **(2018)** 858-872.

[15] J. Albero, Y. Peng, H. García, Photocatalytic CO_2 Reduction to C_{2+} Products, *ACS Catalysis*, 10 **(2020)** 5734-5749.

[16] A.M. Salaberria, R.H. Diaz, J. Labidi, S.C. Fernandes, Preparing valuable renewable nanocomposite films based exclusively on oceanic biomass-Chitin nanofillers and chitosan, *React. Funct. Polym.*, 89 **(2015)** 31-39.

[17] A. Khanafari, R. Marandi, S. SANATI, Recovery of chitin and chitosan from shrimp waste by chemical and microbial methods, *J. Environ. Health sci. Eng.*, 5 **(2008)** 19-24.

[18] I. Hamed, F. Özogul, J.M. Regenstein, Industrial applications of crustacean by-products (chitin, chitosan, and chitooligosaccharides): A review, *Trends Food Sci. Technol.*, 48 **(2016)** 40-50.

[19] A. Primo, E. Sánchez, J.M. Delgado, H. García, High-yield production of N-doped graphitic platelets by aqueous exfoliation of pyrolyzed chitosan, *Carbon*, 68 **(2014)**

777-783.

[20] C. Lavorato, A. Primo, R. Molinari, H. Garcia, N-Doped graphene derived from biomass as a visible-light photocatalyst for hydrogen generation from water/methanol mixtures, *Chem. Eur. J.*, 20 **(2014)** 187-194.

[21] P. Hao, Z. Zhao, Y. Leng, J. Tian, Y. Sang, R.I. Boughton, C. Wong, H. Liu, B. Yang, Graphene-based nitrogen self-doped hierarchical porous carbon aerogels derived from chitosan for high performance supercapacitors, *Nano Energy*, 15 **(2015)** 9-23.

[22] N. Candu, I. Man, A. Simion, B. Cojocaru, S.M. Coman, C. Bucur, A. Primo, H. Garcia, V.I. Parvulescu, Nitrogen-doped graphene as metal free basic catalyst for coupling reactions, *J. Catal.*, 376 **(2019)** 238-247.

[23] A. Primo, P. Atienzar, E. Sanchez, J.M. Delgado, H. García, From biomass wastes to large-area, high-quality, N-doped graphene: catalyst-free carbonization of chitosan coatings on arbitrary substrates, *Chem. Comm.*, 48 **(2012)** 9254-9256.

[24] M. Vakili, S. Deng, G. Cagnetta, W. Wang, P. Meng, D. Liu, G. Yu, Regeneration of chitosan-based adsorbents used in heavy metal adsorption: A review, *Sep. Purif. Technol.*, 224 **(2019)** 373-387.

[25] F.C. Wu, R.L. Tseng, R.S. Juang, A review and experimental verification of using chitosan and its derivatives as adsorbents for selected heavy metals, *J. Environ. Manage.*, 91 **(2010)** 798-806.

[26] J. Wang, S. Zhuang, Removal of various pollutants from water and wastewater by modified chitosan adsorbents, *Crit. Rev. Environ. Sci. Technol.*, 47 **(2017)** 2331-2386.

[27] G. Chen, R. Gao, Y. Zhao, Z. Li, G.I. Waterhouse, R. Shi, J. Zhao, M. Zhang, L. Shang, G. Sheng, Alumina-supported CoFe alloy catalysts derived from layered-double-hydroxide nanosheets for efficient photothermal CO_2 hydrogenation to hydrocarbons, *Adv. Mater.*, 30 **(2018)** 1704663.

[28] S.M. Hwang, S.J. Han, H.-G. Park, H. Lee, K. An, K.W. Jun, S.K. Kim, Atomically

alloyed Fe-Co catalyst derived from a N-voordinated Co single-atom structure for CO_2 hydrogenation, *ACS Catal.*, 11 **(2021)** 2267-2278.

[29] S.L. Zhang, B.Y. Guan, X.W. Lou, Co-Fe alloy/N-doped carbon hollow spheres derived from dual metal-organic frameworks for enhanced electrocatalytic oxygen reduction, *Small*, 15 **(2019)** 1805324.

[30] A. Eckmann, A. Felten, A. Mishchenko, L. Britnell, R. Krupke, K.S. Novoselov, C. Casiraghi, Probing the nature of defects in graphene by Raman spectroscopy, *Nano letters*, 12 **(2012)** 3925-3930.

[31] J. Hong, M.K. Park, E.J. Lee, D. Lee, D.S. Hwang, S. Ryu, Origin of new broad Raman D and G peaks in annealed graphene, *Sci. Rep.*, 3 **(2013)** 1-5.

[32] Y. Zhu, F. Zaera, Selectivity in the catalytic hydrogenation of cinnamaldehyde promoted by Pt/SiO 2 as a function of metal nanoparticle size, *Catal. Sci. Technol.*, 4 **(2014)** 955-962.

[33] W.J. Wang, Y.W. Chen, Influence of metal loading on the reducibility and hydrogenation activity of cobalt/alumina catalysts, *Appl. Catal.*, 77 **(1991)** 223-233.

[34] H. Wu, Y. Chang, J. Wu, J. Lin, I. Lin, C. Chen, Methanation of CO_2 and reverse water gas shift reactions on Ni/SiO_2 catalysts: the influence of particle size on selectivity and reaction pathway, *Catal. Sci. Technol.*, 5 **(2015)** 4154-4163.

[35] K. Mavani, M. Shah, Synthesis of silver nanoparticles by using sodium borohydride as a reducing agent, *Int. J. Eng. Res. Technol.*, 2 **(2013)** 1-5.

[36] Q.M. Liu, D.B. Zhou, Y. Yamamoto, R. Ichino, M. Okido, Preparation of Cu nanoparticles with $NaBH_4$ by aqueous reduction method, *T. Nonferr. Metal. SOC*, 22 **(2012)** 117-123.

[37] J. Cookson, The preparation of palladium nanoparticles, *Platin. Met. Rev.* , 56 **(2012)** 83-98.

[38] J. Zhao, B. Friedrich, Synthesis of gold nanoparticles *via* the chemical reduction methods, NANO CON **(2017)**.

[39] L. Peng, B. Jurca, a. Primo, A. Gordillo, V. Parvulescu, H. Garcia, Co-Fe clusters supported on N-doped graphene as highly-selective catalysts for reverse water gas shift, *ACS Sustain. Chem. Eng.*, in press **(2021)**.

[40] B. Zhao, M. Sun, F. Chen, Y. Shi, Y. Yu, X. Li, B. Zhang, Unveiling theactivity origin of iron nitride catalyst for efficient hydrogenation of CO_2 to C_{2+} hydrocarbons, *Angew. Chem. Int. Ed. Engl.,* 60 **(2020)** 4496-4500.

[41] J. Cored, A. García-Ortiz, S. Iborra Chornet, M.J. Climent Olmedo, L. Liu, C. Chuang, S. Chang, C. Escudero, P. Concepción, A. Corma, Hydrothermal synthesis of ruthenium nanoparticles with a metallic core and a ruthenium carbide shell for lowerature activation of CO_2 to methane, *J. Am. Chem. Soc.*, 49 **(2019)** 19304-19311.

[42] K.Y. Kim, H. Lee, W.Y. Noh, J. Shin, S.J. Han, S.K. Kim, K. An, J.S. Lee, Cobalt ferrite nanoparticles to form a catalytic Co-Fe alloy carbide phase for selective CO_2 hydrogenation to light olefins, *ACS Catal.*, 10 **(2020)** 8660-8671.

[43] F. Jiang, B. Liu, S. Geng, Y. Xu, X. Liu, Hydrogenation of CO_2 into hydrocarbons: enhanced catalytic activity over Fe-based Fischer-Tropsch catalysts, *Catal. Sci. Technol.*, 8 (**2018)** 4097-4107.

[44] B. Yan, B. Zhao, S. Kattel, Q. Wu, S. Yao, D. Su, J.G. Chen, Tuning CO_2 hydrogenation selectivity via metal-oxide interfacial sites, *J. Catal.*, 374 **(2019)** 60-71.

[45] W. Wang, X. Jiang, X. Wang, C. Song, Fe-Cu bimetallic catalysts for selective CO_2 hydrogenation to olefin-rich C_{2+} hydrocarbons, *Ind. Eng. Chem. Res.*, 57 **(2018)** 4535-4542.

[46] F.G. Baddour, E.J. Roberts, A.T. To, L. Wang, S.E. Habas, D.A. Ruddy, N.M. Bedford, J. Wright, C.P. Nash, J.A. Schaidle, An exceptionally mild and scalable solution-phase synthesis of molybdenum carbide nanoparticles for thermocatalytic CO_2 hydrogenation, *J. Am. Chem. Soc.*, 142 **(2020)** 1010-1019.

[47] R. Mutschler, E. Moioli, W. Luo, N. Gallandat, A. Züttel, CO_2 hydrogenation reaction over pristine Fe, Co, Ni, Cu and Al_2O_3 supported Ru: Comparison and determination of the activation energies, *J. Catal.,* 366 **(2018)** 139-149.

CHAPTER 5

CHAPTER 6

Promotional Effects on the Catalytic Activity of Co-Fe Alloy Supported on Graphitic Carbons for CO_2 Hydrogenation

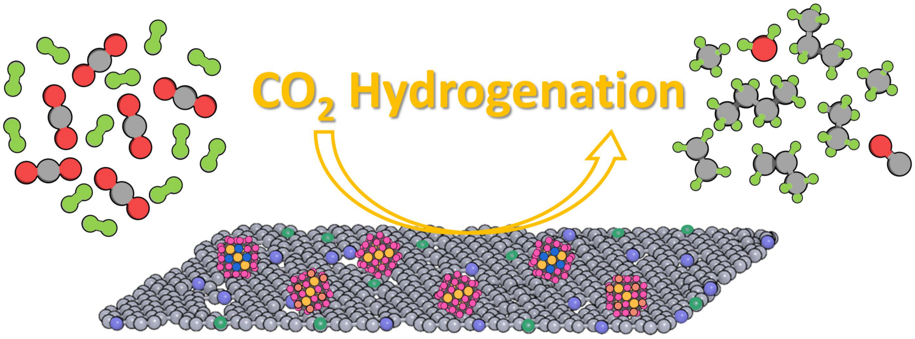

CHAPTER 6

CHAPTER 6

6.1 Introduction

As it was already commented in the Introduction, it is well-known that the presence of certain elements, generally denoted as promoters, can determine the performance of catalysts in CO_2 and CO hydrogenation.[1-9] Specifically alkali metals, such as K and Cs can alter the activity of hydrogenation catalysts,[2, 7, 10-12] by tuning the adsorption properties and surface basicity, among other effects. In this context, it would be of interest to establish which promoters have different effects on the catalytic activity of Co-Fe alloy NPs wrapped on graphitic carbon with the longstanding goal of finding even more active, selective and stable catalysts.

With this objective in mind, the present Chapter focus on the influence that metallic (Na, K, Ca, Pd and Ce) and non-metallic (S) promoters exert on the performance of Co-Fe alloy NPs wrapped on graphitic carbon either N-doped or without N-doping as CO_2 hydrogenation catalysts. Promoters were selected based on precedents reporting the influence of alkali,[13] alkali-earth[14, 15] and noble metals[16-18] on hydrogenation catalysts as well as the poisoning effect of S on the Fischer-Tropsch catalysts.[19-21] Evidence will be presented in this Chapter, showing a significant influence of the promoters on the activity of Co-Fe@(N)C and Co-Fe@C catalysts, driving the selectivity towards CO_2 methanation or reverse water-gas shift.

6.2 Results and Discussion

6.2.1 Samples preparation and characterization

The series of Co-Fe@(N)C and Co-Fe@C catalysts modified with promoters were prepared following three different routes. In two of them, the carbon precursor was chitosan rendering defective N-doped graphitic carbon, while alginate was used as the precursor in the third one for the preparation of Co-Fe alloy NPs on defective graphitic carbons without nitrogen. Chitosan as a polymer of glucosamine with a 6.25 wt.% N, acts in the pyrolysis as a simultaneous source of C and N, while alginate is a copolymer of D-mannuronic and L-guluronic acids condensed through glycosidic β-(1,4) bonds and does not contain N in its composition. **Scheme 1** illustrates the preparation procedures, while **Table 6.1** includes relevant analytical data of samples under study.

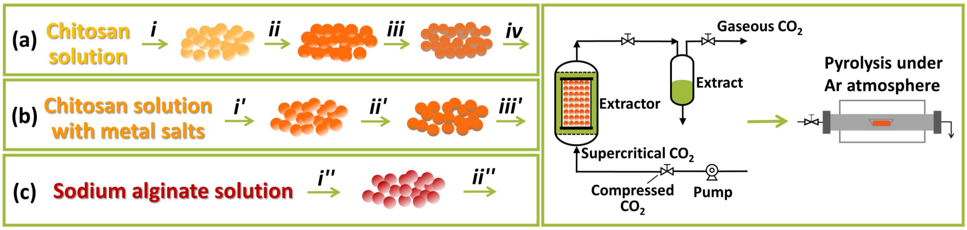

Scheme 6.1. Procedures used to prepare the Co-Fe@(N)C (routes **a** and **b**) and Co-Fe@C (route **c**) under study. Preparation of samples **6.1**, **6.2** and **6.8**-**6.11,** *i*) Precipitation in NaOH solution; *ii*) water/ethanol exchange and metal salt impregnation; *iii*) reduction in $NaBH_4$ ethanol solution; *iv*) supercritical CO_2 drying. (samples **6.8**-**6.11** was performed following route **a** with an additional thiourea impregnation in ethanol in step *iii*). Samples **6.3** and **6.4**, *i'*) Precipitation in NaOH solution; *ii'*) water/ethanol exchange and reduction in $NaBH_4$ ethanol solution; *iii'*)

supercritical CO_2 drying. Sample **6.5**-**6.7**, *i'''*) Precipitation in metal aqueous solution and water/ethanol exchange; *ii'''*) supercritical CO_2 drying.

In route (**a**), chitosan microspheres of millimetric size were first obtained as hydrogel by precipitation of chitosan dissolved in acetic acid aqueous solution into a strong basic NaOH aqueous solution. The resulting chitosan hydrogel was converted into alcogel by a gradual exchange of H_2O by ethanol. Then, Co^{2+} and Fe^{2+} ions were adsorbed onto chitosan beads in ethanol, before chemical reduction with $NaBH_4$ and subsequent supercritical CO_2 drying, followed by pyrolysis. It has been previously observed that $NaBH_4$ reduction of Co^{2+} and Fe^{2+} adsorbed on chitosan renders Co-Fe alloy NPs with narrow particle distributions after pyrolysis in which the average particle dimension can be controlled in a certain extent in the range from 8 to 17 nm, depending on the metal loading.[22]

In route (**b**), Co^{2+} and Fe^{2+} salts were dissolved in acidic chitosan aqueous solution, before the formation of millimetric beads and the exchange of H_2O by ethanol, supercritical CO_2 drying and pyrolysis. Chemical reducing agents are not used in route (**b**) and for this reason the particle size distribution of the Co-Fe alloy NPs tends to be broader than in route (**a**).[23] It should be mentioned that according to prior results, a broader particle size distribution of the Co-Fe alloy NPs tends to favor the formation of CH_4 as the prevalent product.[23]

The precursor of the carbon residue in route (**c**) was sodium alginate that can adsorbs Co^{2+} and Fe^{2+} in an aqueous solution and then, is precipitated with a concentrated solution of divalent metals, either Fe^{2+} in excess (sample **6.5**), Ca^{2+} (samples **6.6**) or $Ce^{3+/4+}$ (sample **6.7**) in H_2O. Alginate is soluble in aqueous solutions at pH values higher than 5, but not soluble in the presence of an excess of di- and tripositive cations, due to the cross-linking of the linear alginate fibrils.[24] The process is completed through the conversion of alginate hydrogel into alcogel by gradual exchange of H_2O with ethanol, followed by supercritical CO_2 drying and pyrolysis at 900 °C. The main difference between routes (**c**), (**a**) and (**b**) derives from the different solubility of chitosan and alginate in acid and neutral-basic aqueous solutions, respectively.[25-27]

Table 6.1. List of samples under study and their main analytical and physicochemical parameters.

Sample No.	Co (wt.%)[a]	Fe (wt.%)[a]	Promoter (wt.%)[a,b]		C (wt.%)[b]	N (wt.%)[b]	Average particle size (nm)[c]
6.1	14.1	3.5	-		63.6	1.4	10.5±2
6.2	18.6	4.4	Pd	0.5	62.9	1.3	10.6±3
6.3	12.4	3.2	-		70.5	1.6	9.7±5
6.4	11.3	2.8	Ce	0.4	67.6	1.4	12.2±6 (CeO_x): 2.4±1
6.5	9.0	38.4	-		47.5	-	21.6±5
6.6	11.3	3.9	Ca	25.8	37.1	-	7.3±3
6.7	16.0	5.4	Ce	1.5	43.4	-	-

6.8	11.7	2.8	S	7.1	49.1	2.2	10.5±2
6.9	11.3	2.2	S	5.2	53.4	2.5	-
6.10	15.6	3.6	S	2.9	55.6	2.7	-
6.11	4.3	1.5	K Na S	1.0 1.4 3.1	60.1	3.9	9.1±6

[a] Determined by ICP-OES analysis after dissolving the metals in *aqua regia*; [b] It is assumed that the rest to 100 % is residual oxygen; [c] Determined by DF-TEM.

As it can be deduced from **Table 6.1**, a set of samples was prepared with the objective of determining the possible influence of promoters, for instance, Pd (samples **6.1** and **6.2**), $Ce^{3+/4+}$ (samples **6.3** and **6.4**), excess of Fe^{2+} (sample **6.5**), Ca^{2+} (sample **6.6**), $Ce^{3+/4+}$ (sample **6.7**) or Na^+ and K^+ in combination with S (sample **6.11**) on the catalytic activity. The percentage of Co, Fe and metallic promoters was determined by ICP-OES after dissolving the metals in the samples with *aqua regia*. In all the cases, except Fe^{2+} and Ca^{2+}, the percentage of promoters was purposely low under 0.5 wt.%. Special cases were Fe^{2+} and Ca^{2+} as promoters. Since alginate beads were precipitated by Fe^{2+} or Ca^{2+}, the content of these metals in samples **6.5** and **6.6** was much higher, about 25 wt.%, compared with the other promoters under study.

Based on the precedents on the influence of S in hydrogenation catalysts, increasing the product selectivity but decreasing the catalytic activity, an additional set of four

Co-Fe@(N)C samples was prepared to contain S. The S content, as well as the percentage of C and N, were quantified by elemental combustion analyses. The relevant analytical details of samples **6.8**-**6.11** are also included in **Table 6.1**. Preparation of samples **6.8**-**6.11** was performed following route (**a**) with an additional thiourea impregnation step in ethanol after the $NaBH_4$ reduction of Co^{2+} and Fe^{2+} salts and before supercritical CO_2 drying and the finial pyrolysis.

Promoter-containing Co-Fe@(N)C and Co-Fe@C samples were characterized by powder XRD, Raman spectroscopy and electron microscopy. As expected in the view of related precedents in the literature, XRD patterns indicate that Co and Fe become reduced to the metallic state during the pyrolysis,[28] with the metal NPs having a variable proportion of fcc and bcc phases. **Figure 6.1** presents the full set of XRD patterns for the samples under study. Importantly, the comparison of the XRD patterns for samples **6.1** and **6.3** lacking promoter with the rest of the samples in which promoters were in low amounts, dose not reveal any difference, except the case of sample **6.6** characterized by a high Ca content. This lack of influence of promoters on the XRD spectra of the Co-Fe@(N)C and Co-Fe@C samples can be attributed, in general, to the low percentage of promoters and their high dispersion. For sample **6.5** containing a large percentage of Fe in its composition, bcc was the prevalent phase. Similarly, for S doped samples, no additional diffraction peaks corresponding to S species could be recorded in the XRD spectra of samples **6.8**-**6.11**. Only in the case of sample **6.6**, the presence of $CaCO_3$ characterized by diffraction peaks at 39.4°, 47.5°, 56.5° was recorded.[29] The formation of $CaCO_3$ can be understood considering the ambient exposure of samples after preparation and the prompt carbonatation of CaO.[30, 31] As mentioned in the previous Chapters, the distinction by XRD between independent Co or Fe phases and Co-Fe alloy is uncertain due to the similarity of the unit cell parameters of Co and Fe.

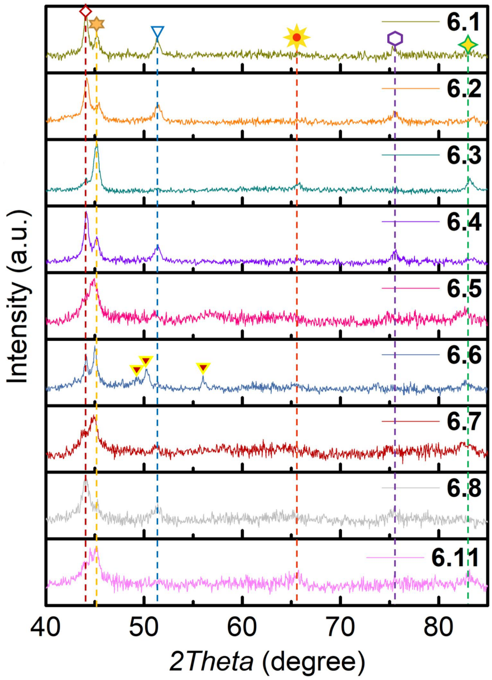

Figure 6.1. XRD pattern of samples **6.1**-**6.8** and **6.11**. Symbols: Co (111) fcc (◇); Co (200) fcc (▽); Co (220) fcc (⬡); Co(0.7)Fe(0.3)(110)bcc (✶); Co(0.7)Fe(0.3)(200)bcc (✹); Co(0.7)Fe(0.3)(211)bcc (✧); $CaCO_3$ (▼).

The graphitic nature of the carbon residue was determined by Raman spectroscopy in which the characteristic D+D’, 2D, G and D peaks appearing at 2960, 2700, 1590 and 1350 cm^{-1}, respectively, were recorded. As an example, **Figure 6.2** collects the Raman spectra of all the samples under study. The intensity of the G vs. the D band

(I_G/I_D) is generally taken as a quantitative indicator of the density of the defects.[32-35] In the present case, the I_G/I_D ratio was between 1.15 and 1.25 that is common for the type of graphitic carbon obtained by pyrolysis of chitosan or alginate.[36-38] The intensity of the overtones is also taken as a sign that the carbon residue is constituted by the stacking of only few graphene layers, these overtones in the region between 2950 and 2700 cm^{-1} being apparent in most of the samples. The Raman spectra essentially coincide with those previously reported for the Co-Fe@(N)C samples lacking promoters in **CHAPTERS 3** and **5**,[22, 23, 39] suggesting that the promoters do not change the graphitic nature of the carbon residue formed in the pyrolysis process.

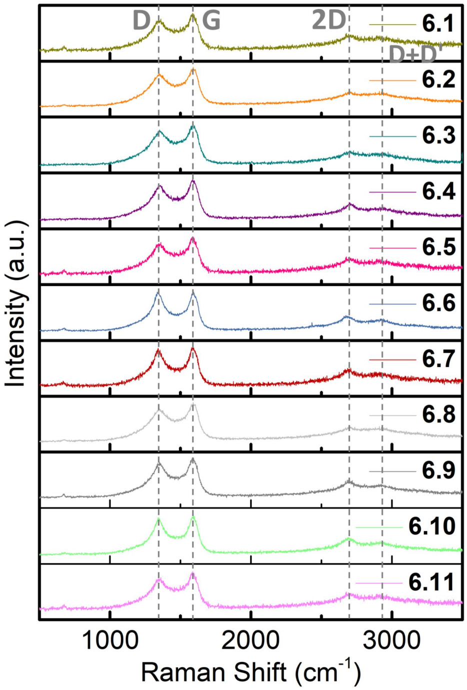

Figure 6.2. Raman spectra of samples **6.1**-**6.11**.

The morphology of the Co-Fe@(N)C and Co-Fe@C samples containing promoters was imaged by field emission scanning electron microscopy. **Figure 6.3** presents the representative images of the Co-Fe@(N)C and Co-Fe@C materials. It was observed that samples **6.1**-**6.11** are characterized by a highly spongy, fluffy structure that derives from the carbonization of the polysaccharide fibrils of the chitosan or alginate after supercritical CO_2 drying.[40] It has been reported in the literature that in contrast to the behavior of hydrogels that give compact beads, conversion of chitosan or alginate microspheres into alcogels and subsequent supercritical CO_2 drying results in highly porous, spongy, large surface area beads of chitosan and alginate.[40] This different behavior is due to the occurrence in dry hydrogels of fibril close packing derived from the formation of hydrogen bridges, while supercritical CO_2 drying diminishes considerably fibril interaction. Interestingly, at the resolution of the FESEM images the presence of Co-Fe NPs was undetectable and no evidence of the presence of promoters on particle morphology could be obtained, even for $CaCO_3$ that is present in a large percentage about 50%.

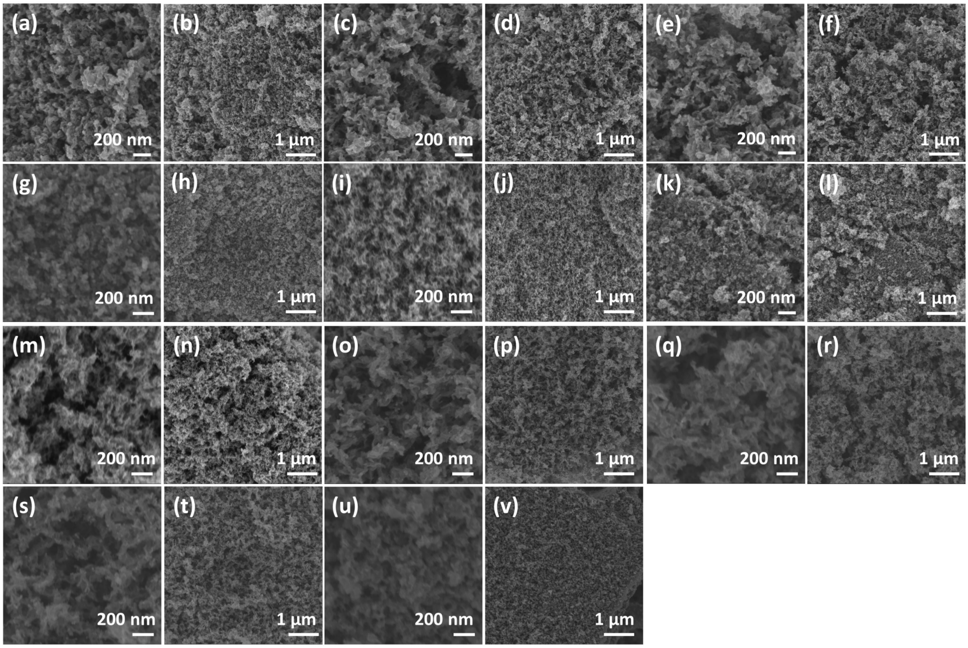

Figure 6.3. FESEM images of the samples **6.1** to **6.11** (**a**, **b**: sample **6.1**; **c**, **d**: sample **6.2**; **e**, **f**: sample **6.3**; **g**, **h**: sample **6.4**; **i**, **j**: sample **6.5**; **k**, **l**: sample **6.6**; **m**, **n**: sample **6.7**; **o**, **p**: sample **6.8**; **q**, **r**: sample **6.9**; **s**, **t**: sample **6.10**; **u**, **v**: sample **6.11**).

Transmission electron microscopy images revealed the presence of Co-Fe alloy NPs. Dark-field images allowed estimating the particle size distribution for each sample based on the measurement of the dimensions of a statistically relevant number of these particles. **Figure 6.4** shows representative images of the samples under study with the corresponding particle size histograms. **Table 6.1** also summarizes the average particle size for each sample. As it can be seen there, most of the samples exhibit a similar average particle size of about 10 nm, except sample **6.5**, in which the particle size was significantly larger, about 18 nm. This larger particle size of sample **6.5** can be easily understood considering the much higher Fe content of this sample.

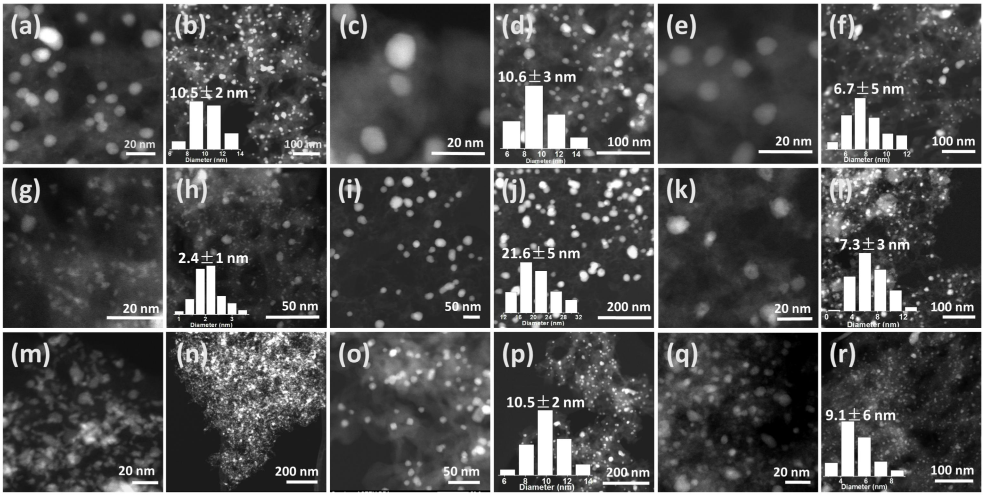

Figure 6.4. DF-TEM images of samples **6.1**-**6.8** and **6.11**. (**a**, **b**: sample **6.1**; **c**, **d**: sample **6.2**; **e**, **f**: sample **6.3**; **g**, **h**: sample **6.4**; **i**, **j**: sample **6.5**; **k**, **l**: sample **6.6**; **m**, **n**: sample **6.7**; **o**, **p**: sample **6.8**; **q**, **r**: sample **6.11**. Insets: statistical particle size distributions of samples **6.1**-**6.8** and **6.11** as corresponding to the main frame image.)

HRTEM images (**Figure 6.5**) allow determining the interplanar distance of the 110 plane in Co-Fe alloy NPs as 0.21 nm which corresponds to the alloy between these two metals.[39] These images also reveal that the Co-Fe alloy NPs are partially covered by one to three layers of defective graphene. The same characterization has been presented in the previous Chapters for similar Co-Fe@(N)C samples.[22, 23, 39] While the presence of promoters in some cases was not apparent from the TEM images, due to their low percentage, EDS analysis revealed the presence of the expected elements in the images. In the case of Ca as a promoter (**Figure 6.6**), it was observed that this element was coating the Co-Fe NPs as determined by analysis of the variation of the elemental composition along with Co-Fe NPs in high-resolution TEM. Therefore, TEM characterization shows that promoters are well dispersed in the Co-Fe@(N)C and Co-Fe@C samples, exhibiting interactions with the Co-Fe alloy NPs supported on few layers of defective graphene.

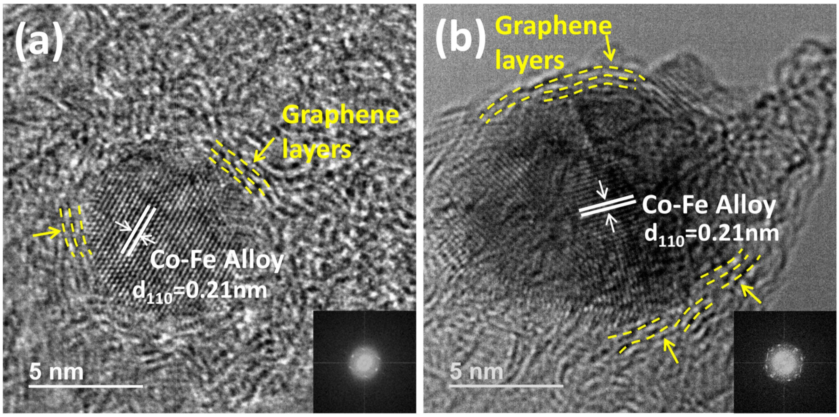

Figure 6.5. HRTEM images of sample **6.1** (**a**) and **6.5** (**b**). The interplanar distance for the Co-Fe alloy nanoparticle measured by HRTEM is indicated in the Figure. The inset corresponds to the Fast Fourier transformed (FFT) electron diffraction of the particle.

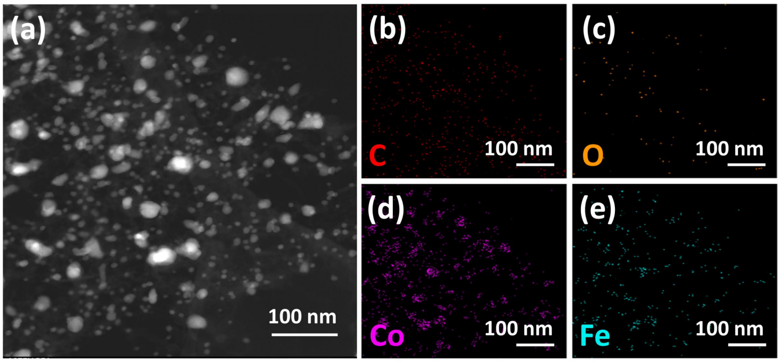

Figure 6.6. DF-TEM image (**a**) and energy dispersive spectrometry mappings (**b**-**e**) of samples **6.5**.

6.2.2 Catalytic activity

The catalytic activity of the samples was evaluated under a continuous flow of a CO_2 and H_2 mixture diluted in Ar in a pressurized tubular, stainless steel reactor with the catalyst as a fixed bed. No binders were employed and the samples were used as fine powders. Each catalyst was tested in the range of temperatures from 300 till 500 ^oC by 50 ^oC increments, without removing the sample from the reactor. After setting a new temperature, the reactor was allowed to equilibrate and, then, the temperature was maintained for 1 h dwell time. The composition of the reaction mixture was determined by gas chromatography analysis at 30, 45 and 55 min after the temperature of the reaction is equilibrated. No differences larger than 10 % among the three analyses were measured in most of the cases and conversion and selectivity values for the temperature were taken as the average of the three independent analyses. For the few cases in which larger differences among the three analyses of the same temperature were found, the value with the highest deviation was not considered. Further details can be found in **CHAPTER 8** describing the experimental procedure.

Preliminary controls at the highest reaction temperature of the study in the absence of any catalysts or using 40 mg of N-doped graphitic carbon or defective graphitic carbon without metals as catalysts showed low CO_2 conversions of 6, 13 and 8 %, respectively, CH_4 being the only detectable product. It has been previously reported that defective graphenes exhibit some activity as CO_2 hydrogenation catalysts.[41] However, as previously found,[22, 23, 39] these CO_2 conversion values of N-doped graphitic carbon or defective graphitic carbon without metals are much lower under operation conditions of the present study than those found when Co-Fe NPs were present in the catalyst.

All the Co-Fe@(N)C and Co-Fe@C samples containing promoters were active as catalysts for CO_2 hydrogenation. The products detected were CH_4, CO and variable percentages of C_2-C_4 hydrocarbons, including a certain proportion of alkenes. As expected, CO_2 conversion increased with the temperature and selectivity varied in each case. Differences in the catalytic activity of the Co-Fe@(N)C and Co-Fe@C samples attributable to the effect of promoters were observed.

The comparison of the catalytic activity of samples **6.1** and **6.2** shows that the presence of Pd in 0.5 wt.% increases CO_2 conversion in the lower temperature range from 300 to 400 °C, with some change in the selectivity. The difference in the catalytic performance of samples **6.1** and **6.2** is presented in **Figure 6.7** and **Tables**

8.4.4.1 and **8.4.4.2** in **CHAPTER 8**. This change was particularly notable at 400 °C, the presence of Pd increasing CH_4 selectivity. This effect can be understood evidently considering that Pd is a better hydrogenating metal than the Co-Fe alloy and it can activate H_2 at lower temperatures. Subsequently, the H atoms on Pd would undergo spillover the Co-Fe NPs. Since CH_4 is the most stable hydrogenation product, the higher catalyst activity caused by Pd as a promoter would be reflected in a higher CH_4 selectivity.

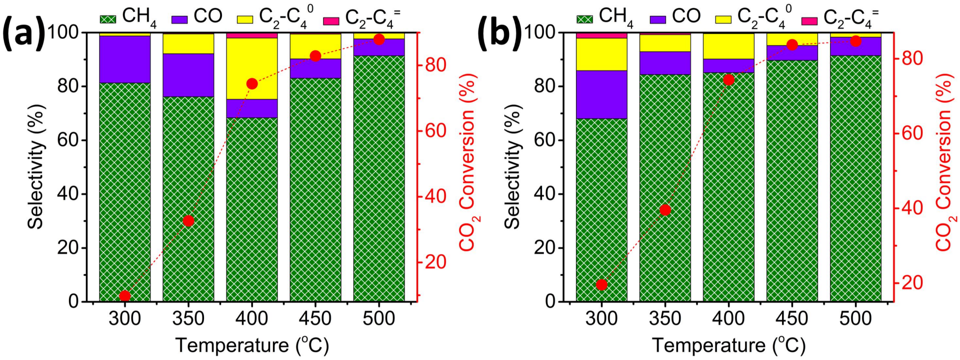

Figure 6.7. CO_2 conversion and selectivity for samples **6.1** (**a**) and **6.2** (**b**) at different temperatures. Reaction conditions: H_2/CO_2 ratio of 7, total flow 4 mL/min, 10 bar, 40 mg catalyst.

Less evident is the influence of Ce as a promoter (see **Figure 6.8** and **Tables 8.4.4.3** and **8.4.4.4** in **CHAPTER 8**). While a comparison of the catalytic activity of Co-Fe@(N)C samples **6.3** and **6.4** shows that Ce does not alter significantly CO_2 conversion, the CO selectivity was considerably reduced at every temperature, favoring the formation of CH_4. In this case, the effect on product selectivity by the promotion of Ce is analogous to that observed for Pd. In contrast, in the case of Co-Fe@C samples derived from alginate, the presence of Ce in a small percentage has a detrimental effect, decreasing substantially CO_2 conversion and resulting in mixtures with a large percentage of CO. This contrasting behavior could indicate that the role of Ce is not H_2 activation, as the case of Pd, but rather interaction with Co-Fe NPs with the tuning of their acidity.

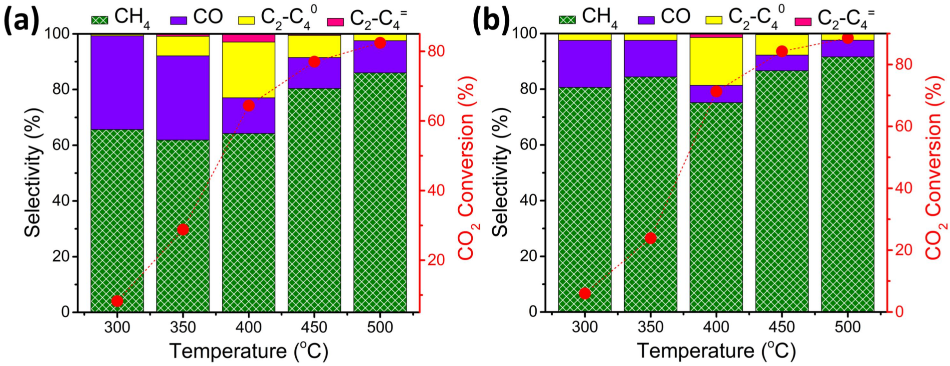

Figure 6.8. CO_2 conversion and selectivity for samples **6.3** (**a**) and **6.4** (**b**) at different temperatures. Reaction conditions: H_2/CO_2 ratio of 7, total flow 4 mL/min, 10 bar, 40 mg catalyst.

As commented previously, an excess of Fe^{2+} or Ca^{2+} was employed in route **c**) to form insoluble alginate beads and these two metals are present in much higher weight percentages in samples **6.5**-**6.7**. The high Fe content of sample **6.5** is responsible for its higher activity at 300 °C compared to sample **6.6**. However, this advantage disappears at the temperature of 350 °C or higher, for which sample **6.6** is significantly more active than sample **6.5** in spite of the higher Fe content of the latter. **Figure 6.9** summarizes the catalytic results for these samples using alginate as the precursor, while data are collected in **Tables 8.4.4.6** and **8.4.4.7** in **CHAPTER 8**. In the case of sample **6.6**, TEM images show an intimate contact between Ca^{2+} and metallic Co-Fe NPs. Ca^{2+} exerts a strong influence on the catalytic performance of Co-Fe@C, increasing CO_2 conversion and CH_4 selectivity. It is proposed that Ca^{2+} increases CO_2 adsorption on Co-Fe@C by forming $CaCO_3$ that is the prevalent phase in the material, resulting in an enhanced conversion.

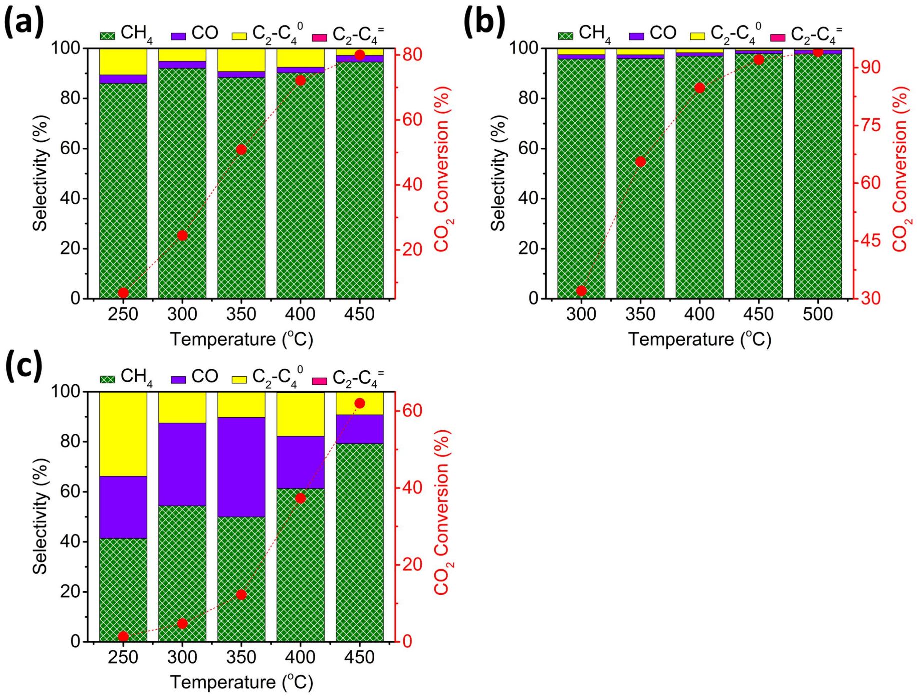

Figure 6.9. CO_2 conversion and selectivity for samples **6.5**-**6.7** at different temperature. (**a**: sample **6.5**; **b**: sample **6.6** and **c**: sample **6.7**.) Reaction conditions: H_2/CO_2 ratio of 7, total flow 4 mL/min, 10 bar, 40 mg catalyst.

Besides the promotion by metallic elements, the effect of S on the catalytic activity of Co-Fe@(N)C was also studied. Samples **6.8**-**6.10** are analogous to sample **6.1** and were prepared similarly, except that thiourea as the source of sulfur was added with three different amounts in the alcogel beads. As shown in **Figure 6.10**, and **Tables 8.4.4.8** to **8.4.4.11** in **CHAPTER 8**, the presence of S produces two clear effects on the catalytic activity of Co-Fe@(N)C. Firstly, CO_2 conversion decreases substantially for the three samples **6.8**-**6.10**, regardless of the S content in the range from 2.9 to 7.1 wt.% under study. Secondly, the selectivity to CO increases dramatically, being over 97 % at the highest temperature tested for these samples. This indicates that S acts as a poison of Co-Fe NPs diminishing their hydrogenation activity of these NPs, resulting in less CO_2 conversion and less hydrogen uptake.

An attempt to increase the catalytic activity of the S-containing Co-Fe@(N)C samples was made in sample **6.11** by adding alkali metal promoters together with S. It was expected that basicity introduced by alkali metals could increase CO_2 conversion in these S-containing samples, by favoring CO_2 adsorption. Although the CO_2 conversion of sample **6.11** was still lower than that of sample **6.1**, a clear increase in activity attributable to the promotion of Na and K was observed, sample **6.11** reaching at 500 ^{o}C a CO_2 conversion of 59 %, lower than the 88 % measured for sample **6.1**, but much higher than the 13 % CO_2 conversion value of sample **6.10**. Notably, the increase in CO_2 conversion observed for sample **6.11** does not influence CO selectivity caused by S poisoning that was for sample **6.11** still over 98 %.

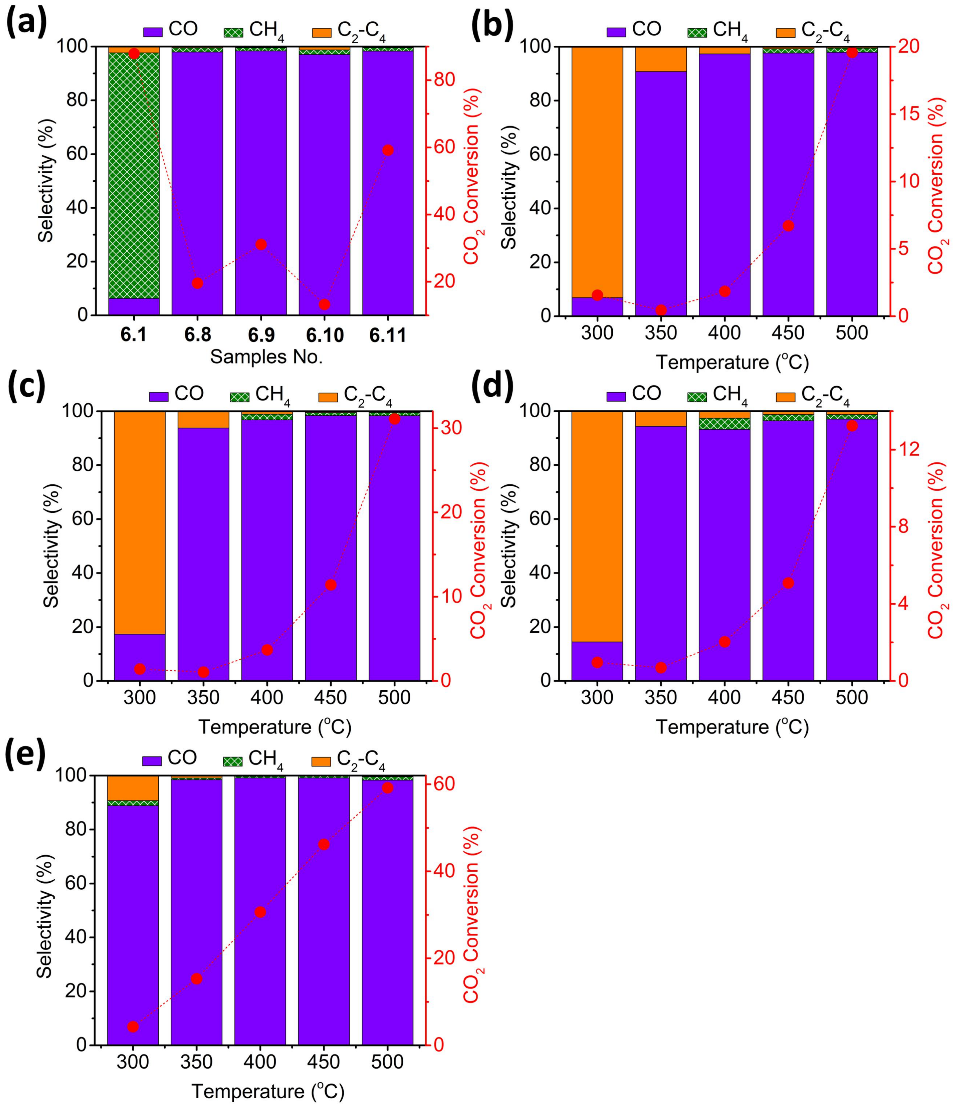

Figure 6.10. CO_2 conversion and selectivity for samples **6.1** and **6.8**-**6.11** with different content of S (**a**) at 500 °C and at different temperature (**b**-**e**). (**b**: sample **6.8**; **c**: sample **6.9**; **d**: sample **6.10** and **e**: sample **6.11**.) Reaction conditions: H_2/CO_2 ratio of 7, total flow 4 mL/min, 10 bar, 40 mg catalyst.

6.3 Conclusions

The present Chapter provides catalytic data of how the activity and selectivity of Co-Fe@(N)C and Co-Fe@C catalysts can be modulated by promoters. Two classes of effects were observed. Pd in a small percentage and Ca in larger concentrations both increase CO_2 conversion and CH_4 selectivity. It is proposed that the promotion of Pd is due to H_2 activation and spillover, while Ca enhances CO_2 adsorption near the active sites. On the other hand, S in a few percent dramatically decreases activity but drives selectivity towards CO. It is proposed that S acts as a poison of the active sites for hydrogenation, disfavoring not only the attack to CO_2, but also successive hydrogen uptake towards CH_4. The effect of S as poison is mitigated partially by the basicity of alkali metals. Overall, the present study shows how a range of catalysts based on Co-Fe alloy NPs supported on graphitic carbon exhibiting contrasting product selectivity to CH_4 or to CO can be prepared by the effective selection of adequate promoters.

References

[1] L. Zhang, Y. Zhang, S. Chen, Effect of promoter SiO_2, TiO_2 or SiO_2-TiO_2 on the performance of CuO-ZnO-Al_2O_3 catalyst for methanol synthesis from CO_2 hydrogenation, *Appl. Catal. A*, 415 **(2012)** 118-123.

[2] D. Li, N. Ichikuni, S. Shimazu, T. Uematsu, Catalytic properties of sprayed Ru/Al_2O_3 and promoter effects of alkali metals in CO_2 hydrogenation, *Appl. Catal. A*, 172 **(1998)** 351-358.

[3] B. Liang, H. Duan, T. Sun, J. Ma, X. Liu, J. Xu, X. Su, Y. Huang, T. Zhang, Effect of Na promoter on Fe-based catalyst for CO_2 hydrogenation to alkenes, *ACS Sustain. Chem. Eng.*, 7 **(2018)** 925-932.

[4] N. Koizumi, X. Jiang, J. Kugai, C. Song, Effects of mesoporous silica supports and alkaline promoters on activity of Pd catalysts in CO_2 hydrogenation for methanol synthesis, *Catal. Today*, 194 **(2012)** 16-24.

[5] L. Xu, Q. Wang, D. Liang, X. Wang, L. Lin, W. Cui, Y. Xu, The promotions of MnO and K_2O to Fe/silicalite-2 catalyst for the production of light alkenes from CO_2 hydrogenation, *Appl. Catal. A*, 173 **(1998)** 19-25.

[6] B. Liu, S. Geng, J. Zheng, X. Jia, F. Jiang, X. Liu, Unravelling the new roles of Na and Mn promoter in CO_2 hydrogenation over Fe_3O_4-Based catalysts for enhanced selectivity to light α-olefins, *ChemCatChem*, 10 **(2018)** 4718-4732.

[7] C.S. Chen, W.H. Cheng, S.S. Lin, Study of reverse water gas shift reaction by TPD, TPR and CO_2 hydrogenation over potassium-promoted Cu/SiO_2 catalyst, *Appl. Catal. A*, 238 **(2003)** 55-67.

[8] G. Jacobs, T.K. Das, Y. Zhang, J. Li, G. Racoillet, B.H. Davis, Fischer-Tropsch synthesis: support, loading, and promoter effects on the reducibility of cobalt catalysts, *Appl. Catal. A*, 233 **(2002)** 263-281.

[9] D.B. Bukur, D. Mukesh, S.A. Patel, Promoter effects on precipitated iron catalysts for Fischer-Tropsch synthesis, *Ind. Eng. Chem. Res.*, 29 **(1990)** 194-204.

[10] W. Li, G. Zhang, X. Jiang, Y. Liu, J. Zhu, F. Ding, Z. Liu, X. Guo, C. Song, CO_2 hydrogenation on unpromoted and M-promoted Co/TiO_2 catalysts (M= Zr, K, Cs): effects of crystal phase of supports and metal-support interaction on tuning product distribution, *ACS Catal.*, 9 **(2019)** 2739-2751.

[11] T. Riedel, G. Schaub, K.W. Jun, K.W. Lee, Kinetics of CO_2 hydrogenation on a K-promoted Fe catalyst, *Ind. Eng. Chem. Res.*, 40 **(2001)** 1355-1363.

[12] M.K. Gnanamani, H.H. Hamdeh, W.D. Shafer, S.D. Hopps, B.H. Davis, Hydrogenation of carbon dioxide over iron carbide prepared from alkali metal promoted iron oxalate, *Appl. Catal. A*, 564 **(2018)** 243-249.

[13] M. Dry, T. Shingles, C.v.H. Botha, Factors influencing the formation of carbon on iron Fischer-Tropsch catalysts: I. The influence of promoters, *J. Catal.*, 17 **(1970)** 341-346.

[14] Z. Tao, Y. Yang, C. Zhang, T. Li, J. Wang, H. Wan, H. Xiang, Y. Li, Effect of calcium promoter on a precipitated iron-manganese catalyst for Fischer-Tropsch synthesis, *Catal. Commun.*, 7 **(2006)** 1061-1066.

[15] A. De La Osa, A. De Lucas, A. Romero, J. Valverde, P. Sánchez, Fischer-Tropsch diesel production over calcium-promoted Co/alumina catalyst: Effect of reaction conditions, *Fuel*, 90 **(2011)** 1935-1945.

[16] A.H. Singleton, R. Oukaci, J.G. Goodwin, Processes and palladium-promoted catalysts for conducting Fischer-Tropsch synthesis, US Patent 6,100,304, **(2000)**.

[17] M. Minnermann, S. Pokhrel, K. Thiel, R. Henkel, J. Birkenstock, T. Laurus, A. Zargham, J.I. Flege, V. Zielasek, E. Piskorska-Hommel, Role of palladium in iron based Fischer-Tropsch catalysts prepared by flame spray pyrolysis, *J. Phys. Chem. C*, 115 **(2011)** 1302-1310.

[18] W. Ning, X. Yang, M. Yamada, Influence of palladium on the hydrocarbon distribution of Fischer-Tropsch reaction over precipitated iron catalyst, *Current Catal.*, 1 **(2012)** 88-92.

[19] H.M.T. Galvis, A.C. Koeken, J.H. Bitter, T. Davidian, M. Ruitenbeek, A.I. Dugulan, K.P. de Jong, Effects of sodium and sulfur on catalytic performance of supported iron catalysts for the Fischer-Tropsch synthesis of lower olefins, *J. Catal.*, 303 **(2013)** 22-30.

[20] R. Anderson, F. Karn, J. Shultz, Factors in sulfur poisoning of iron catalysts in Fischer-Tropsch synthesis, *J. Catal.*, 4 **(1965)** 56-63.

[21] M. Oschatz, N. Krans, J. Xie, K.P. de Jong, Systematic variation of the sodium/sulfur promoter content on carbon-supported iron catalysts for the Fischer-Tropsch to olefins reaction, *J. Energy Chem.*, 25 **(2016)** 985-993.

[22] L. Peng, B. Jurca, A. Gordillo, A. Primo, V.I. Parvulescu, H. García, High C_2-C_4 selectivity (over 40 %) in CO_2 hydrogenation by particle size control of Co-Fe nanoparticles wrapped on N-doped graphitic carbon., *Ener. Environ. Sci.*, **(submitted)**.

[23] B. Jurca, L. Peng, A. Gordillo, A. Primo, V.I. Parvulescu, H. Garcia, Co-Fe nanoparticles wrapped on N-doped graphitic carbon as highly-selective CO_2 methanation catalysts, *ACS Appl. Mater. Interfaces*, (under review) **(2021)**.

[24] Y. Dong, W. Dong, Y. Cao, Z. Han, Z. Ding, Preparation and catalytic activity of Fe alginate gel beads for oxidative degradation of azo dyes under visible light irradiation, *Catalysis Today*, 175 **(2011)** 346-355.

[25] Ø. Skaugrud, A. Hagen, B. Borgersen, M. Dornish, Biomedical and pharmaceutical applications of alginate and chitosan, *Biotechnol. Genet. Eng. Rev.*, 16 **(1999)** 23-40.

[26] M. Latorre-Sánchez, A. Primo, H. García, P-doped graphene obtained by pyrolysis of modified alginate as a photocatalyst for hydrogen generation from water-methanol mixtures, *Angew. Chem. Int. Ed.*, 52 **(2013)** 11813-11816.

[27] M. Latorre-Sánchez, I. Esteve-Adell, A. Primo, H. García, Innovative preparation of MoS_2-graphene heterostructures based on alginate containing $(NH_4)_2MoS_4$ and

their photocatalytic activity for H_2 generation, *Carbon*, 81 **(2015)** 587-596.

[28] Y. Shen, P. Zhao, Q. Shao, D. Ma, F. Takahashi, K. Yoshikawa, *In-situ* catalytic conversion of tar using rice husk char-supported nickel-iron catalysts for biomass pyrolysis/gasification, *Appl. Catal. B*, 152 **(2014)** 140-151.

[29] H.J. Yoon, C.H. Lee, K.B. Lee, Mass transfer enhanced CaO pellets for CO_2 sorption: Utilization of CO_2 emitted from $CaCO_3$ pellets during calcination, *Chem. Eng. J.*, **(2021)** 129584.

[30] A.P.S. Dias, M. Ramos, On the storage stability of CaO biodiesel catalyst. Hydration and carbonation poisoning, *J. Environ. Chem. Eng.*, 9 **(2021)** 104917.

[31] K.W. Ma, H. Teng, CaO powders from oyster shells for efficient CO_2 capture in multiple carbonation cycles, *J. Am. Ceram. Soc.*, 93 **(2010)** 221-227.

[32] L.G. Cançado, A. Jorio, E.M. Ferreira, F. Stavale, C.A. Achete, R.B. Capaz, M.V.d.O. Moutinho, A. Lombardo, T. Kulmala, A.C. Ferrari, Quantifying defects in graphene *via* Raman spectroscopy at different excitation energies, *Nano letters*, 11 **(2011)** 3190-3196.

[33] A. Eckmann, A. Felten, A. Mishchenko, L. Britnell, R. Krupke, K.S. Novoselov, C. Casiraghi, Probing the nature of defects in graphene by Raman spectroscopy, *Nano letters*, 12 **(2012)** 3925-3930.

[34] O. Frank, M. Mohr, J. Maultzsch, C. Thomsen, I. Riaz, R. Jalil, K.S. Novoselov, G. Tsoukleri, J. Parthenios, K. Papagelis, Raman 2D-band splitting in graphene: theory and experiment, *ACS nano*, 5 **(2011)** 2231-2239.

[35] J. Hong, M.K. Park, E.J. Lee, D. Lee, D.S. Hwang, S. Ryu, Origin of new broad Raman D and G peaks in annealed graphene, *Sci. Rep.*, 3 **(2013)** 1-5.

[36] J. He, A. Anouar, A. Primo, H. García, Quality improvement of few-layers defective graphene from biomass and application for H_2 generation, *Nanomaterials*, 9 **(2019)** 895.

[37] A. Primo, P. Atienzar, E. Sanchez, J.M. Delgado, H. García, From biomass wastes

to large-area, high-quality, N-doped graphene: catalyst-free carbonization of chitosan coatings on arbitrary substrates, *Chem. Comm.*, 48 **(2012)** 9254-9256.

[38] A. Primo, E. Sánchez, J.M. Delgado, H. García, High-yield production of N-doped graphitic platelets by aqueous exfoliation of pyrolyzed chitosan, *Carbon*, 68 **(2014)** 777-783.

[39] L. Peng, B. Jurca, A. Gordillo, A. Primo, V.I. Parvulescu, H. García, Co-Fe clusters wrapped on N-doped graphitic carbon as highly-selective catalysts for reverse water gas shift,*ACS Sustain. Chem. Eng.*, (accepted) **(2021)**.

[40] R. Valentin, K. Molvinger, F. Quignard, D. Brunel, Supercritical CO_2 dried chitosan: an efficient intrinsic heterogeneous catalyst in fine chemistry, *New J. Chem.*, 27 **(2003)** 1690-1692.

[41] B. Jurca, C. Bucur, A. Primo, P. Concepción, V.I. Parvulescu, H. García, N-doped defective graphene from biomass as catalyst for CO_2 hydrogenation to methane, *ChemCatChem*, 11 **(2019)** 985-990.

CHAPTER 6

CHAPTER 7

Cu-ZnO Clusters Supported on N-Doped Graphitic Carbons as Highly Selective Catalysts for CO_2 Conversion to Methanol

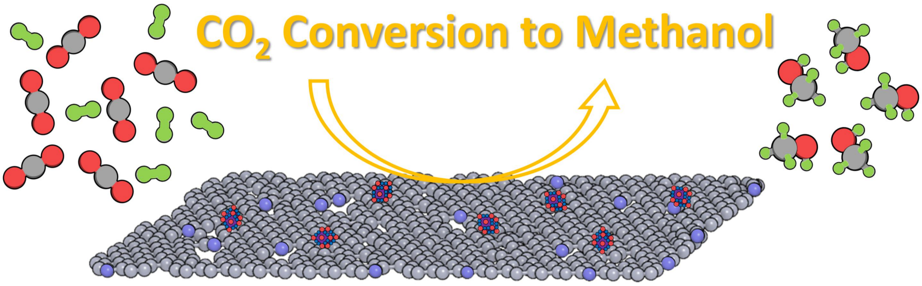

CHAPTER 7

CHAPTER 7

7.1 Introduction

As commented previously, methanol is one of the most valuable products that can derive from CO_2 hydrogenation and its output is predicted to double by 2030.[1-3] In the previous Chapters of this PhD Thesis, highly selective hydrogenation catalysts were developed for the Sabatier reaction in **CHAPTER 3**, the reverse water-gas shift reaction in **CHAPTER 4** and for C_{2+} hydrocarbons in **CHAPTER 5** based on the use of defective graphenes as supports. Therefore, it would also be of interest to explore the possibility to prepare a Cu-ZnO-based catalyst supported on defective N-doped graphitic carbons [Cu-ZnO@(N)C] and to determine its catalytic activity under operation conditions comparative with the thermodynamic limitations of the CO_2 hydrogenation-to-methanol process. In the present Chapter, experimental data support that Cu-ZnO@(N)C is an efficient, selective and stable catalysts for the partial CO_2 hydrogenation to methanol.

7.2 Results and Discussion

7.2.1 Samples preparation and characterization

Initial attempts to prepare Cu-Zn@(N)G were carried out following similar preparation procedures as those described in previous Chapters, including the pyrolysis of chitosan embedding simultaneously Cu and Zn metal ions. In the present case, millimetric alcogel beads of chitosan were impregnated with a mixture of copper acetate and zinc acetate in various molar ratios. However, due to the low boiling point of Zn metal,[4-6] these attempts met with failure because of the complete Zn evaporation during the pyrolysis, with only Cu remaining on the N-doped graphitic carbon after pyrolysis.

To overcome this limitation, Zn has to be incorporated after pyrolysis, while it would be also possible to incorporate simultaneously Cu and Zn after chitosan pyrolysis and the formation of the N-doped graphitic carbon. In the present study, the incorporation of $Cu(OAc)_2$ to chitosan before pyrolysis and the wanted amount of $Zn(OAc)_2$ after the formation of Cu@(N)G has been employed. It was reasoned that in this way, the interaction between Cu nanoparticles and defective graphene as the substrate would be strong[7-9] and the subsequent deposition of $Zn(OAc)_2$ could still form the Cu-Zn bronze under the reaction conditions.[10, 11]

A series of samples with different atomic Cu/Zn ratios were prepared, trying to maintain the total Cu+Zn metal content, meanwhile covering a Cu-Zn ratio of 3 that is close to the composition of the benchmark Cu-ZnO/Al_2O_3 catalyst.[12, 13] **Scheme 7.1** illustrates the steps performed in the preparation of Cu-ZnO@(N)C, while **Table 7.1** summarizes analytical data of the samples under study.

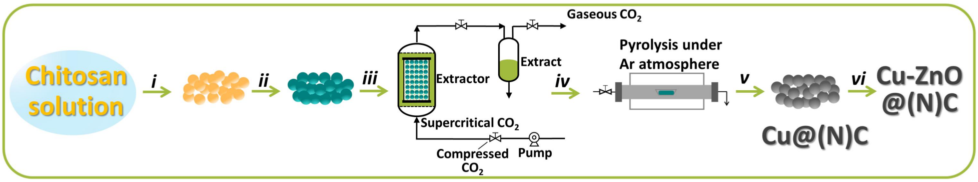

Scheme 7.1. Procedure used to prepare the Cu-ZnO@(N)C samples under study. *i)* precipitation in NaOH solution of chitosan hydrogel; *ii*) water/ethanol exchange and $Cu(OAc)_2$ impregnation; *iii*) supercritical CO_2 drying; *iv*) pyrolysis in Ar atmosphere; *v*) $Zn(OAc)_2$ impregnation; *v*) thermal treatment.

The contents of Cu and Zn in the samples were determined by ICP-OES elemental analysis after treating the Cu-ZnO@(N)G samples with *aqua regia*. The data summarized in **Table 7.1** showed that the total metal content of sample under study varied from 7.9 to 14.2 wt.%, while the Cu/Zn ratio ranges from 0.52 to 8.2.

Table 7.1. List of samples under study and their main analytical and physicochemical parameters.

Sample No.	Cu (wt.%)[a]	Zn (wt.%)[a]	Total Cu+Zn (wt.%)[a]	Molar ratio (Cu/Zn)	C (wt.%)[b]	N (wt.%)[b]	Average particle size (nm)[c]
7.1	7.9	-	7.9	-	77.0	5.4	1.4±0.3
7.2	4.8	9.4	14.2	0.53	64.7	3.9	1.4±0.4
7.3	7.7	2.4	10.1	3.3	70.4	7.1	1.2±0.3
7.4	8.4	2.0	10.4	4.2	72.4	5.1	1.0±0.3
7.5	8.2	1.6	9.8	5.2	68.4	4.5	1.3±0.2
7.6	8.7	1.1	9.8	8.2	72.5	5.1	1.0±0.2

[a] Determined by ICP-OES analysis after dissolving the metals in *aqua regia*; [b] It is assumed that the rest to 100 % is residual oxygen; [c] Determined by DF-HRTEM.

Samples **7.1**-**7.6** were characterized by XRD and Raman spectroscopy (**Figure 7.1**). In the XRD patterns, the expected diffraction peaks corresponding to metallic Cu and ZnO were recorded for Cu-ZnO@(N)C. The peaks that represent Cu (PDF No. 70-3038) and ZnO (JCPDS No. 36-1451) are clearly identified in **Figure 7.1**, **a** for samples **7.1**-**7.6**.[14, 15] The relative intensity of the peaks corresponding to ZnO were in accordance with the relative proportion of ZnO in comparison to Cu. The defective nature of N-doped graphitic carbons was established by Raman spectroscopy, where the characteristic G and D bands appearing at 1590 and 1350 cm^{-1}, together with resolved overtone 2D at 2700 cm^{-1} were recorded.[16, 17] **Figure 7.1**, **b** plots a representative Raman spectrum recorded for the Cu-ZnO@(N)G samples. The relative intensity ratio of the G vs. the D band was about 1.15 and their width at half height is in accordance with values for N-doped graphitic carbons previously reported from chitosan.[18-20]

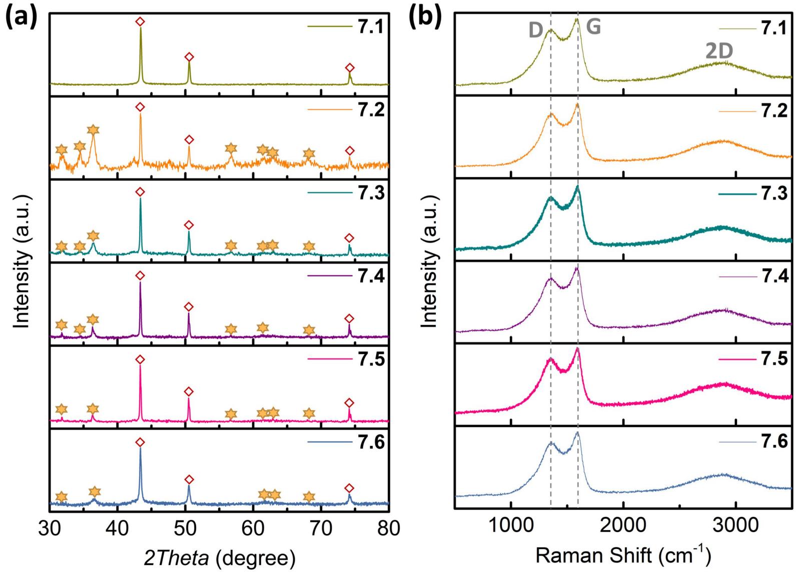

Figure 7.1. XRD patterns (**a**) and Raman spectra (**b**) of the samples **7.1**-**7.6**. Symbols: Cu (◇) and ZnO (✡).

High-resolution FESEM images at 100-400 nm scale recorded for the Cu-ZnO@(N)C materials reveal a fluffy, poorly packed, and highly porous morphology of the graphitic carbon acting as the matrix and support of the metal NPs. As commented in the Introduction, this porous structure is inherited from chitosan aerogel beads dried in supercritical CO_2 and corresponds to the graphitization of linear chitosan fibrils. **Figure 7.2** shows selected HR-FESEM images of Cu-ZnO@(N)C samples showing the structure of the carbonaceous matrix. As expected, no metal NPs could be observed in the HR-FESEM images in agreement with the nanometric particle size of Cu-ZnO NPs measured by TEM.

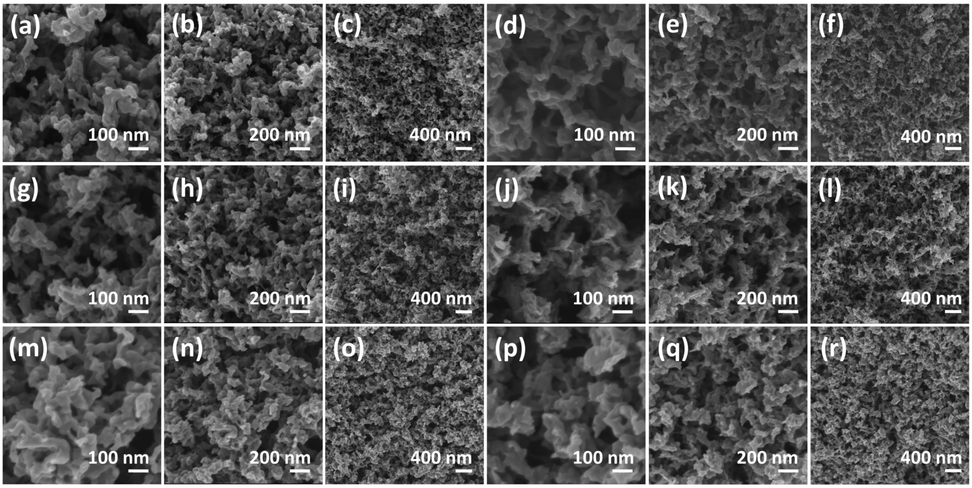

Figure 7.2. HR-FESEM images of samples **7.1**-**7.6**. (**a**, **b**, **c**: sample **7.1**; **d**, **e**, **f**: sample **7.2**; **g**, **h**, **i:** sample **7.3**; **j**, **k**, **l**: sample **7.4**; **m**, **n**, **o**: sample **7.5** and **p**, **q**, **r**: sample **7.6**.)

High-resolution TEM images show that the Cu-ZnO@(N)G samples are constituted by metal NPs deposited on 2D defective graphene. **Figure 7.3** shows the selected DF-TEM images taken in three different areas for the Cu-ZnO@(N)G samples, illustrating that the metal NPs are homogeneously distributed through the carbon matrix. The particle size distribution and the average size were determined by measuring a statistically significant number of those metal NPs. These similar values of average particle size for the series of samples ranging from 1.0±0.2 to 1.4±0.4 nm are collected in **Table 7.1**, while the corresponding particle size distribution histograms are inserted in the DF-TEM images presented in **Figure 7.3**. These small dimensions suggest the occurrence of a strong interaction of the Cu NPs with the defective N-doped graphitic carbon that thwarts the growth of particle even during pyrolysis at 900 ^{o}C.

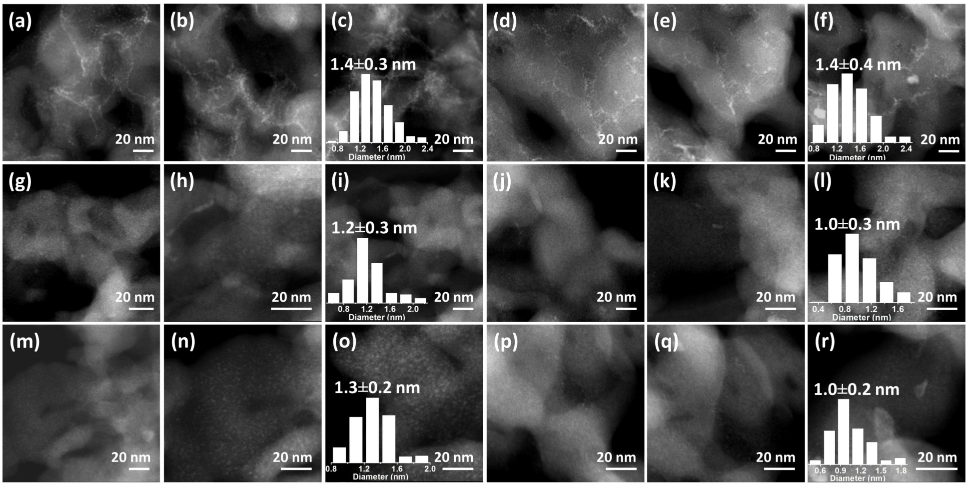

Figure 7.3. DF-TEM images of samples **7.1**-**7.6**. (**a**, **b**, **c**: sample **7.1**; **d**, **e**, **f**: sample **7.2**; **g**, **h**, **i:** sample **7.3**; **j**, **k**, **l**: sample **7.4**; **m**, **n**, **o**: sample **7.5** and **p**, **q**, **r**: sample **7.6**.

Inset: statistical particle size distribution of samples **7.1**-**7.6** according to the main frame image.)

7.2.2 Catalytic activity

As commented in the Introduction, the purpose of selecting Cu and ZnO in the composition of the samples was to measure the materials as catalysts for the selective partial hydrogenation of CO_2 to methanol. The catalytic reactions were carried out in a pressurized stainless-steel reactor, operating at 40 bar, using a H_2/CO_2 ratio of 4 and a continuous flow of 0.8 mL CO_2 per min. After considering the thermodynamic limitations as previously commented, the range of temperatures studied was between 150 to 300 ^{o}C in 50 ^{o}C increments. Previous control tests operating at 300 ^{o}C in the absence of catalyst showed no CO_2 conversions and the absence of methanol or any other products.

Analysis of the reaction products of samples under study shows that methanol was formed together with CO and methane (See **Tables 8.4.5.1** to **8.4.5.1.3** in **CHAPTER 8**). In agreement with the thermodynamics, selectivity to methanol decreases with CO_2 conversion and reaction temperature.[21, 22] Higher temperatures result in higher CO_2 conversions but lower methanol selectivity, the unwanted CO being the major product.[23, 24] Regardless of the unsatisfactory results of the other samples, the maximum methanol selectivity of sample **7.5** was detected at 250 ^{o}C for CO_2 conversions of about 1.5 %, although below 1 % at 150 and 200 ^{o}C, reaching a remarkable selectivity towards methanol of about 64 % (see **Figure 7.4**). However,

CO_2 conversion increases significantly at 300 °C, close to the thermodynamics limit for the formation of methanol. In addition, sample **7.5** appears stable under the reaction conditions for one week. Moreover, cycles of increasing the temperature from 150 to 300 °C show quite similar catalytic result, as presented in **Figure 7.5**, again supporting catalyst stability.

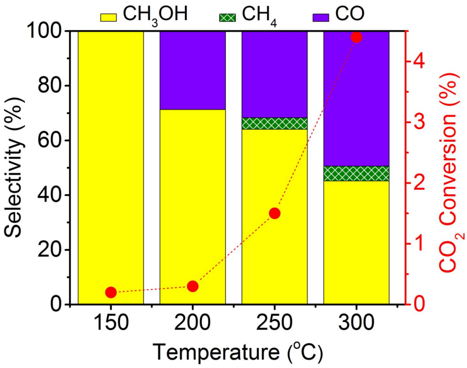

Figure 7.4. CO_2 conversion and selectivity for sample **7.5** at different temperature. Reaction conditions: H_2/CO_2 ratio of 4, total flow 4 mL/min, 40 bar, 40 mg catalyst.

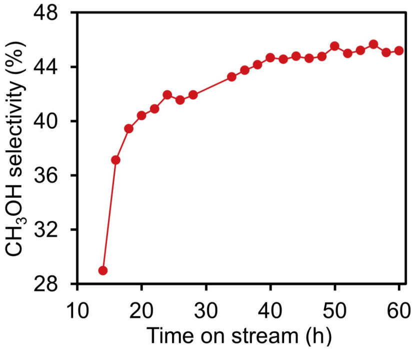

Figure 7.5. Stability test of samples **7.5** at 300 °C. Reaction conditions: H_2/CO_2 ratio of 4, total flow 4 mL/min, 40 bar, 40 mg catalyst.

7.3 Conclusions

Although Zn metal undergoes evaporation during high-temperature pyrolysis, it has been possible to prepare a series of Cu-ZnO@(N)C catalysts by pyrolysis of chitosan embedding $Cu(OAc)_2$ and a subsequent incorporation of $Zn(OAc)_2$ on preformed Cu@(N)C. The samples under study show very small metal NPs about 1 nm average size well dispersed on the graphitic matrix. These samples act as catalysts for the partial CO_2 hydrogenation to methanol. However, the formation of CO and methane in considerable proportions was observed during the process. Methanol selectivity decreased with CO_2 conversion and largely depended on the Cu-ZnO@(N)C catalysts, reaching a maximum methanol value of about 64 % for about 1.5 % CO_2 conversion. The catalytic results achieved represent the starting point for an optimization study trying to reach higher methanol selectivity at lower reaction temperatures.

References

[1] M. Garside, Global production capacity of methanol 2018-2030, **(2020)**. Available at:https://www.statista.com/statistics/1065891/global-methanol-production-capacity/.

[2] X. Xu, X. Zhang, Z. Xia, R. Sun, J. Wang, Q. Jiang, S. Yu, S. Wang, G. Sun, Fe-N-C with Intensified Exposure of Active Sites for Highly Efficient and Stable Direct Methanol Fuel Cells, *ACS Appl. Mater. Interfaces*, 14 **(2021)** 16279-16288.

[3] J. Zhong, J. Han, Y. Wei, Z. Liu, Catalysts and shape selective catalysis in the methanol-to-olefin (MTO) reaction, *J. Catal.*, 396 **(2021)** 23-31.

[4] L. Yuan, C. Wang, R. Cai, Y. Wang, G. Zhou, Temperature-dependent growth mechanism and microstructure of ZnO nanostructures grown from the thermal oxidation of zinc, *J. Cryst. Growth*, 390 **(2014)** 101-108.

[5] V. Deerattrakul, N. Yigit, G. Rupprechter, P. Kongkachuichay, The roles of nitrogen species on graphene aerogel supported Cu-Zn as efficient catalysts for CO_2 hydrogenation to methanol, *Appl. Catal. A*, 580 **(2019)** 46-52.

[6] Y. Hartadi, D. Widmann, R.J. Behm, Methanol formation by CO_2 hydrogenation on Au/ZnO catalysts-effect of total pressure and influence of CO on the reaction characteristics, *J. Catal.*, 333 **(2016)** 238-250.

[7] D.H. Lim, J.H. Jo, D.Y. Shin, J. Wilcox, H.C. Ham, S.W. Nam, Carbon dioxide conversion into hydrocarbon fuels on defective graphene-supported Cu nanoparticles from first principles, *Nanoscale*, 6 **(2014)** 5087-5092.

[8] D. García-Rodríguez, L. Mendoza-Huizar, C. Díaz, A DFT study of Cu nanoparticles adsorbed on defective graphene, *Appl. Surf. Sci.*, 412 **(2017)** 146-151.

[9] Z. Ma, C. Tsounis, P.V. Kumar, Z. Han, R.J. Wong, C.Y. Toe, S. Zhou, N.M. Bedford, L. Thomsen, Y.H. Ng, Enhanced electrochemical CO_2 reduction of Cu@CuxO nanoparticles decorated on 3D vertical graphene with intrinsic sp^3-type defect, *Adv. Funct. Mater.*, 30 **(2020)** 1910118.

[10] Y. Zhao, Z. Horita, T. Langdon, Y. Zhu, E. A, Evolution of defect structures during cold rolling of ultrafine-grained Cu and Cu-Zn alloys: Influence of stacking fault energy, *Mater. Sci. Eng. A*, 474 **(2008)** 342-347.

[11] J. He, K.E. Dettelbach, A. Huang, C.P. Berlinguette, Brass and bronze as effective CO_2 reduction electrocatalysts, *Angew. Chem.*, 129 **(2017)** 16806-16809.

[12] B.A. Peppley, J.C. Amphlett, L.M. Kearns, R.F. Mann, Methanol-steam reforming on $Cu/ZnO/Al_2O_3$. Part 1: the reaction network, *Appl. Catal. A*, 179 **(1999)** 21-29.

[13] M. Zabilskiy, V.L. Sushkevich, D. Palagin, M.A. Newton, F. Krumeich, J.A. van Bokhoven, The unique interplay between copper and zinc during catalytic carbon dioxide hydrogenation to methanol, *Nat. Commun.*, 11 **(2020)** 1-8.

[14] M.M. Günter, T. Ressler, B. Bems, C. Büscher, T. Genger, O. Hinrichsen, M. Muhler, R. Schlögl, Implication of the microstructure of binary Cu/ZnO catalysts for their catalytic activity in methanol synthesis, *Catal. Letters*, 71 **(2001)** 37-44.

[15] T.M. Yurieva, L.M. Plyasova, V.I. Zaikovskii, T.P. Minyukova, A. Bliek, J.C. van den Heuvel, L.P. Davydova, I.Y. Molina, M.P. Demeshkina, A.A. Khassin, *In situ* XRD and HRTEM studies on the evolution of the Cu/ZnO methanol synthesis catalyst during its reduction and re-oxidation, *Phys. Chem. Chem. Phys.*,6 **(2004)** 4522-4526.

[16] O. Frank, M. Mohr, J. Maultzsch, C. Thomsen, I. Riaz, R. Jalil, K.S. Novoselov, G. Tsoukleri, J. Parthenios, K. Papagelis, Raman 2D-band splitting in graphene: theory and experiment, *ACS nano*, 5 **(2011)** 2231-2239.

[17] J. Hong, M.K. Park, E.J. Lee, D. Lee, D.S. Hwang, S. Ryu, Origin of new broad Raman D and G peaks in annealed graphene, *Sci. Rep.*, 3 **(2013)** 1-5.

[18] A. Primo, P. Atienzar, E. Sanchez, J.M. Delgado, H. García, From biomass wastes to large-area, high-quality, N-doped graphene: catalyst-free carbonization of chitosan coatings on arbitrary substrates, *Chem. Comm.*, 48 **(2012)** 9254-9256.

[19] C. Lavorato, A. Primo, R. Molinari, H. Garcia, N-doped graphene derived from biomass as a visible-light photocatalyst for hydrogen generation from

water/methanol mixtures, *Chem. Eur. J.*, 20 **(2014)** 187-194.

[20] A. Primo, E. Sánchez, J.M. Delgado, H. García, High-yield production of N-doped graphitic platelets by aqueous exfoliation of pyrolyzed chitosan, *Carbon*, 68 **(2014)** 777-783.

[21] G. Prieto, Carbon dioxide hydrogenation into higher hydrocarbons and oxygenates: Thermodynamic and kinetic bounds and progress with heterogeneous and homogeneous catalysis, *ChemSusChem*, 10 **(2017)** 1056-1070.

[22] V. Dieterich, A. Buttler, A. Hanel, H. Spliethoff, S. Fendt, Power-to-liquid via synthesis of methanol, DME or Fischer–Tropsch-fuels: a review, *Energy Environ. Sci.*, 13 **(2020)** 3207-3252.

[23] K. Klier, V. Chatikavanij, R. Herman, G. Simmons, Catalytic synthesis of methanol from COH_2: IV. The effects of carbon dioxide, *J. Catal.*, 74 **(1982)** 343-360.

[24] X. Yang, S. Kattel, S.D. Senanayake, J.A. Boscoboinik, X. Nie, J.s. Graciani, J.A. Rodriguez, P. Liu, D.J. Stacchiola, J.G. Chen, Low pressure CO_2 hydrogenation to methanol over gold nanoparticles activated on a CeO_x/TiO_2 interface, *J. Am. Chem. Soc.*, 137 **(2015)** 10104-10107.

CHAPTER 8

Experimental Section

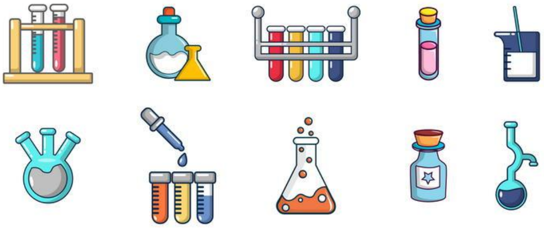

CHAPTER 8

CHAPTER 8

8.1 General Procedures

Commercially available reagents were purchased from Aldrich and used without further purification.

8.1.1 Synthesis of samples Co@(N)C, Co-Fe@(N)C and Co-Fe@TiO_2 prepared in CHAPTER 3

Co@(N)C (sample **3.1**) and Co-Fe@(N)C (samples **3.2**-**3.5**) were prepared by two different methods.

Samples **3.1**-**3.3** were prepared by co-precipitation method. Briefly, 1000 mg chitosan, 625 µL acetic acid and certain amount of $Co(OAc)_2$ and $Fe(OAc)_2$ were added into 50 mL milli-Q water. After chitosan dissolved completely, the solution was introduced dropwise, with a syringe (0.8 mm diameter needle), in an aqueous solution of sodium hydroxide (0.1M). The gel microspheres were formed immediately after dropping and immersed in NaOH solution for 2 h, then profusely washed with distilled water to pH=7. Then the resulting hydrogel microspheres were washed by a series of ethanol/water baths with an increasing concentration of ethanol (10, 30, 50, 70, 90 and 100 vol.%, respectively) for 15 min in each. After that, the microspheres were reduced overnight with 500 mL $NaBH_4$-ethanol solution (0.05 M) for and dried with supercritical CO_2. The resulting microspheres were pyrolyzed under Ar flow (200 mL/min), increasing the temperature at a rate of 2 ^{o}C/min up to 200 ^{o}C for 2 h and then to 900 ^{o}C for 2 h.

Samples **3.4** and **3.5** were prepared by impregnation of chitosan beads in ethanol solution with iron and cobalt salts. Briefly, 1000 mg chitosan and 625 µL acetic acid were added into 50 mL milli-Q water. After chitosan dissolved completely, the solution was introduced dropwise, with a syringe (0.8 mm diameter needle), in an aqueous solution of sodium hydroxide (2 M). The gel microspheres were formed and immersed in NaOH solution for 2 h, then profusely washed with distilled water to pH=7. Then the resulting hydrogel microspheres were washed by a series of ethanol/water baths with an increasing concentration of ethanol (10, 30, 50, 70, 90, 100 vol.%, respectively) for 15 min in each and immersed in 100 mL Co-Fe-ethanol solution with different concentration for 2 days with a slow stirring. After that, the microspheres were reduced with 375 mL $NaBH_4$-ethanol solution with different concentration for a while and then exchanged by supercritical CO_2. The resulting microspheres were pyrolyzed under Ar flow (200 mL/min), increasing the temperature at a rate of 2 °C/min up to 200 °C for 2 h and then to 900 °C for 2 h.

Table 8.1.1. List of metal sources used in the preparation of Co@(N)C (sample **3.1**) and Co-Fe@(N)C (samples **3.2**-**3.5**) in **CHAPTER 3**.

Samples No.	Metal source	m (mg)
3.1	$Co(OAc)_2$	75
3.2	$Co(OAc)_2$	240
	$Fe(OAc)_3$	100
3.3	$Co(OAc)_2$	240
	$Fe(OAc)_2$	100

3.4	$Co(OAc)_2$	240
	$Fe(OAc)_2$	100
3.5	$CoCl_2$	150
	$FeCl_2$	75

Co-Fe@TiO_2: Briefly, to obtain 10 wt.% Co and 5 wt.% Fe in the final Co-Fe@TiO_2 catalyst, the required amounts of $Co(OAc)_2$ and $Fe(OAc)_2$ dissolved in an aqueous solution indicated in **Table 8.1.1**, was impregnated on to the TiO_2 support. After impregnation, the sample was dried at 120 ^oC for 12 h followed by heat treated in Ar with a heating rate of 2 ^oC/min at 400 ^oC for 4 h. Then, the material prepared was reduced by H_2 with a heating rate of 5 ^oC/min at 600 ^oC for 2 h.

8.1.2 Synthesis of samples Co-Fe@(N)C, Co@(N)C, Fe@(N)C, Co-Fe@C and Co-Fe@SiO_2 prepared in CHAPTER 4

Co@(N)C, Fe@(N)C and Co-Fe@(N)C were prepared by impregnation of chitosan beads in 50 vol.% ethanol aqueous solution with iron and cobalt salts. Briefly, 400 mg chitosan and 250 µL acetic acid were added into 20 mL milli-Q water. After chitosan dissolved completely, the solution was introduced dropwise, with a syringe (0.8 mm diameter needle), in an aqueous solution of sodium hydroxide (2 M). The gel microspheres were formed immediately after dropping and immersed in NaOH solution for 2 h, then, profusely washed with distilled water to pH=7. The resulting hydrogel microspheres were washed by a series of ethanol/water baths with an increasing concentration of ethanol (10, 30, 50 vol.%, respectively) for 15 min in each and immersed in 40 mL 50 vol.% ethanol aqueous solution with different amounts of iron and cobalt salts for 2 days with a slow stirring. The exact salts and amounts are indicated in **Table 8.1.2**. After that, the microspheres were dehydrated by a series of ethanol/water baths with an increasing concentration of ethanol (70, 90 and 100 vol.%, respectively) for 15 min in each and exchanged by supercritical CO_2. The resulting dry microspheres were pyrolyzed under Ar flow (200 mL/min), increasing the temperature at a rate of 2 ^oC/min up to 200 ^oC for 2 h and then to 900 ^oC for 2 h.

Co-Fe@C was prepared analogously, but starting from an alginic solution that was dropped into an aqueous metal salt solution containing 0.5 M of $CaCl_2$. The gel microspheres were formed immediately after dropping and immersed in the metal salt solution for 2 h, then washed by a series of ethanol/water baths with an increasing concentration of ethanol (10, 30, 50, 70, 90 and 100 vol.%, respectively) for 15 min in each and finally dried by supercritical CO_2. The resulting aerogel microspheres were pyrolyzed under Ar flow (200 mL/min), increasing the temperature at a rate of 2 ^oC/min up to 200 ^oC for 2 h and then to 900 ^oC for 2 h.

Co-Fe@SiO_2: Briefly, to obtain 10 wt.% Co and 5 wt.% Fe in the final Co-Fe@SiO_2 catalyst, the required amount of $Co(OAc)_2$ and $Fe(OAc)_2$ dissolved in an aqueous solution indicated in **Table 8.1.2**, were impregnated to SiO_2 [(Davisil Grade 646), 35-60 mesh, pore size 150 Å] support. After impregnation, the sample was dried at 120 ^oC for 12 h followed by calcined in air with a heating rate of 2 ^oC/min at 400 ^oC

for 4 h. Then, the material prepared was reduced by H_2 with a heating rate of 5 °C/min at 600 °C for 2 h.

Table 8.1.2. List of weights of metal sources used in the preparation of Co-Fe@(N)C (samples **4.1**-**4.3** and **4.6-4.8**), Co@(N)C (samples **4.4** and **4.9**), Fe@(N)C (samples **4.5** and **4.8**), Co-Fe@C (sample **4.11**) and Co-Fe@SiO_2 (**sample 4.12**) in **CHAPTER 4**.

Samples No.	$m_{Co(OAc)2}$ (mg)	$m_{Fe(OAc)2}$ (mg)	C_{Co} (mol/L)	C_{Fe} (mol/L)
4.1	5	5	-	-
4.2	10	5	-	-
4.3	15	5	-	-
4.4	5	-	-	-
4.5		5	-	-
4.6	-	-	0.01	0.01
4.7	-	-	0.01	0.008
4.8	-	-	0.01	0.003
4.9	-	-	0.01	-
4.10	-	-	-	0.01
4.11	240	100	-	-
4.12	150	75	-	-

8.1.3 Synthesis of the Co-Fe@(N)C samples prepared in CHAPTER 5

Co-Fe@(N)C (samples **5.1**-**5.5**): Briefly, 400 mg chitosan and 250 µL acetic acid were added into 20 mL milli-Q water. After chitosan dissolved completely, the solution was introduced dropwise, with a syringe (0.8 mm diameter needle), in an aqueous solution of sodium hydroxide (2 M). The gel microspheres were formed and immersed in NaOH solution for 2 h, then, profusely washed with distilled water to pH=7. The resulting hydrogel microspheres were washed by a series of ethanol/water baths with an increasing concentration of ethanol (10, 30, 50, 70, 90, 100 vol%, respectively) for 15 min in each and immersed in 40 mL $CoCl_2$-$FeCl_2$-ethanol solution with different concentration for 2 days with a slow stirring. The exact amounts of $CoCl_2$ and $FeCl_2$ employed for each sample are indicated in **Table 8.1.3**. After that, the microspheres were reduction with 150 mL $NaBH_4$ in ethanol solution with different concentrations for a while as indicated in **Table 8.1.3** and then exchanged by supercritical CO_2. The resulting microspheres were pyrolyzed under Ar flow (200 mL/min), increasing the temperature at a rate of 2 ^oC/min up to 200 ^oC for 2 h and then to 900 ^oC for 2 h.

Table 8.1.3. List of Co-Fe@(N)C (samples **5.1**-**5.5**) under study in **CHAPTER 5**.

Samples No.	C_{Co} (mol/L)	C_{Fe} (mol/L)	C_{NaBH4} (mol/L)	Time (h)
5.1	0.001×0.79/0.21	0.001	0.05	5
5.2	0.002×0.79/0.21	0.002	0.05	5
5.3	0.003×0.79/0.21	0.003	0.05	5
5.4	0.003×0.79/0.21	0.003	0.05	12
5.5	0.003×0.79/0.21	0.002	0.1	5

8.1.4 Synthesis of samples Co-Fe@(N)C and Co-Fe@C prepared in CHAPTER 6

The samples were prepared following three routes. Route **a**: Samples **6.1** and **6.2** were prepared following route **a**. Briefly, 1000 mg chitosan and 625 µL acetic acid were added into 50 mL milli-Q water. After chitosan dissolved completely, the solution was introduced dropwise, with a syringe (0.8 mm diameter needle), in an aqueous solution of sodium hydroxide (500 mL, 2 M). The gel microspheres were formed immediately and immersed in NaOH solution for 2 h, then profusely washed with distilled water to pH=7. Afterwards, the resulting hydrogel microspheres were washed by a series of ethanol/water baths with an increasing concentration of ethanol (10, 30, 50, 70, 90, 100 vol.%, respectively) for 15 min in each and immersed in 100 mL Co-Fe-ethanol or Co-Fe-Pd-ethanol solution with different concentration for 2 days with a slow stirring. The exact amounts of each salt employed are indicated in **Table 8.1.4**. After that, the microspheres were reduced with 375 mL 0.05 M $NaBH_4$-ethanol solution for 5 h and then dried by supercritical CO_2. The resulting microspheres were pyrolyzed under Ar flow (200 mL/min), increasing the temperature at a rate of 2 ^oC/min up to 200 ^oC for 2 h and then to 900 ^oC for 2 h. Preparation of samples **6.8**-**6.11** was performed following route **a** with an additional thiourea impregnation step in 375 mL EtOH after $NaBH_4$ reduction and before steps of supercritical CO_2 drying and pyrolysis.

Route **b**: Samples **6.3** and **6.4** were prepared following route **b**. Briefly, 1000 mg chitosan, 625 µL acetic acid and certain amount of $Co(OAc)_2$ and $Fe(OAc)_2$ or hydrated $Ce(OAc)_3$ were added into 50 mL milli-Q water. After chitosan dissolved completely, the solution was introduced dropwise, with a syringe (0.8 mm diameter needle), in an aqueous solution of sodium hydroxide (500 mL, 0.1 M). The gel microspheres were formed immediately after dropping and immersed in NaOH solution for 1 h, then profusely washed with distilled water to pH=7. The resulting hydrogel microspheres were washed by a series of ethanol/water baths with an increasing concentration of ethanol (10, 30, 50, 70, 90 and 100 vol.%, respectively) for 15 minu in each. After that, the microspheres were reduced with 500 mL $NaBH_4$-ethanol solution (0.05M) for overnight and exchanged by supercritical CO_2. The resulting microspheres were pyrolyzed under Ar flow (200 mL/min), increasing the temperature at a rate of 2 ^oC/min up to 200 ^oC for 2 h and then to 900 ^oC for 2 h.

Route **c**: Samples **6.5**-**6.7** were prepared following route **c**. In this procedure, 1000 mg sodium alginate were added into 50 mL milli-Q water. After sodium alginate dissolved completely, the solution was introduced dropwise, with a syringe (0.8 mm diameter needle), in 100 mL an aqueous solution of $CoCl_2{\cdot}6H_2O$ and $FeCl_2$ or hydrated $Ce(OAc)_3$. The exact amounts of each salt employed are indicated in **Table 8.1.4**. The gel microspheres were formed immediately and equilibrated by stirring the mixture overnight. Then the resulting hydrogel microspheres were washed by a series of ethanol/water baths with an increasing concentration of ethanol (10, 30, 50, 70, 90 and 100 vol.%, respectively) for 15 min in each and subsequently dried by supercritical CO_2. Unlike samples **6.5** and **6.7**, sample **6.6** was prepared precipitating alginate acid aqueous solution (30 mL; 2 g alginic acid; 2.5 mL 25 wt.% ammonia solution) into $CaCl_2$ aqueous solution (4 g, 100 mL), then profusely washed with distilled water. Afterwards, the resulting hydrogel microspheres were washed by a series of ethanol/water baths with an increasing concentration of ethanol (10, 30, 50, 70, 90 and 100 vol.%, respectively) for 15 min in each. The resulting alcogel microspheres were immersed in Fe-Co-ethanol solution for 1 day, then washed with anhydrous ethanol and dried by supercritical CO_2. The resulting aerogel microspheres were pyrolyzed under Ar flow (200 mL/min), increasing the temperature at a rate of 2 ^oC/min up to 200 ^oC for 2 h and then to 900 ^oC for 2 h.

Table 8.1.4. List of metal sources and weights used in the preparation of samples **6.1**-**6.11** in **CHAPTER 6**.

Sample No.	Metal source	m (mg)	Promoter
6.1	$CoCl_2$	146.5	-
	$FeCl_2$	38.9	
6.2	$CoCl_2$	146.5	$PdCl_2$ (5 mg)
	$FeCl_2$	38.9	
6.3	$Co(OAc)_2$	150	-
	$Fe(OAc)_2$	50	
6.4	$Co(OAc)_2$	150	$Ce(OAc)_3 \cdot xH_2O$ (10 mg)
	$Fe(OAc)_2$	50	
6.5	$CoCl_2 \cdot 6H_2O$	150	-
	$FeCl_2$	75	
6.6	$Co(OAc)_2$	240	-
	$Fe(OAc)_2$	100	

6.7	$CoCl_2 \cdot 6H_2O$	951.7	$Ce(OAc)_3 \cdot xH_2O$ (126.9 mg)
	$FeCl_2$	101.4	
6.8	$CoCl_2$	146.5	Thiourea (20 mg/mL)
	$FeCl_2$	38.9	
6.9	$CoCl_2$	146.5	Thiourea (5 mg/mL)
	$FeCl_2$	38.9	
6.10	$CoCl_2$	146.5	Thiourea (2 mg/mL)
	$FeCl_2$	38.9	
6.11	$Co(OAc)_2$	40	NaOAc(8 mg) KOAc (4 mg) Thiourea (2 mg/mL)
	$Fe(OAc)_2$	16.5	

8.1.5 Synthesis of samples Cu@(N)C and Cu-ZnO@C prepared in CHAPTER 7

Cu@(N)C (Sample **7.1**) and Cu-ZnO@C (samples **7.2**-**7.6**) were obtained by dissolving 1000 mg chitosan with 625 µL acetic acid in 50 mL milli-Q water. After chitosan dissolved completely, the solution was introduced dropwise, with a syringe (0.8 mm diameter needle), in an aqueous solution of sodium hydroxide (500 mL; 2 M). The hydrogel microspheres were formed immediately and immersed in NaOH solution for 2 h and then profusely washed with distilled water to pH=7. Afterwards, the resulting hydrogel microspheres were washed by a series of ethanol/water baths with an increasing concentration of ethanol (10, 30, 50, 70, 90, 100 vol.%, respectively) for 15 min in each and immersed in 100 mL Cu-ethanol solution with different concentrations as indicated in **Table 8.1.5** for 2 days with a slow stirring, then washed with anhydrous ethanol and subsequently dried by supercritical CO_2. The resulting aerogel microspheres were pyrolyzed under Ar flow (200 mL/min), increasing the temperature at a rate of 2 ^oC/min up to 200 ^oC for 2 h and then to 900 ^oC for 2 h. The resulting Cu@(N)C was ground into powder and immersed in 30 mL Zn-ethanol solution with different concentration for 2 days with a slow stirring. After removal of ethanol at 60 ^oC overnight, the Zn^{2+}-containing Cu@(N)C was heated at a rate of 2 ^oC/min up to 200 ^oC for 2 h to obtain the final of Cu-ZnO@C.

Table 8.1.5. List of metal amounts employed in the preparation of Cu@(N)C (Samples **7.1**) and Cu-ZnO@C (samples **7.2**-**7.6**) under study in **CHAPTER 7**.

Samples No.	$C_{Cu(OAc)2}$ (mol/L)	$m_{Zn(OAc)2}$ (mg)
7.1	0.005	-
7.2	0.005	109.8
7.3	0.005	43.9
7.4	0.005	22.0
7.5	0.005	27.3
7.6	0.005	11.0

8.2 Sample Characterization

X-ray diffraction patterns were obtained in a Philips XPert diffractometer (40 kV and 45 mA) equipped with a graphite monochromator employing Ni-filtered Cu Kα radiation (1.541178 Å). Raman spectra were collected with a Horiba Jobin Yvon-Labram HR UV-visible-NIR (200-1600 nm). Raman microscope spectrometer model, resolution using a 514 nm laser. The carbon and nitrogen content of the samples was determined by combustion chemical analysis by using a CHNS FISONS elemental analyzer. The chemical analysis was determined by ICP-OES (iCAP 7400, Thermo Scientific, Waltham, MA, USA). Field emission scanning electron microscopy images were acquired by using a JEOL JSM 6300 apparatus. High resolution transmission electron microscope images were recorded in a JEOL JEM 2100F under an accelerating voltage of 200 kV coupled with an X-Max 80 energy dispersive X-ray detector (Oxford instruments). This HR-TEM is equipped with the dark-field and high-angle field image detectors that facilitate the observation of phase contrast with different atomic number. Samples for measurement were prepared by dropping few drops of the suspended material in ethanol or dichloromethane on a carbon-coated nickel or copper grid and drying at room temperature overnight.

8.3 Catalytic Tests

Catalytic tests were performed in collaboration with the group of Prof. Vasile I. Parvulescu at the University of Bucharest. A setup (Microactivity tester, PID Eng&Tech) equipped with a stainless steel (316 SS) fixed bed tube reactor (Autoclave Engineers) featured with an inner K-type thermocouple was used. Two mass flow controllers (EL-FLOW Select, Bronkhorst) were used to feed the mixture of the inlet gases: hydrogen (5.0, Linde) and carbon dioxide (4.5, Linde). The total gas flow rate was checked before each experiment using a gas calibrated burette connected to the outlet of the reactor setup. After catalyst activation at 300 °C under N_2, an amount of 40 mg catalyst powder was introduced in the reactor. Air was removed by flushing the system at room temperature for 15 min with 30 mL/min H_2 and 10 mL/min CO_2, followed by 30 min catalytic reaction at the flow rates of different ratio of H_2 and CO_2 (in total 4 mL/min). Afterwards, the reactor was pressurized at 10 or 20 or 40 bar depending on different reactions. Each sample was submitted to a 5 h test starting at 250 °C and increasing the temperature in 50 °C steps. Each temperature was maintained for 1 h period before increasing another 50 °C. Analysis of the reaction products was carried out on line with multichannel gas chromatography that quantifies the percentage of CO_2, CO, CH_4 and C_{2+} products. Data at each temperature corresponds to the average value of the analysis measured for each temperature at 30, 45 and 55 min after the stabilization of the temperature. The values of the CO_2 conversion obtained from the GC measurements coincided very well in all the experiments, indicating that the reactor setup reached the steady state operation conditions.

GC analyses were performed using H_2 as carrier gas on an Agilent 7890A chromatograph equipped with a capillary PLOT column (RT-Msieve 5A, Restek) and a thermal conductivity detector (TCD). Oven temperature program started with a 5 min dwell at 50 °C, then continue with a ramp with 25 °C/min up to 250 °C followed by a final dwell of 5 min, allowing thus a very good separation between CH_4, CO and CO_2. The gas samples were injected through a remotely controlled 6-way valve (A4C6WE, Vici) kept at ambient temperature. The reproducibility of the analysis system was checked prior to each experiment by injecting a series of three successive samples of standard gas mixtures of known composition passed through the reactor at room temperature.

8.4 Tables of Catalytic Activity and Selectivity

8.4.1 Tables of catalytic activity and selectivity for methane in CHAPTER 3

Table 8.4.1.1. CO_2 conversion and selectivity for sample **3.1** at different temperatures. (Reaction conditions: H_2/CO_2 ratio of 7, total flow 4 mL/min, 10 bar, 40 mg catalyst.)

T (°C)	**C (%) CO_2**	**S (%) CH_4**	S (%) C_2H_6	S (%) C_3H_8	S (%) *n*-C_4H_{10}	S (%) C_2H_4	S (%) C_3H_6	S (%) CO
400	**30.2**	**77.1**	0.3	0.2	0	0	0	22.4
450	**50.8**	**81.0**	0.2	0	0	0	0	18.8
500	**67.4**	**86.2**	0.3	0	0	0	0	13.5

Table 8.4.1.2. CO_2 conversion and selectivity for sample **3.2** at different temperatures. (Reaction conditions: H_2/CO_2 ratio of 7, total flow 4 mL/min, 10 bar, 40 mg catalyst.)

T (°C)	**C (%) CO_2**	**S (%) CH_4**	S (%) C_2H_6	S (%) C_3H_8	S (%) *n*-C_4H_{10}	S (%) C_2H_4	S (%) C_3H_6	S (%) CO
400	**55.9**	**84.6**	3.4	1.2	1.0	0	0	9.9

450	**72.0**	**90.9**	2.1	0.2	0	0	0	6.8
500	**80.4**	**92.6**	1.0	0.1	0	0	0	6.3

Table 8.4.1.3. CO_2 conversion and selectivity for sample **3.3** at different temperatures. (Reaction conditions: H_2/CO_2 ratio of 7, total flow 4 mL/min, 10 bar, 40 mg catalyst.)

T (°C)	**C (%) CO_2**	**S (%) CH_4**	S (%) C_2H_6	S (%) C_3H_8	S (%) n-C_4H_{10}	S (%) C_2H_4	S (%) C_3H_6	S (%) CO
300	**8.2**	**65.6**	0.7	0	0	0	0	33.7
350	**28.8**	**61.9**	3.8	1.6	1.6	0	0.9	30.3
400	**64.4**	**64.2**	11.4	5.3	3.4	0.8	2.1	12.8
450	**77.0**	**80.3**	6.3	1.3	0.4	0.2	0.3	11.2
500	**82.4**	**86.0**	2.2	0.2	0	0	0	11.6

Table 8.4.1.4. CO_2 conversion and selectivity for sample **3.4** at different temperatures. (Reaction conditions: H_2/CO_2 ratio of 7, total flow 4 mL/min, 10 bar, 40 mg catalyst.)

T (°C)	**C (%) CO_2**	**S (%) CH_4**	S (%) C_2H_6	S (%) C_3H_8	S (%) n-C_4H_{10}	S (%) C_2H_4	S (%) C_3H_6	S (%) CO
300	**14.9**	**70.1**	2.0	0	0	0	0.9	26.9
350	**35.5**	**62.8**	5.0	1.8	1.5	0	1.3	27.6
400	**67.8**	**69.3**	9.0	4.6	2.1	1.1	2.2	11.6

450	**81.3**	**87.0**	3.6	0.7	0.3	0.3	0.2	8.0
500	**87.1**	**91.2**	1.3	0.2	0	0	0	7.3

Table 8.4.1.5. CO_2 conversion and selectivity for sample **3.5** at different temperatures. (Reaction conditions: H_2/CO_2 ratio of 7, total flow 4 mL/min, 10 bar, 40 mg catalyst.)

T (°C)	**C (%) CO_2**	**S (%) CH_4**	S (%) C_2H_6	S (%) C_3H_8	S (%) n-C_4H_{10}	S (%) C_2H_4	S (%) C_3H_6	S (%) CO
300	**2.7**	**71.9**	4.9	0	0	0	0	23.1
350	**10.6**	**75.7**	0.8	0	0	0	0	23.6
400	**42.9**	**75.8**	4.1	1.6	1.0	0	0.5	17.1
450	**74.6**	**86.7**	3.8	0.7	0.3	0.1	0.1	8.2
500	**85.0**	**90.5**	1.7	0.2	0	0	0	7.6

Table 8.4.1.6. CO_2 conversion and selectivity for Co-Fe@TiO_2 at different temperatures. (Reaction conditions: H_2/CO_2 ratio of 7, total flow 4 mL/min, 10 bar, 40 mg catalyst.)

T (°C)	**C (%) CO_2**	**S (%) CH_4**	S (%) C_2H_6	S (%) C_3H_8	S (%) n-C_4H_{10}	S (%) C_2H_4	S (%) C_3H_6	S (%) CO
250	**0.3**	**16.1**	0	0	0	0	0	83.9
300	**0.7**	**11.8**	3.9	0	0	0	0	84.3
350	**4.5**	**6.4**	0.7	0	0	0	0	93.0

400	**16.1**	**6.1**	0.5	0	0	0	0	93.5
450	**29.8**	**6.5**	0.7	0	0	0	0	92.8

8.4.2 Tables of catalytic activity and selectivity for carbon monoxide in CHAPTER 4

Table 8.4.2.1. CO_2 conversion and selectivity for sample **4.1** at different temperatures. (Reaction conditions: H_2/CO_2 ratio of 7, total flow 4 mL/min, 10 bar, 40 mg catalyst.)

T (^{o}C)	**C (%) CO_2**	S (%) CH_4	S (%) C_2H_6	S (%) C_3H_8	S (%) n-C_4H_{10}	S (%) C_2H_4	S (%) C_3H_6	**S (%) CO**
300	**3.4**	2.0	4.5	0	0	0	7.3	**86.2**
350	**8.1**	1.6	2.8	0	0	0	0	**95.6**
400	**19.3**	1.0	0.8	0	0	0	0	**98.2**
450	**37.0**	1.0	0.4	0	0	0	0	**98.7**
500	**55.8**	1.6	0.5	0	0	0	0	**97.9**

Table 8.4.2.2. CO_2 conversion and selectivity for sample **4.2** at different temperatures. (Reaction conditions: H_2/CO_2 ratio of 7, total flow 4 mL/min, 10 bar, 40 mg catalyst.)

T (^{o}C)	**C (%) CO_2**	S (%) CH_4	S (%) C_2H_6	S (%) C_3H_8	S (%) n-C_4H_{10}	S (%) C_2H_4	S (%) C_3H_6	**S (%) CO**
300	**0.8**	8.0	6.5	0	0	0	0	**85.5**

350	**6.3**	1.9	1.1	0	0	0	0	**96.9**
400	**16.0**	1.3	0.5	0	0	0	0	**98.3**
450	**31.6**	2.4	1.1	0.5	0	0	0	**96.0**
500	**57.8**	15.8	7.2	2.6	0.7	0	0.4	74.3

Table 8.4.2.3. CO_2 conversion and selectivity for sample **4.3** at different temperatures. (Reaction conditions: H_2/CO_2 ratio of 7, total flow 4 mL/min, 10 bar, 40 mg catalyst.)

T (^{o}C)	**C (%) CO_2**	S (%) CH_4	S (%) C_2H_6	S (%) C_3H_8	S (%) n-C_4H_{10}	S (%) C_2H_4	S (%) C_3H_6	**S (%) CO**
300	**4.2**	2.2	4.6	0	0	0	4.0	**89.2**
350	**12.6**	1.1	1.7	0	0	0	0	**97.2**
400	**25.8**	1.0	0.9	0	0	0	0	**98.1**
450	**42.4**	1.4	0.6	0.2	0	0	0	**97.8**
500	**55.2**	7.1	3.0	0.8	0	0	0	**89.1**

Table 8.4.2.4. CO_2 conversion and selectivity for sample **4.4** at different temperatures. (Reaction conditions: H_2/CO_2 ratio of 7, total flow 4 mL/min, 10 bar, 40 mg catalyst.)

T (^{o}C)	**C (%) CO_2**	S (%) CH_4	S (%) C_2H_6	S (%) C_3H_8	S (%) n-C_4H_{10}	S (%) C_2H_4	S (%) C_3H_6	**S (%) CO**
300	**7.1**	11.5	3.8	0	0	0	0	**84.7**

350	**12.8**	7.0	1.4	0	0	0	3.5	**88.1**
400	**17.3**	2.9	0.9	0	0	0	0	**96.2**
450	**36.3**	1.6	0.6	0	0	0	0	**97.9**
500	**50.8**	1.9	0.4	0	0	0	0	**97.9**

Table 8.4.2.5. CO_2 conversion and selectivity for sample **4.5** at different temperatures. (Reaction conditions: H_2/CO_2 ratio of 7, total flow 4 mL/min, 10 bar, 40 mg catalyst.)

T (°C)	**C (%) CO_2**	S (%) CH_4	S (%) C_2H_6	S (%) C_3H_8	S (%) n-C_4H_{10}	S (%) C_2H_4	S (%) C_3H_6	**S (%) CO**
300	**1.0**	0	6.9	0	0	0	15.4	**77.7**
350	**3.7**	1.9	5.2	0	0	0	0	**92.9**
400	**11.9**	1.3	1.6	0	0	0	0	**97.2**
450	**28.6**	1.1	0.6	0	0	0	0	**98.2**
500	**46.6**	1.6	0.5	0	0	0	0	**97.9**

Table 8.4.2.6. CO_2 conversion and selectivity for sample **4.6** at different temperatures. (Reaction conditions: H_2/CO_2 ratio of 7, total flow 4 mL/min, 10 bar, 40 mg catalyst.)

T (°C)	**C (%) CO_2**	S (%) CH_4	S (%) C_2H_6	S (%) C_3H_8	S (%) n-C_4H_{10}	S (%) C_2H_4	S (%) C_3H_6	**S (%) CO**
400	**12.6**	13.4	1.3	0	0	0	0	**85.4**

450	**17.8**	1.7	0.5	0	0	0	0	**97.7**
500	**30.2**	6.6	1.7	0.2	0	0	0	**91.5**

Table 8.4.2.7. CO_2 conversion and selectivity for sample **4.7** at different temperatures. (Reaction conditions: H_2/CO_2 ratio of 7, total flow 4 mL/min, 10 bar, 40 mg catalyst.)

T (°C)	**C (%) CO_2**	S (%) CH_4	S (%) C_2H_6	S (%) C_3H_8	S (%) *n*-C_4H_{10}	S (%) C_2H_4	S (%) C_3H_6	**S (%) CO**
400	**3.9**	2.2	0.9	0	0	0	0	**96.9**
450	**8.2**	1.5	0.7	0	0	0	0	**97.9**
500	**14.7**	2.5	1.0	0	0	0	0	**96.5**

Table 8.4.2.8. CO_2 conversion and selectivity for sample **4.8** at different temperatures. (Reaction conditions: H_2/CO_2 ratio of 7, total flow 4 mL/min, 10 bar, 40 mg catalyst.)

T (°C)	**C (%) CO_2**	S (%) CH_4	S (%) C_2H_6	S (%) C_3H_8	S (%) *n*-C_4H_{10}	S (%) C_2H_4	S (%) C_3H_6	**S (%) CO**
400	**17.5**	9.7	2.0	1.0	0.8	0	0	**86.5**
450	**22.4**	1.8	0.6	0	0	0	0	**97.7**
500	**39.8**	12.5	3.5	1.1	0.4	0	0	**82.5**

Table 8.4.2.9. CO_2 conversion and selectivity for sample **4.9** at different

temperatures. (Reaction conditions: H_2/CO_2 ratio of 7, total flow 4 mL/min, 10 bar, 40 mg catalyst.)

T (°C)	**C (%) CO_2**	S (%) CH_4	S (%) C_2H_6	S (%) C_3H_8	S (%) *n*-C_4H_{10}	S (%) C_2H_4	S (%) C_3H_6	**S (%) CO**
250	**0.8**	45.8	5.0	0	0	0	0	**49.2**
300	**2.5**	33.3	2.4	0	0	0	0	**64.4**
350	**4.7**	18.7	0.9	0	0	0	0	**70.4**
400	**8.0**	9.3	0.6	0	0	0	0	**90.2**
450	**9.3**	4.9	0.6	0	0	0	0	**94.5**

Table 8.4.2.10. CO_2 conversion and selectivity for sample **4.10** at different temperatures. (Reaction conditions: H_2/CO_2 ratio of 7, total flow 4 mL/min, 10 bar, 40 mg catalyst.)

T (°C)	**C (%) CO_2**	S (%) CH_4	S (%) C_2H_6	S (%) C_3H_8	S (%) *n*-C_4H_{10}	S (%) C_2H_4	S (%) C_3H_6	**S (%) CO**
250	**0**	0	0	0	0	0	0	**100**
300	**0.4**	41.0	11.4	0	0	0	0	**47.6**
350	**1.7**	25.3	4.1	0	0	0	0	**70.6**
400	**6.4**	13.7	2.9	0	0	0	0	**83.4**
450	**9.7**	4.6	0.8	0	0	0	0	**94.6**

Table 8.4.2.11. CO_2 conversion and selectivity for sample **4.11** at different

temperatures. (Reaction conditions: H_2/CO_2 ratio of 7, total flow 4 mL/min, 10 bar, 40 mg catalyst.)

T (°C)	**C (%) CO_2**	S (%) CH_4	S (%) C_2H_6	S (%) C_3H_8	S (%) n-C_4H_{10}	S (%) C_2H_4	S (%) C_3H_6	**S (%) CO**
300	32.06	95.76	1.77	0.75	0	0	0	**1.71**
350	65.63	95.9	2.29	0.3	0	0	0	**1.51**
400	84.76	96.9	1.62	0.11	0	0	0	**1.36**
450	92.08	97.91	0.79	0.07	0	0	0	**1.22**
500	94.16	97.78	0.59	0.08	0	0	0	**1.54**

Table 8.4.2.12. CO_2 conversion and selectivity for sample **4.12** at different temperatures. (Reaction conditions: H_2/CO_2 ratio of 7, total flow 4 mL/min, 10 bar, 40 mg catalyst.)

T (°C)	**C (%) CO_2**	S (%) CH_4	S (%) C_2H_6	S (%) C_3H_8	S (%) n-C_4H_{10}	S (%) C_2H_4	S (%) C_3H_6	**S (%) CO**
250	**1.1**	23.7	5.9	30.5	0	0	14.9	**25.0**
300	**4.5**	60.1	3.4	4.1	0	0	0	**32.4**
350	**9.6**	59.8	4.8	1.5	0	0	0	**33.9**
400	**15.7**	60.8	4.7	1.0	0	0	0.7	**32.9**
450	**22.6**	61.9	4.8	0.5	0	0	0.4	**32.5**

8.4.3 Tables of catalytic activity and selectivity for C_2-C_4 hydrocarbons in CHAPTER

5

Table 8.4.3.1. CO_2 conversion and selectivity for sample **5.1** at different temperatures. (Reaction conditions: H_2/CO_2 ratio of 7, total flow 4 mL/min, 10 bar, 40 mg catalyst.)

T (°C)	**C (%)** **CO_2**	S (%) CH_4	S (%) C_2H_6	S (%) C_3H_8	S (%) n-C_4H_{10}	S (%) C_2H_4	S (%) C_3H_6	S (%) CO	**S (%)** **C_2-C_4^0**	**S (%)** **C_2-$C_4^=$**	**S (%)** **C_2-C_4**
300	**3.8**	67.0	1.6	0	0	0	4.0	27.3	**1.6**	**4.0**	**5.6**
350	**12.9**	70.2	2.3	0	0	0	1.2	26.2	**2.3**	**1.2**	**3.6**
400	**47.8**	64.4	10.8	5.9	3.0	0.3	1.0	14.6	**19.7**	**1.3**	**21.0**
450	**70.4**	64.5	13.0	5.8	1.4	0.4	0.7	14.2	**20.2**	**1.1**	**21.3**
500	**76.6**	74.2	7.0	1.1	0.2	0.1	0.2	17.2	**8.3**	**0.3**	**8.6**

Table 8.4.3.2. CO_2 conversion and selectivity for sample **5.2** at different temperatures. (Reaction conditions: H_2/CO_2 ratio of 7, total flow 4 mL/min, 10 bar, 40 mg catalyst.)

T (°C)	**C (%)** **CO_2**	S (%) CH_4	S (%) C_2H_6	S (%) C_3H_8	S (%) n-C_4H_{10}	S (%) C_2H_4	S (%) C_3H_6	S (%) CO	**S (%)** **C_2-C_4^0**	**S (%)** **C_2-$C_4^=$**	**S (%)** **C_2-C_4**
300	**6.7**	80.8	1.3	0	0	0	0	17.9	**1.3**	**0**	**1.3**
350	**21.2**	82.4	1.7	0	0	0	0	15.9	**1.7**	**0**	**1.7**
400	**62.3**	78.9	7.7	3.3	1.2	0.2	0.5	8.1	**12.3**	**0.7**	**13.0**
450	**79.4**	82.2	7.1	1.8	0.4	0.2	0.3	8.1	**9.2**	**0.4**	**9.7**
500	**82.4**	84.7	3.7	0.4	0	0.1	0	11.2	**4.1**	**0.1**	**4.2**

Table 8.4.3.3. CO_2 conversion and selectivity for sample **5.3** at different temperatures. (Reaction conditions: H_2/CO_2 ratio of 7, total flow 4 mL/min, 10 bar, 40 mg catalyst.)

T (°C)	**C (%) CO_2**	S (%) CH_4	S (%) C_2H_6	S (%) C_3H_8	S (%) *n*-C_4H_{10}	S (%) C_2H_4	S (%) C_3H_6	S (%) CO	**S (%) C_2-C_4^0**	**S (%) C_2-$C_4^=$**	**S (%) C_2-C_4**
300	**9.8**	81.3	1.3	0	0	0	0	17.4	**1.3**	**0**	**1.3**
350	**32.7**	76.1	4.4	1.6	1.4	0	0.5	16.0	**7.4**	**0.5**	**7.9**
400	**74.4**	68.4	11.9	7.4	3.5	0.6	1.4	6.9	**22.8**	**2.0**	**24.8**
450	**82.9**	83.0	6.9	1.8	0.6	0.3	0.3	7.2	**9.3**	**0.5**	**9.8**
500	**87.9**	91.4	2.1	0.2	0	0.1	0	6.3	**2.3**	**0.1**	**2.3**

Table 8.4.3.4. CO_2 conversion and selectivity for sample **5.4** at different temperatures. (Reaction conditions: H_2/CO_2 ratio of 7, total flow 4 mL/min, 10 bar, 40 mg catalyst.)

T (°C)	**C (%) CO_2**	S (%) CH_4	S (%) C_2H_6	S (%) C_3H_8	S (%) *n*-C_4H_{10}	S (%) C_2H_4	S (%) C_3H_6	S (%) CO	**S (%) C_2-C_4^0**	**S (%) C_2-$C_4^=$**	**S (%) C_2-C_4**
400	**71.6**	63.5	11.8	8.1	3.7	1.7	2.6	8.7	**23.6**	**4.2**	**27.8**
450	**75.0**	78.0	7.5	1.9	0.6	0.6	0.5	10.9	**10**	**1.1**	**11.1**
500	**75.1**	83.7	2.5	0.2	0.4	0.1	0.1	12.9	**3.2**	**0.2**	**3.4**

Table 8.4.3.5. CO_2 conversion and selectivity for sample **5.5** at different temperatures. (Reaction conditions: H_2/CO_2 ratio of 7, total flow 4 mL/min, 10 bar,

40 mg catalyst.)

T (°C)	**C (%) CO_2**	S (%) CH_4	S (%) C_2H_6	S (%) C_3H_8	S (%) n-C_4H_{10}	S (%) C_2H_4	S (%) C_3H_6	S (%) CO	**S (%) C_2-C_4^0**	**S (%) C_2-$C_4^=$**	**S (%) C_2-C_4**
350	**80.0**	77.0	10	5.6	2.1	0.5	0.8	4.4	**17.7**	**1.2**	**18.9**
400	**83.2**	89.2	4.6	0.8	0.2	0	0.1	5.0	**5.6**	**0.1**	**5.8**
450	**85.5**	92.4	1.4	0.1	0	0	0	6.1	**1.6**	**0**	**1.6**

Table 8.4.3.6. Stability of CO_2 conversion and selectivity for sample **5.3** at different temperatures. (Reaction conditions: H_2/CO_2 ratio of 7, total flow 4 mL/min, 10 bar, 40 mg catalyst.)

T (°C)	**C (%) CO_2**	S (%) CH_4	S (%) C_2H_6	S (%) C_3H_8	S (%) n-C_4H_{10}	S (%) C_2H_4	S (%) C_3H_6	S (%) CO	**S (%) C_2-C_4^0**	**S (%) C_2-$C_4^=$**	**S (%) C_2-C_4**
300	**9.8**	81.3	1.3	0	0	0	0	17.4	**1.3**	**0**	**1.3**
350	**32.7**	76.1	4.4	1.6	1.4	0	0.5	16.0	**7.4**	**0.5**	**7.9**
400	**74.4**	68.4	11.9	7.4	3.5	0.6	1.4	6.9	**22.8**	**2.0**	**24.8**
450	**82.9**	83.0	6.9	1.8	0.6	0.3	0.3	7.2	**9.3**	**0.5**	**9.8**
500	**87.9**	91.4	2.1	0.2	0	0.1	0	6.3	**2.3**	**0.1**	**2.3**
300	**18.6**	43.9	7.8	5.1	5.4	0.6	4.1	33.1	**18.2**	**4.8**	**23.0**
350	**50.9**	58.3	12.9	7.7	5.1	0.9	3.3	11.8	**25.6**	**4.2**	**29.8**
400	**77.5**	69.0	12.6	7.0	2.9	0.7	1.7	6.1	**22.5**	**2.4**	**24.9**
450	**82.2**	85.9	6.2	1.2	0.3	0.2	0.3	6.1	**7.7**	**0.4**	**8.1**
500	**85.6**	91.9	1.9	0.2	0	0	0	6.0	**2.0**	**0**	**2.0**

300	**19.0**	45.2	7.9	5.5	5.1	0.6	3.5	32.3	**18.5**	**4.1**	**22.6**
350	**51.2**	58.7	12.9	7.9	4.7	0.9	3.3	11.7	**25.5**	**4.2**	**29.7**
400	**77.3**	68.8	12.4	6.7	3.5	0.7	1.7	6.2	**22.6**	**2.4**	**25.0**
450	**82.2**	86.6	5.9	1.1	0	0.1	0.2	6.1	**6.9**	**0.4**	**7.3**
500	**86.2**	91.9	1.8	0.1	0	0	0	6.2	**1.9**	**0**	**1.9**
300	**21.7**	46.1	8.9	6.4	6.1	0.8	3.7	28.2	**21.3**	**4.4**	**25.7**
350	**55.4**	58.9	13.3	8.3	5.0	0.9	3.5	10	**26.7**	**4.4**	**31.1**
400	**77.9**	70	12.2	6.4	3.1	0.7	1.6	6.0	**21.7**	**2.3**	**24.0**
450	**84.3**	86.2	5.7	1.3	0.3	0.2	0.2	6.0	**7.3**	**0.4**	**7.7**
500	**88.6**	92.0	1.8	0.3	0	0	0	6.0	**2.1**	**0**	**2.1**

Table 8.4.3.7. CO_2 conversion and selectivity for sample **5.3** at different temperatures. (Reaction conditions: H_2/CO_2 ratio of 4, total flow 4 mL/min, 10 bar, 40 mg catalyst.)

T (°C)	**C (%) CO_2**	S (%) CH_4	S (%) C_2H_6	S (%) C_3H_8	S (%) *n*-C_4H_{10}	S (%) C_2H_4	S (%) C_3H_6	S (%) CO	**S (%) C_2-C_4^0**	**S (%) C_2-$C_4^=$**	**S (%) C_2-C_4**
300	**21.0**	32.3	11.5	7.6	7.1	1.9	10.8	28.8	**26.2**	**12.7**	**38.9**
350	**48.9**	52.9	15.9	6.6	6.3	1.6	7.4	9.2	**28.9**	**9.0**	**37.9**
400	**61.3**	59.8	15.4	6.1	4.8	1.0	3.7	9.1	**26.4**	**4.7**	**31.0**
450	**66.7**	77.6	8.2	1.8	0.5	0.3	0.6	11.0	**10.6**	**0.8**	**11.4**
500	**70.3**	83.6	2.9	0.3	0	0	0	13.3	**3.1**	**0**	**3.1**

Table 8.4.3.8. CO_2 conversion and selectivity for sample **5.3** at different temperatures. (Reaction conditions: H_2/CO_2 ratio of 3, total flow 4 mL/min, 10 bar, 40 mg catalyst.)

T (°C)	**C (%) CO_2**	S (%) CH_4	S (%) C_2H_6	S (%) C_3H_8	S (%) *n*-C_4H_{10}	S (%) C_2H_4	S (%) C_3H_6	S (%) CO	**S (%) C_2-C_4^0**	**S (%) C_2-$C_4^=$**	**S (%) C_2-C_4**
300	**13.6**	34.7	7.9	4.9	6.0	0.8	6.3	39.5	**18.7**	**7.1**	**25.9**
350	**38.6**	49.3	14.4	7.2	6.1	1.6	7.6	13.9	**27.6**	**9.2**	**36.9**
400	**51.0**	50.8	15.3	8.9	6.0	1.4	5.1	12.5	**30.2**	**6.4**	**36.6**
450	**54.5**	68.8	9.9	2.6	0.9	0.3	0.9	16.6	**13.4**	**1.2**	**14.6**
500	**58.1**	76.2	3.5	0.3	0	0	0.1	19.9	**3.8**	**0.1**	**3.9**

Table 8.4.3.9. CO_2 conversion and selectivity for sample **5.3** at different temperatures. (Reaction conditions: H_2/CO_2 ratio of 2, total flow 4 mL/min, 10 bar, 40 mg catalyst.)

T (°C)	**C (%) CO_2**	S (%) CH_4	S (%) C_2H_6	S (%) C_3H_8	S (%) *n*-C_4H_{10}	S (%) C_2H_4	S (%) C_3H_6	S (%) CO	**S (%) C_2-C_4^0**	**S (%) C_2-$C_4^=$**	**S (%) C_2-C_4**
300	**13.5**	27.3	9.0	6.1	6.2	2.2	9.4	39.9	**21.2**	**11.6**	**32.8**
350	**34.5**	46.1	14.8	9.1	6.1	2.4	8.3	13.3	**29.9**	**10.7**	**40.6**
400	**40.3**	48.3	15.3	7.4	6.4	1.6	5.5	15.6	**29.0**	**7.1**	**36.2**
450	**43.2**	62.5	10.9	3.5	0.7	0.4	1.0	21.0	**15.1**	**1.4**	**16.5**
500	**45.8**	68.2	4.1	0.4	0	0.1	0.1	27.0	**4.5**	**0.2**	**4.7**

Table 8.4.3.10. CO_2 conversion and selectivity for sample **5.3** at different temperatures. (Reaction conditions: H_2/CO_2 ratio of 1, total flow 4 mL/min, 10 bar, 40 mg catalyst.)

T (°C)	**C (%) CO_2**	S (%) CH_4	S (%) C_2H_6	S (%) C_3H_8	S (%) n-C_4H_{10}	S (%) C_2H_4	S (%) C_3H_6	S (%) CO	**S (%) C_2-C_4^0**	**S (%) C_2-$C_4^=$**	**S (%) C_2-C_4**
300	**9.0**	17.8	7.0	4.0	5.1	2.6	11.1	52.5	**16.0**	**13.7**	**29.7**
350	**19.1**	36.9	12.4	6.2	5.3	3.8	11.0	24.5	**23.9**	**14.8**	**38.7**
400	**24.5**	39.2	12.9	7.6	6.9	2.0	6.4	25.1	**27.3**	**8.4**	**35.7**
450	**27.3**	50	9.4	3.6	3.1	0.5	1.2	32.2	**16.1**	**1.7**	**17.8**
500	**29.6**	49.5	3.8	0.6	2.5	0.1	0.2	43.3	**6.9**	**0.3**	**7.2**

Table 8.4.3.11. CO_2 conversion and selectivity for sample **5.3** at different temperatures. (Reaction conditions: H_2/CO_2 ratio of 4, total flow 4 mL/min, 5 bar, 40 mg catalyst.)

T (°C)	**C (%) CO_2**	S (%) CH_4	S (%) C_2H_6	S (%) C_3H_8	S (%) n-C_4H_{10}	S (%) C_2H_4	S (%) C_3H_6	S (%) CO	**S (%) C_2-C_4^0**	**S (%) C_2-$C_4^=$**	**S (%) C_2-C_4**
250	**18.8**	6.4	4.4	5.1	0	3.8	61.5	18.8	**9.5**	**65.3**	**74.8**
300	**34.4**	13.7	10.7	9.7	1.1	7.8	22.6	34.4	**21.5**	**30.3**	**51.9**
350	**52.3**	17.5	8.1	8.2	1.0	4.4	8.5	52.3	**17.3**	**12.9**	**30.2**
400	**60.1**	16.1	7.5	6.2	0.3	1.2	8.6	60.1	**14.0**	**9.8**	**23.7**
450	**72.6**	10.9	3.4	0.8	0.1	0.3	11.9	72.6	**4.3**	**12.2**	**16.5**

Table 8.4.3.12. CO_2 conversion and selectivity for sample **5.3** at different temperatures. (Reaction conditions: H_2/CO_2 ratio of 4, total flow 4 mL/min, 15 bar, 40 mg catalyst.)

T (°C)	**C (%)**	S (%)	S (%)	S (%)	S (%)	S (%)	S (%)	S (%)	**S (%)**	**S (%)**	**S (%)**
	CO_2	CH_4	C_2H_6	C_3H_8	n-C_4H_{10}	C_2H_4	C_3H_6	CO	**C_2-C_4^0**	**C_2-$C_4^=$**	**C_2-C_4**
250	**7.1**	39.5	5.4	3.5	4.3	0	2.9	44.5	**13.1**	**2.9**	**16.0**
300	**34.0**	53.7	12.0	10.4	8.6	0.4	3.2	11.8	**30.9**	**3.6**	**34.5**
350	**68.3**	62.9	14.9	10.8	6.4	0.2	1.5	3.3	**32.1**	**1.7**	**33.8**
400	**76.9**	76.7	11.9	5.9	1.9	0.1	0.4	3.1	**19.7**	**0.5**	**20.2**
450	**80.1**	88.9	5.8	1.2	0.1	0	0.1	4.0	**7.0**	**0.1**	**7.1**

Table 8.4.3.13. CO_2 conversion and selectivity for sample **5.3** at different temperatures. (Reaction conditions: H_2/CO_2 ratio of 4, total flow 4 mL/min, 20 bar, 40 mg catalyst.)

T (°C)	**C (%)**	S (%)	S (%)	S (%)	S (%)	S (%)	S (%)	S (%)	**S (%)**	**S (%)**	**S (%)**
	CO_2	CH_4	C_2H_6	C_3H_8	n-C_4H_{10}	C_2H_4	C_3H_6	CO	**C_2-C_4^0**	**C_2-$C_4^=$**	**C_2-C_4**
250	**8.3**	21.0	8.8	6.0	9.6	0	3.0	51.7	**24.3**	**3.0**	**27.3**
300	**40.7**	46.3	15.8	12.9	13.5	0.3	3.1	8.2	**42.2**	**3.4**	**45.6**
350	**82.7**	76.0	12.3	5.5	4.7	0.2	0.5	0.9	**22.4**	**0.8**	**23.2**
400	**87.8**	87.8	8.1	2.1	0.7	0.1	0.2	1.0	**11.0**	**0.3**	**11.2**
450	**84.6**	90.2	6.1	1.1	0.2	0	0.1	2.3	**7.4**	**0.1**	**7.5**

Table 8.4.3.14. CO_2 conversion and selectivity for sample **5.3** at different temperatures. (Reaction conditions: H_2/CO_2 ratio of 4, total flow 4 mL/min, 40 bar, 40 mg catalyst.)

T (°C)	**C (%) CO_2**	S (%) CH_4	S (%) C_2H_6	S (%) C_3H_8	S (%) n-C_4H_{10}	S (%) C_2H_4	S (%) C_3H_6	S (%) CO	**S (%) C_2-C_4^0**	**S (%) C_2-$C_4^=$**	**S (%) C_2-C_4**
250	**10.1**	35.6	10.2	7.8	10.7	0	4.7	31.0	**28.7**	**4.7**	**33.4**
300	**58.4**	52.7	16.9	14.5	10.1	0.2	2.8	2.9	**41.5**	**3.0**	**44.5**
350	**92.5**	79.8	10.3	5.0	4.1	0.1	0.4	0.3	**19.4**	**0.5**	**19.9**
400	**96.8**	89.4	6.2	2.6	1.4	0.1	0.1	0.2	**10.2**	**0.2**	**10.4**
450	**97.4**	93.4	4.4	1.5	0.2	0.1	0.1	0.2	**6.2**	**0.2**	**6.4**

Table 8.4.3.15. CO_2 conversion and selectivity for sample **5.3** at different temperatures. (Reaction conditions: H_2/CO_2 ratio of 2, total flow 4 mL/min, 5 bar, 40 mg catalyst.)

T (°C)	**C (%) CO_2**	S (%) CH_4	S (%) C_2H_6	S (%) C_3H_8	S (%) n-C_4H_{10}	S (%) C_2H_4	S (%) C_3H_6	S (%) CO	**S (%) C_2-C_4^0**	**S (%) C_2-$C_4^=$**	**S (%) C_2-C_4**
250	**3.6**	7.7	2.0	3.1	0	0	1.7	85.5	**5.1**	**1.7**	**6.7**
300	**13.6**	12.4	4.6	2.0	3.0	1.0	7.8	69.3	**9.6**	**8.7**	**18.4**
350	**26.1**	30.8	11.3	5.0	4.4	2.7	10.7	35.2	**20.6**	**13.4**	**34.0**
400	**36.4**	44.9	14.2	6.1	3.2	1.0	5.2	25.4	**23.5**	**6.2**	**29.7**
450	**40.9**	60.6	7.4	1.3	0.3	0.3	0.7	29.4	**8.9**	**1.1**	**10**

Table 8.4.3.16. CO_2 conversion and selectivity for sample **5.3** at different temperatures. (Reaction conditions: H_2/CO_2 ratio of 2, total flow 4 mL/min, 7.5 bar, 40 mg catalyst.)

T (^oC)	**C (%) CO_2**	S (%) CH_4	S (%) C_2H_6	S (%) C_3H_8	S (%) n-C_4H_{10}	S (%) C_2H_4	S (%) C_3H_6	S (%) CO	**S (%) C_2-C_4^0**	**S (%) C_2-$C_4^=$**	**S (%) C_2-C_4**
250	**4.3**	8.8	1.9	0.7	2.0	0	2.6	84.0	**4.7**	**2.6**	**7.2**
300	**15.1**	15.9	6.5	4.0	3.8	1.9	8.3	59.6	**14.3**	**10.1**	**24.4**
350	**29.3**	36.6	14.1	7.1	5.9	2.2	8.5	25.7	**27.1**	**10.6**	**37.7**
400	**38.8**	49.5	15.6	7.2	4.2	0.7	3.6	19.3	**27.0**	**4.3**	**31.2**
450	**43.0**	65.5	9.1	2.2	0.2	0.2	0.7	22.1	**11.5**	**0.9**	**12.4**

Table 8.4.3.17. CO_2 conversion and selectivity for sample **5.3** at different temperatures. (Reaction conditions: H_2/CO_2 ratio of 2, total flow 4 mL/min, 15 bar, 40 mg catalyst.)

T (^oC)	**C (%) CO_2**	S (%) CH_4	S (%) C_2H_6	S (%) C_3H_8	S (%) n-C_4H_{10}	S (%) C_2H_4	S (%) C_3H_6	S (%) CO	**S (%) C_2-C_4^0**	**S (%) C_2-$C_4^=$**	**S (%) C_2-C_4**
250	**5.6**	18.8	6.4	4.4	5.1	0	3.8	61.5	**15.9**	**3.8**	**19.7**
300	**21.3**	34.4	13.7	10.7	9.7	1.1	7.8	22.6	**34.1**	**8.9**	**43.0**
350	**38.0**	52.3	17.5	8.1	8.2	1.0	4.4	8.5	**33.8**	**5.4**	**39.1**
400	**48.7**	60.1	16.1	7.5	6.2	0.3	1.2	8.6	**29.8**	**1.5**	**31.3**
450	**50.2**	72.6	10.9	3.4	0.8	0.1	0.3	11.9	**15.1**	**0.4**	**15.5**

Table 8.4.3.18. CO_2 conversion and selectivity for sample **5.3** at different temperatures. (Reaction conditions: H_2/CO_2 ratio of 2, total flow 4 mL/min, 20 bar, 40 mg catalyst.)

T (°C)	**C (%) CO_2**	S (%) CH_4	S (%) C_2H_6	S (%) C_3H_8	S (%) n-C_4H_{10}	S (%) C_2H_4	S (%) C_3H_6	S (%) CO	**S (%) C_2-C_4^0**	**S (%) C_2-$C_4^=$**	**S (%) C_2-C_4**
250	**5.8**	38.9	6.3	4.8	6.0	0	1.4	42.6	**17.1**	**1.4**	**18.5**
300	**26.5**	51.8	11.9	11.7	9.4	0.3	3.2	11.8	**33.0**	**3.5**	**36.5**
350	**44.8**	60.2	15.8	8.8	7.6	0.3	2.0	5.3	**32.2**	**2.3**	**34.5**
400	**50.5**	68.9	14.7	6.1	3.3	0.2	0.8	5.9	**24.2**	**1.0**	**25.2**
450	**51.8**	77.5	10.5	2.6	0.3	0.1	0.2	8.9	**13.3**	**0.3**	**13.6**

Table 8.4.3.19. CO_2 conversion and selectivity for sample **5.3** at different temperatures. (Reaction conditions: H_2/CO_2 ratio of 1, total flow 4 mL/min, 5 bar, 40 mg catalyst.)

T (°C)	**C (%) CO_2**	S (%) CH_4	S (%) C_2H_6	S (%) C_3H_8	S (%) n-C_4H_{10}	S (%) C_2H_4	S (%) C_3H_6	S (%) CO	**S (%) C_2-C_4^0**	**S (%) C_2-$C_4^=$**	**S (%) C_2-C_4**
250	**3.5**	2.9	0.8	0	0	0	1.4	94.9	**0.8**	**1.4**	**2.2**
300	**10.9**	5.5	1.9	1.2	1.3	0	4.5	85.7	**4.4**	**4.5**	**8.8**
350	**16.6**	16.4	6.0	1.3	1.9	2.1	7.5	64.8	**9.2**	**9.6**	**18.8**
400	**22.2**	28.6	10.2	3.6	2.0	0.9	5.6	49.1	**15.8**	**6.5**	**22.3**

Table 8.4.3.20. CO_2 conversion and selectivity for sample **5.3** at different

temperatures. (Reaction conditions: H_2/CO_2 ratio of 1, total flow 4 mL/min, 15 bar, 40 mg catalyst.)

T (°C)	**C (%) CO_2**	S (%) CH_4	S (%) C_2H_6	S (%) C_3H_8	S (%) $n\text{-}C_4H_{10}$	S (%) C_2H_4	S (%) C_3H_6	S (%) CO	**S (%) $C_2\text{-}C_4^0$**	**S (%) $C_2\text{-}C_4^=$**	**S (%) $C_2\text{-}C_4$**
250	**3.8**	8.4	2.9	1.8	3.2	0	2.8	81.0	**7.9**	**2.8**	**10.7**
300	**21.9**	12.8	**51.7**	3.4	2.6	0.5	3.1	25.9	**57.7**	**3.6**	**61.4**
350	**26.4**	31.0	33.3	7.9	5.5	1.2	4.6	16.6	**46.6**	**5.8**	**52.4**
400	**30.8**	35.5	33.5	6.1	5.2	0.6	2.4	16.7	**44.8**	**3.0**	**47.8**

Table 8.4.3.21. CO_2 conversion and selectivity for sample **5.3** at different temperatures. (Reaction conditions: H_2/CO_2 ratio of 1, total flow 4 mL/min, 20 bar, 40 mg catalyst.)

T (°C)	**C (%) CO_2**	S (%) CH_4	S (%) C_2H_6	S (%) C_3H_8	S (%) $n\text{-}C_4H_{10}$	S (%) C_2H_4	S (%) C_3H_6	S (%) CO	**S (%) $C_2\text{-}C_4^0$**	**S (%) $C_2\text{-}C_4^=$**	**S (%) $C_2\text{-}C_4$**
250	**3.7**	12.1	2.9	2.5	3.4	0	3.0	76.2	**8.8**	**3.0**	**11.8**
300	**12.9**	24.1	10.4	9.2	7.9	1.6	7.4	39.5	**27.5**	**9.0**	**36.4**
350	**24.0**	40.3	16.0	12.5	8.8	1.3	5.7	15.4	**37.2**	**7.0**	**44.3**
400	**29.2**	45.7	16.2	12.2	8.3	0.5	2.3	14.9	**36.7**	**2.8**	**39.5**

8.4.4 Tables of catalytic activity and selectivity for C_2-C_4 hydrocarbons with promoters and poison in CHAPTER 6

Table 8.4.4.1. CO_2 conversion and selectivity for sample **6.1** at different

temperatures. (Reaction conditions: H_2/CO_2 ratio of 7, total flow 4 mL/min, 10 bar, 40 mg catalyst.)

T (^{o}C)	**C (%)**	S (%)	S (%)	S (%)	S (%)	S (%)	S (%)	S (%)	**S (%)**	**S (%)**	**S (%)**
	CO_2	CH_4	C_2H_6	C_3H_8	*n*-C_4H_{10}	C_2H_4	C_3H_6	CO	**C_2-C_4^0**	**C_2-$C_4^=$**	**C_2-C_4**
300	**9.8**	81.3	1.3	0	0	0	0	17.4	**1.3**	**0**	**1.3**
350	**32.7**	76.1	4.4	1.6	1.4	0	0.5	16.0	**7.4**	**0.5**	**7.9**
400	**74.4**	68.4	11.9	7.4	3.5	0.6	1.4	6.9	**22.8**	**2.0**	**24.8**
450	**82.9**	83.0	6.9	1.8	0.6	0.3	0.3	7.2	**9.3**	**0.5**	**9.8**
500	**87.9**	91.4	2.1	0.2	0	0.1	0	6.3	**2.3**	**0.1**	**2.3**

Table 8.4.4.2. CO_2 conversion and selectivity for sample **6.2** at different temperatures. (Reaction conditions: H_2/CO_2 ratio of 7, total flow 4 mL/min, 10 bar, 40 mg catalyst.)

T (^{o}C)	**C (%)**	S (%)	S (%)	S (%)	S (%)	S (%)	S (%)	S (%)	**S (%)**	**S (%)**	**S (%)**
	CO_2	CH_4	C_2H_6	C_3H_8	*n*-C_4H_{10}	C_2H_4	C_3H_6	CO	**C_2-C_4^0**	**C_2-$C_4^=$**	**C_2-C_4**
300	**19.6**	68.0	6.1	2.8	3.2	0	2.1	17.9	**12.1**	**2.1**	**14.1**
350	**39.6**	84.4	2.4	2.3	1.6	0	0.8	8.5	**6.3**	**0.8**	**7.1**
400	**74.4**	85.1	6.6	2.0	0.9	0	0.4	5.1	**9.4**	**0.4**	**9.8**
450	**83.8**	89.7	4.0	0.5	0	0.1	0.1	5.5	**4.6**	**0.3**	**4.8**
500	**84.7**	91.4	1.5	0.2	0	0	0	6.9	**1.7**	**0**	**1.7**

Table 8.4.4.3. CO_2 conversion and selectivity for sample **6.3** at different

temperatures. (Reaction conditions: H_2/CO_2 ratio of 7, total flow 4 mL/min, 10 bar, 40 mg catalyst.)

T (°C)	**C (%)**	S (%)	S (%)	S (%)	S (%)	S (%)	S (%)	S (%)	**S (%)**	**S (%)**	**S (%)**
	CO_2	CH_4	C_2H_6	C_3H_8	*n*-C_4H_{10}	C_2H_4	C_3H_6	CO	**C_2-C_4^0**	**C_2-$C_4^=$**	**C_2-C_4**
300	**8.2**	65.6	0.7	0	0	0	0	33.7	**0.7**	**0**	**0.7**
350	**28.8**	61.9	3.8	1.6	1.6	0	0.9	30.3	**7.0**	**0.9**	**7.9**
400	**64.4**	64.2	11.4	5.3	3.4	0.8	2.1	12.8	**20.1**	**2.9**	**23.0**
450	**77.0**	80.3	6.3	1.3	0.4	0.2	0.3	11.2	**8.0**	**0.5**	**8.5**
500	**82.4**	86.0	2.2	0.2	0	0	0	11.6	**2.4**	**0**	**2.4**

Table 8.4.4.4. CO_2 conversion and selectivity for sample **6.4** at different temperatures. (Reaction conditions: H_2/CO_2 ratio of 7, total flow 4 mL/min, 10 bar, 40 mg catalyst.)

T (°C)	**C (%)**	S (%)	S (%)	S (%)	S (%)	S (%)	S (%)	S (%)	**S (%)**	**S (%)**	**S (%)**
	CO_2	CH_4	C_2H_6	C_3H_8	*n*-C_4H_{10}	C_2H_4	C_3H_6	CO	**C_2-C_4^0**	**C_2-$C_4^=$**	**C_2-C_4**
300	**6.0**	80.6	2.5	0	0	0	0	16.9	**2.5**	**0**	**2.5**
350	**23.9**	84.4	2.4	0	0	0	0	13.2	**2.4**	**0**	**2.4**
400	**71.3**	75.2	9.8	5.2	2.2	0.3	1.1	6.2	**17.2**	**1.4**	**18.6**
450	**84.3**	86.6	5.8	1.3	0.3	0.2	0.2	5.6	**7.4**	**0.4**	**7.8**
500	**88.6**	91.6	2.2	0.3	0	0	0	6.0	**2.4**	**0**	**2.4**

Table 8.4.4.5. CO_2 conversion and selectivity for sample **6.5** at different

temperatures. (Reaction conditions: H_2/CO_2 ratio of 7, total flow 4 mL/min, 10 bar, 40 mg catalyst.)

T (°C)	**C (%) CO_2**	S (%) CH_4	S (%) C_2H_6	S (%) C_3H_8	S (%) n-C_4H_{10}	S (%) C_2H_4	S (%) C_3H_6	S (%) CO	**S (%) C_2-C_4^0**	**S (%) C_2-$C_4^=$**	**S (%) C_2-C_4**
250	**6.8**	86.0	3.0	7.6	0	0	0	3.4	**10.6**	**0**	**10.6**
300	**24.5**	92.0	3.6	1.5	0	0	0	2.9	**5.1**	**0**	**5.1**
350	**50.9**	88.4	6.6	2.0	0.8	0	0	2.3	**9.3**	**0**	**9.3**
400	**72.2**	90.2	6.2	1.1	0.3	0	0	2.2	**7.5**	**0**	**7.5**
450	**80.0**	94.5	2.7	0.1	0	0	0	2.7	**2.8**	**0**	**2.8**

Table 8.4.4.6. CO_2 conversion and selectivity for sample **6.6** at different temperatures. (Reaction conditions: H_2/CO_2 ratio of 7, total flow 4 mL/min, 10 bar, 40 mg catalyst.)

T (°C)	**C (%) CO_2**	S (%) CH_4	S (%) C_2H_6	S (%) C_3H_8	S (%) n-C_4H_{10}	S (%) C_2H_4	S (%) C_3H_6	S (%) CO	**S (%) C_2-C_4^0**	**S (%) C_2-$C_4^=$**	**S (%) C_2-C_4**
300	**32.1**	95.8	1.8	0.8	0	0	0	1.7	**2.5**	**0**	**2.5**
350	**65.6**	95.9	2.3	0.3	0	0	0	1.5	**2.6**	**0**	**2.6**
400	**84.8**	96.9	1.6	0.1	0	0	0	1.4	**1.7**	**0**	**1.7**
450	**92.1**	97.9	0.8	0.1	0	0	0	1.2	**0.9**	**0**	**0.9**
500	**94.2**	97.8	0.6	0.1	0	0	0	1.5	**0.7**	**0**	**0.7**

Table 8.4.4.7. CO_2 conversion and selectivity for sample **6.7** at different

temperatures. (Reaction conditions: H_2/CO_2 ratio of 4, total flow 4 mL/min, 10 bar, 40 mg catalyst.)

T (°C)	**C (%) CO_2**	S (%) CH_4	S (%) C_2H_6	S (%) C_3H_8	S (%) *n*-C_4H_{10}	S (%) C_2H_4	S (%) C_3H_6	S (%) CO	**S (%) C_2-C_4^0**	**S (%) C_2-$C_4^=$**	**S (%) C_2-C_4**
250	**1.4**	41.4	16.0	17.8	0	0	0	24.8	**33.8**	**0**	**33.8**
300	**4.8**	54.4	3.7	8.8	0	0	0	33.1	**12.5**	**0**	**12.5**
350	**12.3**	49.9	5.3	2.2	2.7	0	0	39.8	**10.3**	**0**	**10.3**
400	**37.3**	61.3	10.5	5.1	1.9	0	0.3	20.9	**17.5**	**0.3**	**17.8**
450	**62.0**	79.2	7.6	1.4	0.2	0	0.1	11.5	**9.1**	**0.1**	**9.2**

Table 8.4.4.8. CO_2 conversion and selectivity for sample **6.8** at different temperatures. (Reaction conditions: H_2/CO_2 ratio of 3, total flow 4 mL/min, 10 bar, 40 mg catalyst.)

T (°C)	**C (%) CO_2**	S (%) CH_4	S (%) C_2H_6	S (%) C_3H_8	S (%) *n*-C_4H_{10}	S (%) C_2H_4	S (%) C_3H_6	**S (%) CO**	S (%) C_2-C_4^0	S (%) C_2-$C_4^=$	S (%) C_2-C_4
300	**1.6**	0	14.4	48.1	0	0	30.7	**6.9**	62.5	30.7	93.1
350	**0.5**	0	9.2	0	0	0	0	**90.8**	9.2	0	9.2
400	**1.8**	0	2.7	0	0	0	0	**97.3**	2.7	0	2.7
450	**6.7**	1.6	0.8	0	0	0	0	**97.7**	0.8	0	0.8
500	**19.6**	1.5	0.6	0	0	0	0	**98.0**	0.6	0	0.6

Table 8.4.4.9. CO_2 conversion and selectivity for sample **6.9** at different

temperatures. (Reaction conditions: H_2/CO_2 ratio of 2, total flow 4 mL/min, 10 bar, 40 mg catalyst.)

T (°C)	**C (%) CO_2**	S (%) CH_4	S (%) C_2H_6	S (%) C_3H_8	S (%) n-C_4H_{10}	S (%) C_2H_4	S (%) C_3H_6	**S (%) CO**	S (%) C_2-C_4^0	S (%) C_2-$C_4^=$	S (%) C_2-C_4
300	**1.4**	0	19.8	40.9	0	0	21.9	**17.4**	60.7	21.9	82.7
350	**1.0**	0	6.2	0	0	0	0	**93.8**	6.2	0	6.2
400	**3.7**	2.1	1.1	0	0	0	0	**96.9**	1.1	0	1.1
450	**11.4**	1.1	0.5	0	0	0	0	**98.4**	0.5	0	0.5
500	**31.1**	1.2	0.4	0	0	0	0	**98.4**	0.4	0	0.4

Table 8.4.4.10. CO_2 conversion and selectivity for sample **6.10** at different temperatures. (Reaction conditions: H_2/CO_2 ratio of 1, total flow 4 mL/min, 10 bar, 40 mg catalyst.)

T (°C)	**C (%) CO_2**	S (%) CH_4	S (%) C_2H_6	S (%) C_3H_8	S (%) n-C_4H_{10}	S (%) C_2H_4	S (%) C_3H_6	**S (%) CO**	S (%) C_2-C_4^0	S (%) C_2-$C_4^=$	S (%) C_2-C_4
300	**1.0**	0	23.3	38.7	0	0	23.5	**14.5**	62.0	23.5	85.5
350	**0.7**	0	5.6	0	0	0	0	**94.4**	5.6	0	5.6
400	**2.0**	4.2	2.6	0	0	0	0	**93.2**	2.6	0	2.6
450	**5.1**	2.3	1.2	0	0	0	0	**96.5**	1.2	0	1.2
500	**13.2**	1.7	1.2	0	0	0	0	**97.1**	1.2	0	1.2

Table 8.4.4.11. CO_2 conversion and selectivity for sample **6.11** at different

temperatures. (Reaction conditions: H_2/CO_2 ratio of 1, total flow 4 mL/min, 10 bar, 40 mg catalyst.)

T (°C)	**C (%) CO_2**	S (%) CH_4	S (%) C_2H_6	S (%) C_3H_8	S (%) n-C_4H_{10}	S (%) C_2H_4	S (%) C_3H_6	**S (%) CO**	S (%) C_2-C_4^0	S (%) C_2-$C_4^=$	S (%) C_2-C_4
300	**4.3**	1.8	3.4	0	0	0	5.9	**88.9**	3.4	5.9	9.3
350	**15.3**	0.6	0.9	0	0	0	0	**98.5**	0.9	0	0.9
400	**30.6**	0.6	0.3	0	0	0	0	**99.1**	0.3	0	0.3
450	**46.2**	0.7	0.2	0	0	0	0	**99.1**	0.2	0	0.2
500	**59.2**	1.2	0.5	0	0	0	0	**98.3**	0.5	0	0.5

8.4.5 Tables of catalytic activity and selectivity for methanol in CHAPTER 7

Table 8.4.5.1. CO_2 conversion and selectivity for sample **7.1** at different temperatures. (Reaction conditions: H_2/CO_2 ratio of 4, total flow 4 mL/min, 40 bar, 40 mg catalyst.)

T (°C)	**C (%) CO_2**	S (%) CH_4	S (%) C_2H_6	S (%) C_3H_8	S (%) n-C_4H_{10}	S (%) C_2H_4	S (%) C_3H_6	S (%) CO	**S (%) CH_3OH**
150	**0**	0	0	0	0	0	0	0	**0**
200	**0.1**	0	0	0	0	0	0	100	**0**
250	**0.6**	0	0	10.5	0	0	0	89.5	**0**
300	**2.6**	6.0	1.8	25.8	0	0	0	66.4	**0**

Table 8.4.5.2. CO_2 conversion and selectivity for sample **7.3** at different

temperatures. (Reaction conditions: H_2/CO_2 ratio of 4, total flow 4 mL/min, 40 bar, 40 mg catalyst.)

T (°C)	**C (%) CO_2**	S (%) CH_4	S (%) C_2H_6	S (%) C_3H_8	S (%) n-C_4H_{10}	S (%) C_2H_4	S (%) C_3H_6	S (%) CO	**S (%) CH_3OH**
150	**0**	0	0	0	0	0	0	0	**0**
200	**0.1**	0	0	0	0	0	0	100	**0**
250	**3.2**	1.3	0	0	0	0	0	39.9	**58.8**
300	**11.1**	1.7	0.6	0.5	0	0	0	72.9	**24.4**
150	**0**	0	0	0	0	0	0	0	**0**
200	**0.1**	0	0	0	0	0	0	100	**0**
250	**1.6**	2.1	0	0	0	0	0	98.0	**0**
300	**9.3**	2.8	0.5	0	0	0	0	96.7	**0**

Table 8.4.5.3. CO_2 conversion and selectivity for sample **7.5** at different temperatures. (Reaction conditions: H_2/CO_2 ratio of 4, total flow 4 mL/min, 40 bar, 40 mg catalyst.)

T (°C)	**C (%) CO_2**	S (%) CH_4	S (%) C_2H_6	S (%) C_3H_8	S (%) n-C_4H_{10}	S (%) C_2H_4	S (%) C_3H_6	S (%) CO	**S (%) CH_3OH**
150	**0.2**	0	0	0	0	0	0	0	**100**
200	**0.2**	0	0	0	0	0	0	52.9	**47.1**
250	**1.2**	10.1	0	0	0	0	0	53.3	**36.6**
300	**4.4**	19.6	1.0	0	0	0	0	51.3	**28.2**

150	**0.2**	0	0	0	0	0	0	0	**100**
200	**0.3**	0	0	0	0	0	0	28.7	**71.3**
250	**1.5**	4.2	0	0	0	0	0	31.6	**64.1**
300	**4.4**	5.4	0	0	0	0	0	49.4	**45.2**

CHAPTER 8

CHAPTER 9

Conclusions

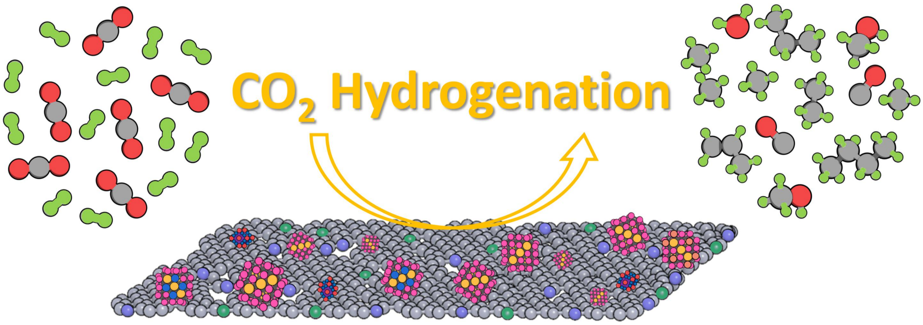

CHAPTER 9

CHAPTER 9

The previous Chapters present the preparation and catalytic activity of various metal nanoparticles supported on defective N-doped graphenes. During this Doctoral Thesis, highly selective and stable catalysts for CO_2 hydrogenation have been developed that are able to drive the reaction towards different high-value products. The properties of catalysts with remarkable performance were controlled, exhibiting significant influence of the metal nanoparticle size and composition of catalysts on the outcome of the catalytic reaction.

More specifically, in view of results presented in **CHAPTERS 3** to **7**, the following conclusions can be drawn based on the catalytic activity of materials.

1) Co and Co-Fe alloy nanoparticles wrapped on defective N-doped graphenes with a broad nanoparticle size distribution are highly efficient catalysts for the Sabatier reaction with remarkable catalytic activity and stability, achieving a selectivity of methane over 90 % at high CO_2 conversion values over 85 %.

2) Small clusters of Co-Fe alloy nanoparticles supported on N-doped graphitic carbon matrix are highly selective catalysts for the reverse-water-gas-shift reaction, reaching a conversion of 56 % with 98 % CO selectivity. These catalysts with the metal loading even below 0.2 wt.% exhibit a higher selectivity and better performance than the ones with larger Co-Fe alloy nanoparticles and higher metal loading in similar composition.

3) By the preparation of Co-Fe alloy nanoparticles with a narrow particle size distribution ranging from 7 to 17 nm, it has been possible to drive the selectivity of CO_2 hydrogenation towards value-added C_{2+} hydrocarbons. It was found that an

increase in temperature, particularly in the range from 300 to 450 °C, is essential for selectivity of C_{2+} products and CO_2 conversion. Under optimized conditions, a selectivity towards C_{2+} hydrocarbons about 45% was obtained with CO_2 conversion closing to 60% and remarkable selectivity values of ethylene and propylene as high as 30 % were also detected at CO_2 conversion about 34 %.

4) It has been found that the presence of Ca and Pd promotes the catalytic activity of Co-Fe alloy nanoparticles wrapped on defective N-doped graphenes towards selectivity of CH_4. Under effective control, the presence of S as a poison on the catalysts could significantly drive selectivity towards CO, although accompanied by a substantial decrease of the catalytic activity.

5) Cu-ZnO-based catalysts have been prepared by the two-step method, in which Zn was added after pyrolysis and the resulting Cu-ZnO supported on defective N-doped graphitic matrix exhibits a high selectivity for CO_2 conversion to methanol at a temperature of 250 °C, but with low CO_2 conversion.

In summary, during the present Doctoral Thesis, a series of highly selective catalysts for CO_2 hydrogenation have been developed based on the use of abundant transition metals and natural polysaccharides as graphene precursors. With all the results achieved, high selectivity to CH_4, remarkable selectivity of reverse water-gas shift reaction and a high proportion of C_{2+} hydrocarbons are the most relevant achievements of the present PhD Thesis, making a contribution to the field of CO_2 hydrogenation.

Abstract

Considering the depletion of fossil fuels and the increasing atmospheric CO_2 concentration, CO_2 hydrogenation is a promising way to convert CO_2 into value-added carbon-containing chemicals and fuels. Taking into account the significant influences of the particle size, chemical composition, nature of the support, and operation conditions on the catalytic performance of catalysts, a series of catalysts for CO_2 hydrogenation have been developed based on the use of abundant non-noble metals and natural polysaccharides as graphene precursors. In the present PhD Thesis, metal species supported on defective graphitic carbon matrix with different particle sizes show different catalytic activity and selectivity for CO_2 hydrogenation.

Under effective control, Co and Co-Fe alloy nanoparticles wrapped on defective N-doped graphenes with a broad nanoparticle size distribution were prepared and performed for the Sabatier reaction, exhibiting a selectivity to methane over 90 % at CO_2 conversion values over 85 %. In the case of single Co or Fe metal and their alloys in the form of clusters and small nanoparticles wrapped on the same support, the selectivity for CO_2 hydrogenation shifts to CO, rather than methane, reaching a conversion of 56 % with 98 % CO selectivity. It is worth noting that the metal alloy clusters-based catalysts with the metal loading even below 0.2 wt.% exhibit a higher selectivity and better performance than the ones with larger Co-Fe alloy nanoparticles ranging from 1-4 nm and higher metal loading in a similar composition.

Abstract

Following the research line for CO_2 hydrogenation, a series of Co-Fe alloy nanoparticles supported on defective N-doped graphenes with controlled nanoparticle size distribution in the range of 7-17 nm are developed, obtaining a selectivity towards C_{2+} hydrocarbons about 45% with a CO_2 conversion close to 60%. In addition, a comparative catalytic activity of similar Co-Fe-based catalysts with promoters and poison has been studied for CO_2 hydrogenation to observe their influence on CO_2 conversion and selectivity. Finally, besides Co-Fe-based catalysts, Cu-ZnO-based catalysts have also been prepared by a two-step method. These Cu-ZnO nanoparticles supported on N-doped defective graphene exhibit a high selectivity for CO_2 conversion to methanol.

Resumen

Teniendo en cuenta el agotamiento de los combustibles fósiles y la creciente concentración de CO_2 en la atmósfera, la hidrogenación de CO_2 es una forma prometedora de convertir el CO_2 en productos químicos y combustibles de carbono de alto valor añadido. Considerando la gran influencia del tamaño de partícula, la composición química, la naturaleza del soporte y las condiciones de operación sobre el comportamiento catalítico de los catalizadores, se han desarrollado una serie de catalizadores para la hidrogenación de CO_2 basados en metales abundantes no nobles y polisacáridos naturales como precursores del grafeno. En la presente tesis doctoral, las especies metálicas soportadas sobre una matriz de carbono grafítico defectuosa, con diferentes tamaños de partículas, muestran diferente actividad catalítica y selectividad para la hidrogenación de CO_2.

Se prepararon, de forma controlada, nanopartículas de aleaciones de Co y Co-Fe soportadas en grafenos dopados con N defectuosos, con una amplia distribución de tamaño de nanopartículas, para la reacción de Sabatier, presentando una selectividad a metano superior al 90% con valores de conversión de CO_2 superiores al 85%. En el caso de un solo metal, Co o Fe, y sus aleaciones en forma de “clusters” y pequeñas nanopartículas soportadas en el mismo material, la selectividad de la hidrogenación de CO_2 cambia a CO, en lugar de metano, obteniéndose un valor del 98 % y alcanzando una conversión de CO_2 del 56%. Conviene resaltar que, los catalizadores basados en “clusters” de aleaciones de metal con una carga de metal incluso por debajo del 0.2 % en peso, exhiben una mayor selectividad y rendimiento que los que tienen nanopartículas de aleaciones de Co-Fe más grandes que varían de 1 a 4 nm y una carga de metal más alta en una composición similar.

Siguiendo la línea de investigación de hidrogenación de CO_2, se desarrollaron una serie de nanopartículas de aleaciones de Co-Fe soportadas sobre grafenos dopados con N defectuosos con distribución de tamaño de nanopartículas controlada en el rango de 7-17 nm, obteniendo una selectividad hacia hidrocarburos C_{2+} alrededor del 45% y una conversión del CO_2 cercana al 60%. Además, se realizó un estudio comparativo de la actividad catalítica de catalizadores similares basados en Co-Fe con promotores e inhibidores para la hidrogenación de CO_2, observando su influencia en la conversión y selectividad de CO_2. Finalmente, además de los catalizadores basados en Co-Fe, también se han preparado catalizadores basados en Cu-ZnO mediante un método de dos pasos. Estas nanopartículas de Cu-ZnO soportadas sobre grafeno defectuoso dopado con N exhiben una alta selectividad hacia la conversión de CO_2 a metanol.

Resum

Tenint en compte l'esgotament dels combustibles fòssils i la creixent concentració de CO_2 en l'atmosfera, la hidrogenació de CO_2 és una forma prometedora de convertir el CO_2 en productes químics i combustibles de carboni d'alt valor afegit. Considerant la gran influència de la grandària de partícula, la composició química, la naturalesa del suport i les condicions d'operació sobre el comportament catalític dels catalitzadors, s'han desenvolupat una sèrie de catalitzadors per a la hidrogenació de CO_2 basats en metalls abundants no nobles i polisacàrids naturals com a precursors del grafé. En la present tesi doctoral, les espècies metàl·liques suportades sobre una matriu de carboni grafític defectuosa, amb diferents grandàries de partícules, mostren diferent activitat catalítica i selectivitat per a la hidrogenació de CO_2.

Es van preparar, de manera controlada, nanopartícules d'aliatges de Co i Co-Fe suportades en grafens dopats amb N defectuosos, amb una àmplia distribució de grandària de nanopartícules, per a la reacció de Sabatier, presentant una selectivitat a metà superior al 90% amb valors de conversió de CO_2 superiors al 85%. En el cas d'un sol metall, Co o Fe, i els seus aliatges en forma de “clústers” i xicotetes nanopartícules suportades en el mateix material, la selectivitat de la hidrogenació de CO_2 canvia a CO, en lloc de metà, obtenint-se un valor del 98% i aconseguint una conversió de CO_2 del 56%. Convé ressaltar que, els catalitzadors basats en “clústers” d'aliatges de metall amb una càrrega de metall fins i tot per davall del 0.2% en pes, exhibeixen una major selectivitat i rendiment que els que tenen nanopartícules d'aliatges de Co-Fe més grans que varien d'1 a 4 nm i una càrrega de metall més alta en una composició similar.

Seguint la línia d'investigació d'hidrogenació de CO_2, es van desenvolupar una sèrie de nanopartícules d'aliatges de Co-Fe suportades sobre grafens dopats amb N defectuosos amb distribució de grandària de nanopartícules controlada en el rang de 7-17 nm, obtenint una selectivitat cap a hidrocarburs C_{2+} al voltant del 45% i una conversió del CO_2 pròxima al 60%. A més, es va realitzar un estudi comparatiu de l'activitat catalítica de catalitzadors similars basats en Co-Fe amb promotors i inhibidors per a la hidrogenació de CO_2, observant la seua influència en la conversió i selectivitat de CO_2. Finalment, a més dels catalitzadors basats en Co-Fe, també s'han preparat catalitzadors basats en Cu-ZnO mitjançant un mètode de dos passos. Aquestes nanopartícules de Cu-ZnO suportades sobre grafé defectuós dopat amb N exhibeixen una alta selectivitat cap a la conversió de CO_2 a metanol.

List of Publications

‡ Co-first authors. *Corresponding author.

Porous Graphitic Carbons Containing Nitrogen by Structuration of Chitosan with Pluronic P123

Lu Peng, Yong Peng, Ana Primo* and Hermenegildo Garcia*. *ACS Applied Materials & Interfaces*, **2021**, 13, 11, 13499-13507.

Cobalt Nanoparticle with Tunable Size Supported on Nitrogen-Deficient Graphitic Carbon Nitride for Efficient Visible Light Driven H_2 Evolution Reaction

Dan Zhang‡, Lu Peng‡, Ke Liu, Hermenegildo Garcia*, Chuanzhi Sun* and Lin Dong. *Chemical Engineering Journal*, **2020**, 381,122576.

3D Defective Graphenes with Subnanometric Porosity Obtained by Soft-Templating Following Zeolite Procedures

Lu Peng, Antonio Doménech-Carbo, Ana Primo* and Hermenegildo Garcia*. *Nanoscale Advances*, **2019**, 1, 4827-4833.

Co-Fe Clusters Supported on N-Doped Graphitic Carbon as Highly-Selective Catalysts for Reverse Water Gas Shift

Lu Peng‡, Bogdan Jurca‡, Ana Primo, Alvaro Gordillo, Vasile I. Parvulescu* and Hermenegildo Garcia*.

ACS Sustainable Chemistry & Engineering, in press.

List of Publications

ZnCdS Dotted with Highly Dispersed Pt Supported on SiO_2 Nanospheres Promoting Photocatalytic Hydrogen Evolution

Ke Liu[‡], Lu Peng[‡], Pingping Zhen[‡], Shaoqing Song, Hermenegildo Garcia* and Chuanzhi Sun*.

Journal of Physical Chemistry C, in press.

Co-Fe Nanoparticles Wrapped on N-Doped Graphitic Carbons as Highly-Selective CO_2 Methanation Catalysts

Bogdan Jurca[‡], Lu Peng[‡], Ana Primo, Alvaro Gordillo, Vasile I. Parvulescu* and Hermenegildo Garcia*.

ACS Applied Materials & Interfaces, in press.

Promotional Effects on the Catalytic Activity of Co-Fe Alloy Supported on Graphitic Carbons for CO_2 Hydrogenation

Bogdan Jurca[‡], Lu Peng[‡], Ana Primo, Alvaro Gordillo, Vasile I. Parvulescu* and Hermenegildo Garcia*.

Under review in *Catalysis Science & Technology*

Particle Size Control of Co-Fe Nanoparticles Wrapped on Defective N-doped Graphitic Carbons as Efficient Catalysts for Selectivity of C_2-C_4 Hydrocarbons in CO_2 Hydrogenation

Lu Peng[‡], Bogdan Jurca[‡], Ana Primo, Alvaro Gordillo, Vasile I. Parvulescu* and

Hermenegildo Garcia*.

To be submitted

Tridimensional N, P-Codoped Carbon Sponges as Highly Selective Catalysts for Aerobic Oxidative Coupling of Benzylamine

Lu Peng, Herme G. Baldovi, Amarajothi Dhakshinamoorthy, Ana Primo* and Hermenegildo Garcia*.

To be submitted

Cu-ZnO Clusters Supported on Nitrogen-Doped Graphitic Carbons as Highly Selective Catalysts for CO_2 Conversion to Methanol

Bogdan Jurca[‡], Lu Peng[‡], Ana Primo, Vasile I. Parvulescu* and Hermenegildo Garcia*.

Under preparation

Patent: Porous 3D Sponges Constitute of One or Multiple Defective Graphene Layers

Hermenegildo García,Ana García Mulero, Ana Primo Lu Peng. Priority Request: P201930865 (04/10/2019), **2019**.